Summer 8-2014

Improved Efficiency Organic Photovoltaic Cells through Morphology Control and Process Modification

Qi Wu
University of Southern Mississippi

The University of Southern Mississippi

IMPROVED EFFICIENCY ORGANIC PHOTOVOLTAIC CELLS THROUGH MORPHOLOGY CONTROL AND PROCESS MODIFICATION

by

Qi Wu

A Dissertation
Submitted to the Graduate School
of The University of Southern Mississippi
in Partial Fulfillment of the Requirements
for the Degree of Doctor of Philosophy

August 2014

ABSTRACT

IMPROVED EFFICIENCY ORGANIC PHOTOVOLTAIC CELLS THROUGH MORPHOLOGY CONTROL AND PROCESS MODIFICATION

by Qi Wu

August 2014

Organic photovoltaic (OPV) cells have drawn great attention due to the potential to produce flexible, light weight, affordable solar cells using polymer organic photovoltaic materials; however, the current power conversion efficiency achieved for these systems is too low for widespread implementation of the technology. Morphology and phase separation are key factors determining the performance of organic photovoltaic cells. Precise control of the size and distribution of the phase-separated photoactive domains is necessary for optimum photon-electron conversion. Polyhedral oligomeric silsesquioxane (POSS) nanostructered chemicals have the potential to provide enhanced control of morphology, crystallinity, and phase dispersion in polymeric blend systems. In this work, POSS molecules with different organic functionalities were utilized to control OPV film morphology. The light absorption, crystallinity, and phase separated domain size were evaluated to determine the relationship between POSS structures and film characteristics. The selected POSS molecules were utilized for further device fabrication and performance measurements, with which the POSS enhanced performance was revealed. Furthermore, processing conditions are also important in determining the performance and phase separated morphology of the OPV devices. The effects of solvent vapor annealing and thermal annealing were evaluated in terms of light absorption, crystallinity, long-term stabilitiy, and device performance.

The University of Southern Mississippi

IMPROVED EFFICIENCY ORGANIC PHOTOVOLTAIC CELLS THROUGH MORPHOLOGY CONTROL AND PROCESS MODIFICATION

by

Qi Wu

A Dissertation
Submitted to the Graduate School
of The University of Southern Mississippi
in Partial Fulfillment of the Requirements
for the Degree of Doctor of Philosophy

Approved:

Dr. Sarah Morgan
Committee Chair

Dr. James Rawlins

Dr. Daniel Savin

Dr. Jeffrey Wiggins

Dr. Derek Patton

Dr. Maureen Ryan
Dean of the Graduate School

August 2014

ACKNOWLEDGMENTS

First, I would like to thank my advisor Dr. Sarah Morgan. The best advisor is not only the people who can give you research directions and ideas but also should be the tutor who let you discover the best of yourself. My advisor, Dr. Sarah Morgan, is just such a great tutor. She taught me how to think about questions logically, do things reliably, and present results clearly. She trusts me even when I face difficulties and feel frustrated. Without her trust, I would never finish my Ph.D. work and become a confident person. It is my honor and luck to work in Dr. Sarah Morgan's group.

Also, I would like to thank my coworkers, Mithun Bhattacharya and Levi Moore, who are working with me on the solar cell project. They not only contribute their knowledge and ideas but also help me a lot with my experiments. Without their help, I would never obtain so many exciting research results alone.

At last, funding from The U.S. Department of Energy under grant number DE-EE0003173, from the Ray C. Anderson Foundation, and from Vistakon R&D, Johnson & Johnson Vision Care, Inc. is gratefully acknowledged. The authors would like to thank Hybrid Plastics, Inc. for donation of the POSS materials and for useful discussions.

TABLE OF CONTENTS

ABSTRACT ……ii

ACKNOWLEDGMENTS……iii

LIST OF TABLES……vi

LIST OF ILLUSTRATIONS……vii

CHAPTER

I. INTRODUCTION 1

Polymeric Photovoltaic Cells
Morphology Control in OPV
Motivation and Goal of Research
References

II. ELUCIDATION OF THE EFFECTS OF POSS STRUCTURE ON MORPHOLOGY AND PHOTOPHYSICAL CHARACTERISTICS OF PHOTOACTIVE POLYMER FILMS.....25

Abstract
Introduction
Experimentation
Results and Discussion
Conclusions
References

III. IDENTIFICATION OF POSS INTERACTIONS WITH P3HT AND PCBM AND RESULTANT PERFORMANCE IN ORGANIC PHOTOVOLTAIC DEVICES 42

Abstract
Introduction
Experimentation
Results and Discussion
Conclusions
References

IV. DETERMINATION OF EFFECTS OF SOLVENT VAPOR AND THERMAL ANNEALING ON ENVIRONMENTAL AND MORPHOLOGY STABILITY OF PHOTOACTIVE POLYMER FILMS AND PHOTOVOLTAIC DEVICES.....82

Abstract
Introduction
Experimentation
Results and Discussion
Conclusions
References

V. CONCLUSIONS 109

VI. RECOMMENDATIONS FOR FUTURE WORK.....111

LIST OF TABLES

Table

1. Roughness of the neat P3HT:PCBM and POSS-modified films 33

2. d-spacing of the neat P3HT:PCBM films and POSS modified films 38

3. Nanomechanical and conductive properties of individual blend components and OPV films at different stages of processing 64

4. Integrated area (x 10^{-4}) of the normalized fluorescence spectra from 600-800 nm 67

5. Performance of OPV devices 70

LIST OF ILLUSTRATIONS

Figure

1. Energy diagram of conjugated polymers (adapted from Figure 10.1 in reference 6) 3

2. Schematic operation of OPV cells (adapted from Figure 6 in reference 29). 4

3. Examples of typical electron donor and acceptor materials in OPV cells. 6

4. Current-voltage (I-V) characteristics of an OPV cell (adapted from Figure 3 in reference 19) 8

5. Schemes of (A) regular structure and (B) inverted structure.. 9

6. Schematic structures of (a) bilayer heterojunction and (b) bulk heterojunction (adapted from Figure 2 in reference 19).....11

7. Chemical degradation of polythiophene derivatives (adapted from Scheme1 in reference 38). 17

8. Structures of P3HT and PCBM 27

9. Structures of POSS molecules 31

10. AFM height images of the (A) Neat P3HT:PCBM (B) H-POSS (C) OH-POSS and (D) PhSO3H-POSS modified P3HT:PCBM films. Image size is 5μmX5μm. 32

11. AFM phase images of the (A) Neat P3HT:PCBM (B) H-POSS (C) OH-POSS and (D) PhSO3H-POSS modified P3HT:PCBM films. Image size is 300 nm X 300 nm. 33

12. UV-vis spectra of the neat P3HT:PCBM films and POSS modified films. 36

13. XRD curves of the neat P3HT:PCBM films and POSS modified films. 38

14. Structures of SH-POSS and Ph-POSS 52

15. Optical microscopy images (1000X) of (A) the neat P3HT:PCBM film (B) the Ph-POSS modified film and (C) the SH-POSS modified film after SVA-TA. POSS is incorporated at 1 wt % 53

16. Raman spectrum of the neat P3HT:PCBM film after SVA-TA.....54

17. Raman images of the (A) neat P3HT:PCBM film (B) Ph-POSS modified film and (C) SH-POSS modified film after SVA-TA. The color bar indicates the peak intensity at 1447 cm^{-1}.....55

18. (A1) height image, (A2) the corresponding DMT modulus image and (A3) current image of P3HT:PCBM film after SVA-TA; (B1) height image (B2) the corresponding DMT modulus image and (B3) current image of the Ph-POSS modified film after SVA-TA; (C1) height image (C2) the corresponding DMT modulus image and (C3) current image of the SH-POSS modified film after SVA-TA. The lateral dimensions of all images are 5 μm X 5 μm. 56

19. AFM cross section curves of POSS-modified films after SVA-TA. Ph-POSS (A1) DMT modulus image and (A2) current image; SH-POSS (B1) DMT modulus image and (B2) current image. White line indicates cross-section analyzed. The scale of all images is 5 μm X 5 μm. 60

20. (A1) 5 X 5 μm DMT modulus image, (A2) 500 X 500 nm DMT modulus image, and (A3) the corresponding 500 X 500 nm height image of the P3HT:PCBM film after SVA-TA; (B1) 5 X 5μm DMT modulus image, (B2) 500 X 500 nm DMT modulus, and (B3) the corresponding 500 X 500 nm height image of the Ph-POSS modified P3HT:PCBM film after SVA-TA (C1) 5 X 5 μm DMT modulus image, (C2) 500 X 500 nm DMT modulus image, and (C3) the corresponding 500 X 500 nm height image of the SH-POSS modified P3HT:PCBM film after SVA-TA. .61

21. (A1) height image (A2) the corresponding DMT modulus image and (A3) current image of the Ph-POSS modified film after SVA; (B1) height image (B2) the corresponding DMT modulus image and (B3) current image of the SH-POSS modified film after SVA. The scale of all images is 5 μm X 5 μm. 63

22. UV-Vis spectra of the neat P3HT:PCBM film, the SH-POSS modified film and the Ph-POSS modified film with SVA and SVA-TA. 65

23. UV-vis absorption curves of Ph-POSS and SH-POSS in THF (0.001 g POSS in 1 mL THF). 66

24. Fluorescence spectra of neat P3HT:PCBM, SH-POSS modified, and Ph-POSS modified films with SVA and SVA-TA. 67

25. I-V curves of (a) devices with only solvent vapor annealing and (b) devices with both solvent vapor and thermal annealing.....69

26. Box charts depicting the variability in device characteristics of cells that underwent both SVA and TA. (Bottom star is the 1st percentile, top star is the 99th percentile, top line of the box is the 75th percentile, medium line of the box is the median, bottom line of the box is the 25th percentile, and solid square is the mean) 71

27. J-V curves of devices prepared under varying combinations of annealing and air exposure. 90

28. Box plots of measured parameters for devices prepared under different conditions of annealing and air exposure. (The bottom star represents the 1st percentile, the top star is the 99th percentile, the top line of the box is the 75th percentile, the central line of the box is the median, the bottom line of the box is the 25th percentile, and the solid square within the box is the mean) 71

29. J-V curves of devices prepared with SVA and SVA-TA annealing. 93

30. XRD curves of samples prepared with different annealing processes. 95

31. UV-vis spectra of samples prepared with different annealing processes. 95

32. AFM height images of samples with (A) no annealing, (B) TA, (C) SVA, and (D) SVA-TA. Z-scale for all images is 50 nm. 96

33. DMT modulus images of films produced with: (A) no annealing, (B) TA, (C) SVA, and (D) SVA-TA. 98

34. Device performance characteristics as a function of aging time in air for devices prepared under different annealing conditions, and recovery after thermal annealing. 99

35. XRD spectra of the degraded and reannealed SVA-TA devices. 100

36. UV-vis spectra of the degraded and reannealed SVA-TA devices. 101

37. AFM images of SVA-TA samples at the (A) first day, (B) 4 days, (C) 30 days and (1) reannealing. A1-D1 are the height images corresponding to 5 μm DMT modulus images of A2-D2. A3-D3 are 500 nm DMT modulus images taken from small sections of A2 – D2. 104

CHAPTER I

INTRODUCTION

Polymeric Photovoltaic Cells

Development of Organic Photovoltaic Cells

Development of sustainable, clean energy sources is one of the greatest challenges for scientists and engineers in the 21st century. Fossil fuels such as petroleum, coal, and nature gas have dominated the energy supplies for decades and greatly accelerated the development of human society. However, due to concerns about climate change and the conflict between the rising demand for energy and the decreasing deposits of natural resources, there is interest in developing clean, affordable, alternative energy sources to reduce dependency on fossil fuels. Sunlight, as an attractive alternative to fossil-based energy sources, is clean, abundant, sustainable, and widely available. The National Academy of Engineering has identified "making solar energy affordable" as the first of its "Grand Challenges for Engineering." [1] However, current technologies aimed at harnessing sunlight to meet large-scale energy needs are not cost competitive with fossil fuel-based approaches. The total solar energy absorbed by the earth is approximately 3,850,000 exajoules (EJ) per year.[2] This level of absorbance corresponds to more energy absorbed in one hour than was used by the entire globe for a full year, based on 2002 statistics.[3] It has been estimated that solar energy could provide the essential power for the entire world at an efficiency rate of only 10% per unit cell spread across as little as 0.1% of the available land on earth.[4]

Photovoltaic devices, or solar cells, transform solar energy into electrical energy. Alexandre Edmond Becquerel is credited with the first report of the photovoltaic effect in

a conductive solution in 1839, but the first practical photovoltaic device was not developed until 1954, when Bell Laboratories reported the first silicon based p-n junction with an efficiency of approximately 6%. Silicon-based photovoltaic devices then underwent intense development, with the structure evolving from two junctions to four or more junction and the efficiency increasing to 40%. Because of their relatively high efficiency, most commercially available photovoltaic devices in the market today are silicon-based. Thin silicon-based photovoltaic panels were developed to address the weight and difficult installation of traditional panels. Polymer-based organic photovoltaic (OPV) devices are attractive due to ease of fabrication, low-weight, flexibility, and potential reduction in cost. Polymeric OPV devices have enhanced stability in comparison to OPV devices formed from small organic molecules and have thus been under rapid development. Polymeric OPV devices can be solution processed into thin films using high throughput production methods such as roll-to-roll printing and inkjet printing.[5] Ultimately, if scientific and technical challenges are overcome, polymeric solar devices will be printed as flexible sheets and cut as required, thus greatly reducing processing costs and broadening solar power applicability.

Advantages of Polymeric Solar Cells

Conjugated polymers have intrinsic structural advantages in light absorption. Figure 1 shows a schematic of the electron structure of conjugated polymers. Conjugated polymers contain a mixture of σ-bonds and π-bonds. The top of the π-band is referred as the highest occupied molecular orbital (HOMO) and the bottom of the π*-band is referred as the lowest unoccupied molecular orbital (LUMO). The energy difference between the HOMO and LUMO is defined as the band gap, which determines the light absorption of

conjugated polymers. The band gap of conjugated polymers is usually between 1.5-2.5 eV, corresponding to the visible light range. [6] Thus, conjugated polymers are able to absorb visible light without breaking covalent bonds in the polymer molecules. In fact, the unique band gap characteristics of the conjugated structures also provide polymeric photovoltaic cells with high absorption efficiency (10^5 cm^{-1}). [7] Thus, a thickness of only a few hundred nanometers is adequate for the polymeric photovoltaic cell to harvest all the visible light within the absorption range.[6]

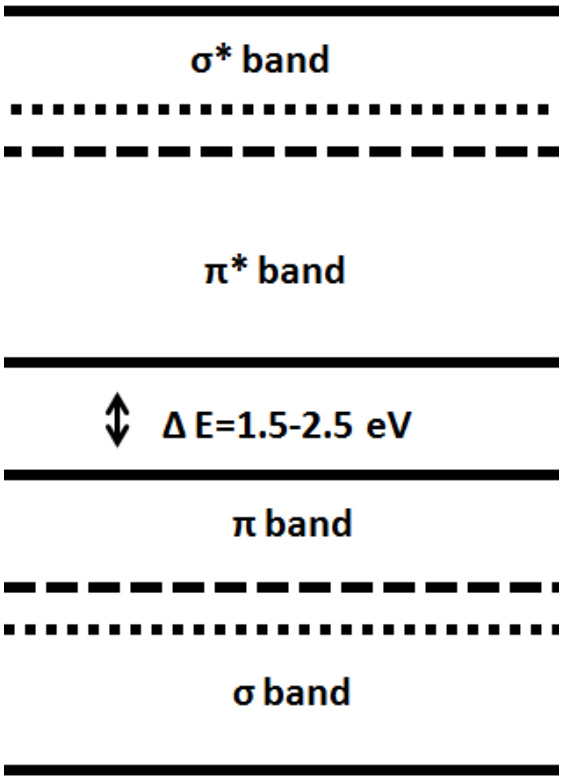

Figure 1. Energy diagram of conjugated polymers (adapted from Figure 10.1 in reference 6).

Working Mechanism of OPV

A typical polymer-based OPV device consists of a conjugated semiconducting polymer as the donor and a fullerene derivative as the acceptor. The working mechanism of a photovoltaic cell transforming light energy into electricity can be divided into four

steps, as illustrated in Figure 2.[8] When the light is absorbed by the donor, the electrons are excited to a higher energy level, leaving holes with opposite charges in the form of electron-hole pairs (excitons). Due to the low dielectric constant of the electron-hole pairs, an additional energy supply, the acceptor material, is required for the excitons to be dissociated into free charge carriers. For this process to occur, the excitons must move to the interface of the donor and acceptor phases before recombination occurs. At the interface, the excitons are dissociated into free charge carriers. Then the electrons jump from the LUMO level of the donor to the LUMO level of the acceptor, while the holes move to the HOMO level of the donor to accomplish the charge transfer. Finally, the electrons and holes are collected by the electrodes to be used.

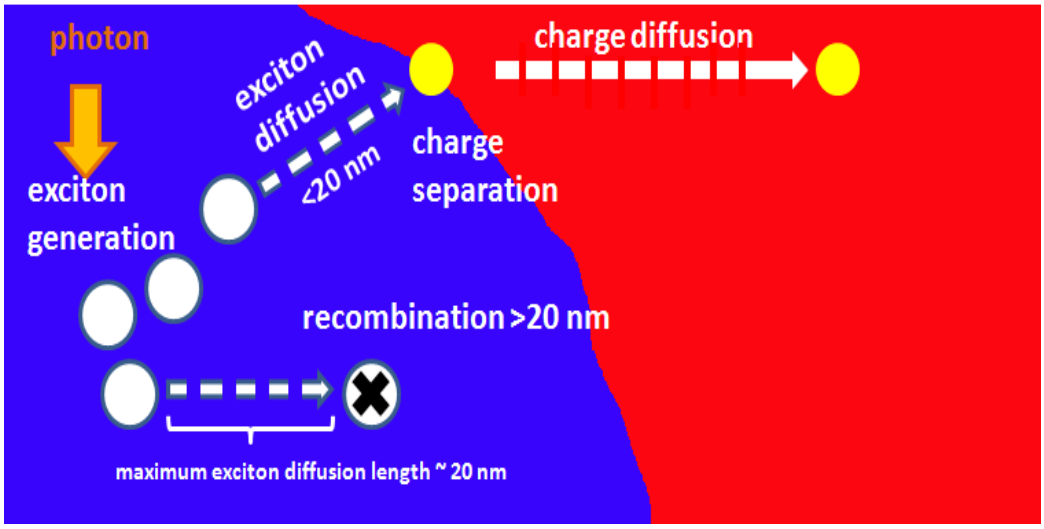

Figure 2. Schematic operation of OPV cells (adapted from Figure 6 in reference 29).

Polymer Donor Materials

Poly(phenylene vinylene) (PPV) and polythiophene (PT) derivatives are the most widely used donor materials in OPV devices. A few examples of conjugated polymers used in polymeric OPVs are shown in Figure 3. One of the biggest advantages of

polymeric solar cells is the structural tunability, which provides conjugated polymers with improved solubility, tunable band gap, and controllable morphology. Compared with the poorly soluble PPV, the MEH-PPV with alkane groups presents great solubility in organic solvents.[9] After incorporation of more rigid structures into the MEH-PPV backbone, higher molecular weight of M3EH-PPV is achievable. The promoted molecular weight has been found to increase glass transition temperature and doubled zero-field mobility of the conjugated polymer.[10] However, PPV based polymeric donor materials display low power conversion efficiency (2%) in OPV devices because of the mismatch between light absorption spectra and the solar irradiation spectrum. [11] In general, low band gap conjugated polymers are desirable to generate broad light absorption and high efficiency. Poly(3-hexylthiophene-2,5-diyl) (P3HT) is the most successful and widely studied electron donor material in OPVs to date . Compared with M3EH-PPV (band gap ~ 2.4 eV),[12] a broader range of light absorption and higher hole mobility are achieved in P3HT with a decreased band gap of around 2.2 eV.[13] The best power conversion efficiency in P3HT based OPV devices has been reported to be ~ 4%. Studies on lower band gap polythiophene derivatives have also been conducted. By adding a conjugated side chain to the thiophene group, a lower band gap PTZV-PT is obtained (band gap ~2.0 eV).[14] However, the device performance is not comparable to that of P3HT, because of poorerpolymer chain packing, phase separation, and crystallinity. A new synthetic method involving alternating donor-acceptor repeating units has been developed recently to obtain low band gap polymers. The mixed band gap of donor and acceptor units provides PTB7 with a lower band gap ~1.7 eV,[15] and power conversion efficiency of 7.4% has been achieved in a PTB7 based OPV device.[16]

Nevertheless, the complicated synthesis and high cost limit the current application of donor-acceptor polymers.

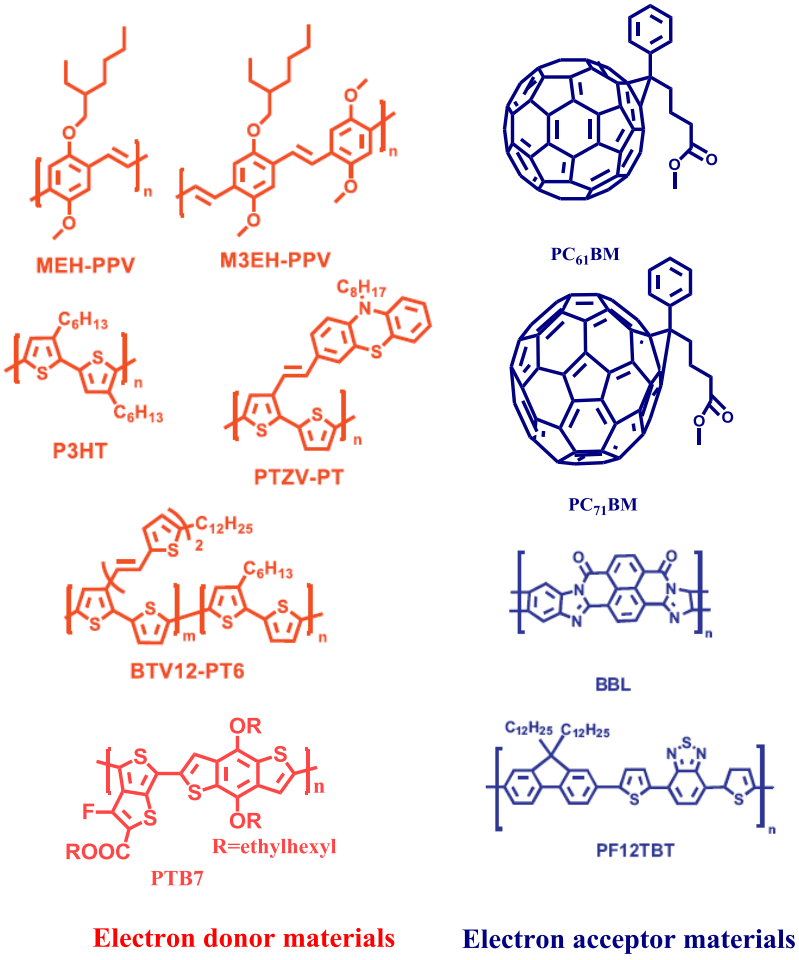

Figure 3. Examples of typical electron donor and acceptor materials in OPV cells.

OPV Acceptor Materials

Conjugated polymers would not generate electrical power unless electron acceptor species were involved. A good acceptor should have two properties: lower energy levels (HOMO and LUMO) than the donor to dissociate excitons and high electron mobility to transport electrons. A few examples of electron acceptor materials are shown in Figure 3. Among these materials, fullerene derivatives are the most widely used acceptor materials in OPV devices. The π-π conjugated, electron rich structure

provides fullerenes with a LUMO level of ~4.0 eV, which is lower than that of most polymeric donors. At the same time, the HOMO level of fullerenes (~6.3 eV) is also low enough to avoid internal energy waste during electron transfer. [17] Furthermore, fullerenes have a high electron mobility (~ $4X10^3$ cm^2/Vs).[18] Thus, fullerenes are able to serve as electron acceptor materials for most polymeric donors. Among the fullerene derivatives, [6,6]-Phenyl C_{61} butyric acid methyl ester (PCBM) is the mostly widely utilized in OPV devices. The organic functionality improves solubility in many organic solvents, such as dichlorobenzene, chlorobenzene, chloroform, and THF. A large number of solution processed OPV devices have been reported based on PCBM.

Parameters to Evaluate the Performance of OPV Devices

Parameters used to characterize the performance of OPV cells are illustrated in Figure 4,[4] which displays current(I)-voltage(V) curves for a cell measured in the dark and under illumination. V_{OC} and I_{SC} are the open circuit voltage and short circuit current, respectively. V_{OC} is the voltage when there is no current flowing through the cell. V_{oc} is linearly proportional to the energy gap between the HOMO level of the donor and the LUMO of the acceptor. Thus a good energy match between donor and acceptor materials provides high $V_{oc.}$ I_{sc} is calculated when the voltage is equal to zero. I_{sc} is determined by the external quantum efficiency, which is an overall consideration of light absorption, exciton dissociation at the donor/acceptor interface and electron collection at the electrodes. Power, P, is defined as P=I*V. The fill factor (FF) is a measure of the quality of the cell. It is calculated from the ratio of the maximum power, $P_{m,out}$, to the theoretical power, $P_t=V_{oc}*I_{sc}$ ($FF=P_{m,out}/P_t$). $P_{m,out}$ is shown graphically in Figure 4. P_t is described graphically by the rectangle formed by connecting perpendiculars from V_{oc} and I_{sc}. FF

indicates the quality of diode property in the OPV devices. The power conversion efficiency (PCE) is the ratio of the maximum power to the input power, normally referred as efficiency. A high quality OPV cell should possess high values of V_{oc}, I_{sc}, FF, and PCE simultaneously.

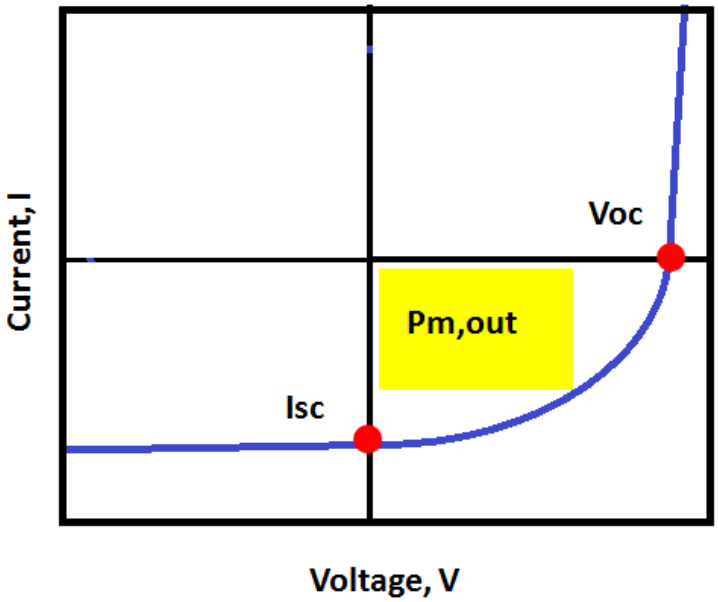

Figure 4. Current-voltage (I-V) characteristics of an OPV cell (adapted from Figure 3 in reference 19).

Structures of OPV Devices

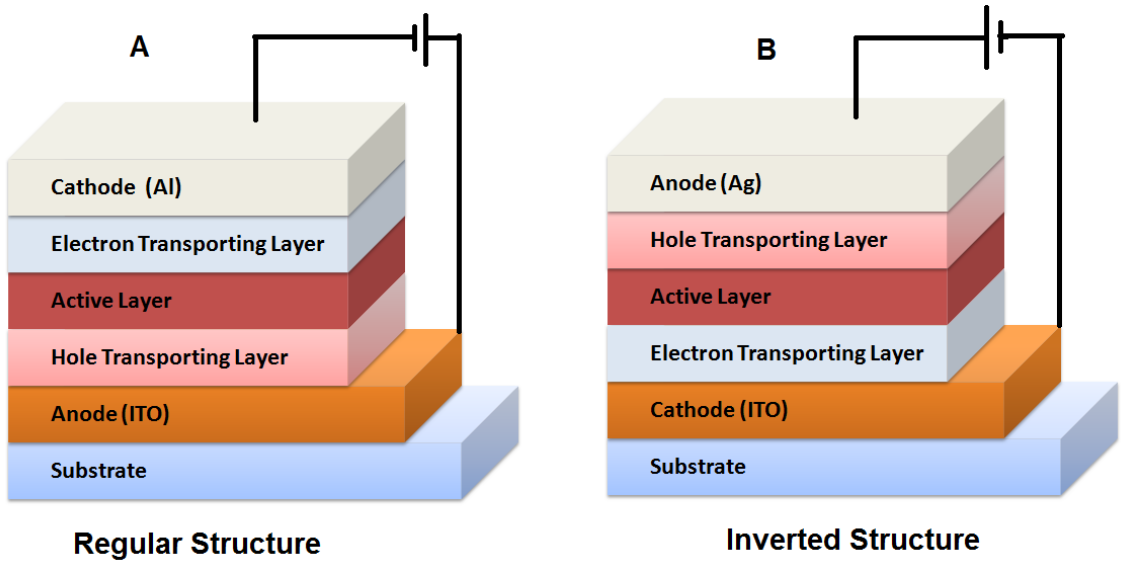

Figure 5. Schemes of (A) regular structure and (B) inverted structure.

Two types of device structures are defined in the literature, regular structure and inverted structure, as illustrated in Figure 5. In both of the structures, a transparent substrate is required to support the OPV device, such as a glass slide as a hard substrate or a polymer film as a flexible substrate. In a regular structure, indium tin oxide (ITO) is coated on top of the substrate as the anode, while low work function metal materials such as aluminum (Al) are thermally deposited on top of the device as the cathode. The active layer consisting of donor and acceptor is sandwiched between the electrodes. When the device is working, the holes move from the active layer to the cathode, while the electrons move towards the anode. In an inverted structure, a high work function metal such as Ag serves as the anode and ITO serves as the cathode. The current goes in the opposite direction as compared with the regular structure. Because Ag has higher oxidation resistance than Al, inverted structures show longer lifetimes than those of the

regular structure. However, the energy level mismatch between the active layer and the anode decreases the performance slightly in the inverted structure.[19]

Interfacial Layers

Interfacial layers play an important role in OPV devices to minimize the energy barrier between the active layer and the electrodes. A low energy barrier is required to facilitate charge transfer by promoting the tunneling current. Two interfacial layers, a hole transport layer and an electron transport layer are generally employed in OPV devices. A hole transport layer is a functional thin film facilitating hole transport to the cathode and blocking electron injection to the anode, while an electron transport layer favors the electron extraction and blocks the hole transport. Poly(3,4-ethylenedioxythiophene)-poly(styrenesulfonate) (PEDOT:PSS) is the most widely used hole transport material. PEDOT is a conjugated polymer with strong electron donating groups on the polythiophene backbone. Because of the electron rich structure, PEDOT can effectively block electron movement in the devices. At the same time, the excellent transparency of PEDOT reduces the light absorption from the interfacial layer, which enables more visible light to get to the donor/acceptor materials. After incorporation of hydrophilic PSS as the counter ion, PEDOT:PSS can be well dispersed in aqueous solution. The PEDOT:PSS solution can be easily spin coated on top of the electrodes to form a uniform hole transport layer. In a PEDOT:PSS incorporated P3HT:PCBM system, the V_{oc} increased by 1.6% and the PCE increased by 45% of the original values.[20]

Heterojunction System

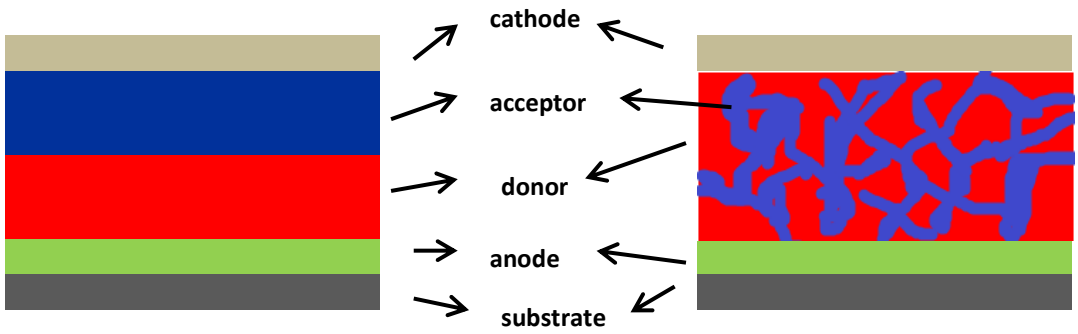

(a) (b)

Figure 6. Schematic structures of (a) bilayer heterojunction and (b) bulk heterojunction (adapted from Figure 2 in reference 19).

The development of OPV devices underwent two generations, bilayer and bulk heterojunctions, classified by the geometrical structures of the photoactive layer and illustrated in Figure 6.[8] In the bilayer heterojunction model (Figure 6a) the active layer, consisting of separate donor and acceptor materials, is sandwiched between the anode and the cathode. The donor material is evaporated or cast onto the anode and the acceptor layer is deposited on top of the donor. The first bilayer OPV device was fabricated in 1986 based on a copper phthalocyanine and a perylene tetracarboxylic derivative. The efficiency of this device was reported to be as high as 1%. [21] Then new materials based on bilayer structures were sequentially applied in OPV devices. Based on the OPV operation theory, current is generated at the donor/acceptor interface rather than within the bulk. The exciton diffusion length is the maximum length that the exciton can travel inside of the materials before recombination. If the domain size of the donor and acceptor phases is larger than the exciton diffusion length, only the excitons close to the donor/acceptor interface will contribute to the power conversion efficiency while the

remaining excitons will combine and radiate photons. In general, the diffusion length for conjugated polymers is 10-20 nm and the required thickness of the materials to absorb maximum light energy within the absorption spectrum is an order of magnitude higher.[22] It is thus difficult to obtain high efficiency in the bilayer model OPV system.

During the research of bilayer structures, interlayer diffusion was discovered at the donor/acceptor interface, with increment of performance.[23,24] The idea of penetration of donor/acceptor materials leads to the development of heterojunction structures. The bulk heterojunction system utilizes a phase segregated mixture of donor and acceptor materials sandwiched between the electrodes (Figure 6b). Phase separation results from the different crystallization rates of the conjugated polymer and the fullerene derivative. Through optimization of the film preparation processes, it is possible to control domain size close to that of the exciton diffusion length, to yield maximum efficiency on exciton dissociation. Annealing processes, including thermal annealing, solvent vapor annealing and solvent annealing, are utilized to control phase separation, optimize domain size, increase crystallinity, and decrease energy level differences in the active layer.[25-27]

Morphology Control in OPV

The ideal morphology to achieve maximum efficiency in organic solar cells consists of separate donor and acceptor strip-like domains perpendicular to the electrodes. The excitons are dissociated into holes and electrons at the donor/acceptor interface. Holes travel through the donor domains to the anode and electrons travel through the acceptor domains to the cathode.[28] However, due to technical difficulties, the ideal model has not been achieved. The bulk heterojunction morphology with small domain size that generates sufficient surface area has so far proved to provide the best performance.

Dadmun proposed a "rivers and streams model," in which the phase separated morphology of the standard P3HT:PCBM system was studied by small angle neutron scattering. [29] In this model, the photoactive layer contains crystallized P3HT, crystallized PCBM, and an amorphous P3HT/PCBM mixture. The amorphous P3HT and PCBM serve as rivers that generate excitons. Because the charge transfer in the amorphous mixture is limited, the crystallized P3HT and PCBM embedded in the amorphous mixture serve as streams to transport holes and electrons, respectively. In the rivers and streams model, the film morphology is highly influenced by the ratio of the P3HT and PCBM. When the PCBM content was less than 20%, the photoactive films showed no phase separation. Even after being thermal annealed at 150 ℃ for 6 hours, the annealed films presented similar characteristics as the as-cast film. However, when the content of the PCBM was increased to 50%, the films subjected to the thermal annealing showed crystallized P3HT and PCBM, which served as streams to facilitate the charge transfer.

Thermal annealing was first introduced into photovoltaic cells by Padinger et al., resulting in substantial increases in the power conversion efficiency.[30] In the thermal annealing process, the OPV cells are heated above the T_g of P3HT to allow molecular reorganization. In general, OPV cells that have not been subjected to annealing processes display little phase separation and thus demonstrate low power conversion efficiencies and fill factors.[31] On thermal annealing, both the P3HT and PCBM molecules are reorganized into thermodynamically favored crystallized structures. Due to the lower crystallization rate of PCBM at the initial thermal annealing stage, thermal annealing results in the formation of fiber-like P3HT crystallites in a matrix consisting of PCBM clusters and amorphous P3HT.[32] The annealing-induced P3HT crystallized domains not

only adjust the phase separation degree in accordance with the exciton diffusion length but also decrease the space between P3HT chains to facilitate the charge transport inside P3HT domains.[33] Also, the annealing was found to decrease the band gap difference between electrodes and the active layer, which theoretically should increase the efficiency. It was found that PCE as high as 5% could be obtained after thermal annealing.[35] It was reported by Russell and co-workers that a bicontinuous interconnected P3HT:PCBM phase separated morphology with 10 nm domain size was formed within seconds after thermal annealing, as determined by small angle neutron scattering and high resolution transmission electron microscopy studies. [34] Oriented P3HT was discovered at the interface between the photoactive layer and the cathode. The oriented structures displayed a fine crystalline structure in near edge x-ray absorption studies, which was thought to facilitate the hole transport at the interface.

Solvent annealing refers to control of the solidification time of the wet sample before deposition of the cathode. Yang et al. reported that films produced at a fast rate (film dried in 20 s) yielded smooth surfaces with PCE of 1.36%, while films grown at a slow rate (in 20 minutes) yielded a ten-fold increase in roughness and PCE of 3.52%.[36] Using the slow film growth process, the resistance of the photovoltaic film decreased from 19.8 $\Omega*cm^2$ to 2.4 $\Omega*cm^2$. The increased PCE and decreased resistance were believed to be caused by the higher crystallinity in the films produced at slow rate, which greatly influences the ordering of the P3HT chains. Further study showed that solvent annealing followed by thermal annealing at 110 ^oC for 10 min increased the efficiency of the cell to 4.4%. [36]

The solvent vapor annealing method involves treatment of the photovoltaic film with solvent vapor to increase the mobility of polymer chains to enhance crystallization and phase separation. The resulting morphology and crystallinity of the films are directly related to the type of solvent employed. Good solvents are expected to allow greater chain mobility than poor solvents, and the penetration rate of the solvent is dependent on its boiling point. However, too much chain mobility may result in large-scale phase separation and exciton loss. Thus, it is necessary to optimize solvent type and annealing time to achieve the desired morphology. [27]

Studies have been reported of incorporation of nanoparticles as additives to OPV systems with the goal of increasing efficiency, with varying results. Berson et al. reported that carbon nanotubes increased the short circuit current of a P3HT:PCBM cell by a factor of two, which leads a higher power conversion efficiency.[37] Chul-Hyun Kim et al. embedded silver nanowires into P3HT:PCBM systems and reported the elevation of overall performance in terms of open circuit voltage, short circuit current, fill factor, and power conversion efficiency.[38] Gold nanoparticles of 5 nm diameter with a ligand shell dispersed in P3OT/C_{60} blends were reported to elevate the performance of the photovoltaic cell.[39] However, gold nanoparticles incorporated in a P3HT:PCBM system resulted in aggregation leading to lower power conversion efficiency due to exciton loss.[39] The effects of nanoparticle incorporation on OPV cell performance depend on the dispersion, size, and interaction of the nanoparticles with the polymer matrix. These parameters are in turn affected by processing conditions and composition of the OPV cell.

Degradation of OPV

Even though OPV has experienced great development during the last few decades, the fast degradation of OPV is still a maro problem for industrial applications. Compared with silicon based inorganic solar cells that can last up to 20 years, [40] OPV devices based on PPVs are only able to maintain effectiveness for a few days. [41] Among the materials reported to date, P3HT:PCB- based devices show the longest lifetime, maintaining stable performance for one year.[42] Generally, there are two main degradation pathways in OPV devices: chemical degradation and physical degradation.

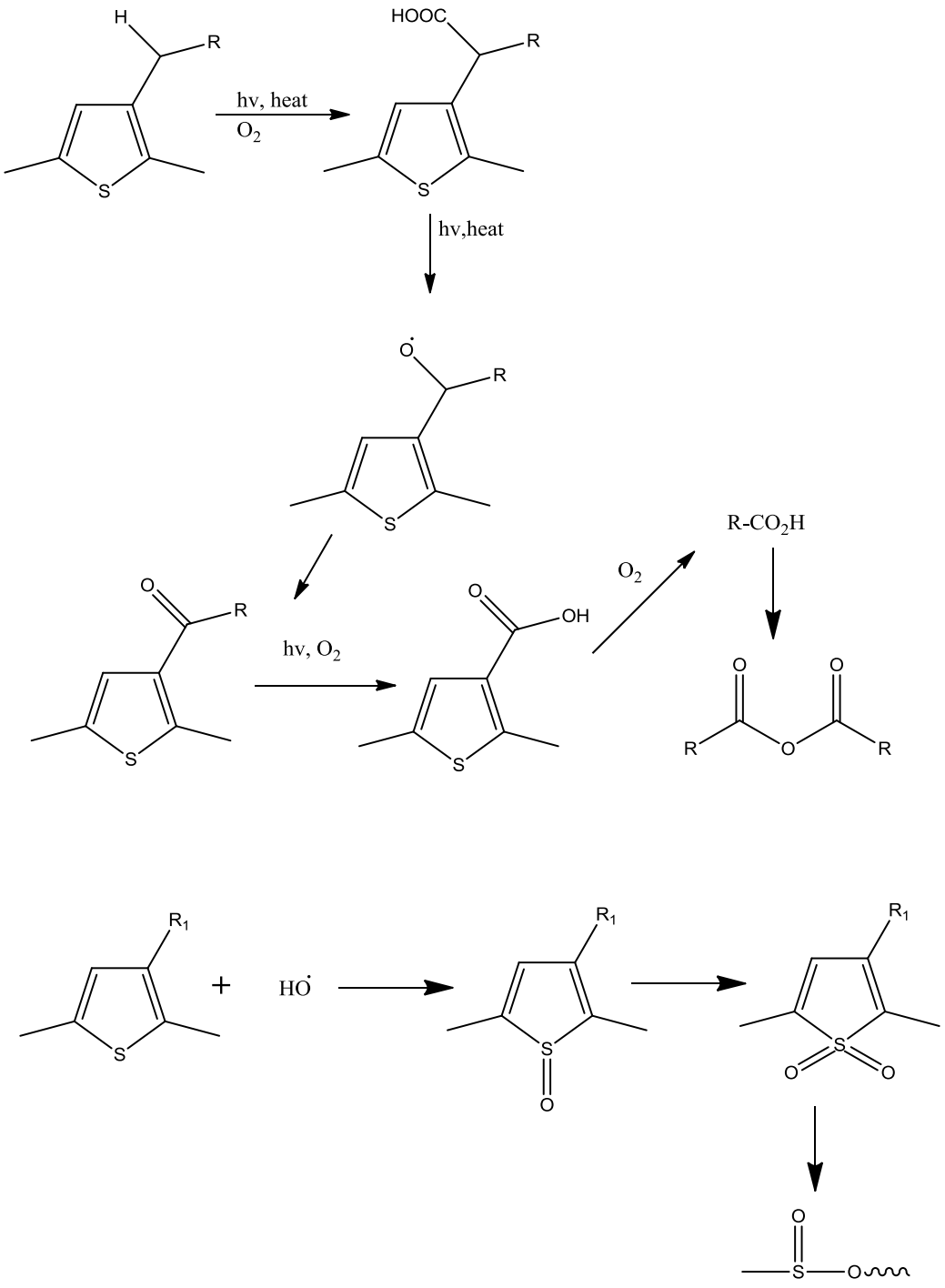

Figure 7. Chemical degradation of polythiophene derivatives (adapted from Scheme1 in reference 38).

Figure 7 shows a series of chemical degradation reactions of polythiophene derivatives.[43] Light, oxygen, and moisture are the main factors inducing chemical

degradations.[44] Exposure to UV light and oxygen leads to the oxidation of the alkyl groups, in which poly(acrylic acid thiophene) and non-conjugated small molecules are generated. In the presence of moisture, the conjugated thiophene rings are converted to linear structures. These chemical reactions result in irreversible damage to the conjugated polymers, leading to large decrements in conductivity, hole transport, and light absorption. In fact, a single factor among light, oxygen, and moisture will not degrade the OPV, but combined factors have been shown to accelerate the degradation process enormously. [45] In order to avoid chemical degradation, encapsulation is widely used. Encapsulation effectively protects the OPV devices from oxygen and moisture, which not only protects the photoactive layer but also prevents oxidation of the low work function electrode. [46]

Physical degradation also causes performance decrement. Phase separation or precisely controlled dimensions, close that that of the exciton diffusion length, is desirable to obtain devices with high efficiency. However, phase separation is a thermodynamic meta-stable state, which is time and temperature dependent. In the P3HT:PCBM heterojunction system, P3HT tends to form crystallized fibers and PCBM tends to aggregate and segregate to the surface. [47] When the domain size exceeds the exciton diffusion length, the performance will decrease over time.

Motivation and Goal of Research

OPV cells have undergone fast development during the last few decades. However, the power conversion efficiency is still lower than the commercial requirement. Control of phase separated morphology in the donor/acceptor system is one of the most important factors determining the performance of the OPV cells. The current is generated

at the interface of the donor/acceptor phases; thus, domain size close to the exciton diffusion length is desirable to achieve the maximum power conversion efficiency of the photoactive materials. Studies using nanoparticles have been conducted to control the nanomorphology in the donor/acceptor thin films. However, traditional nanoparticles such as gold and silver provide non-uniform particle sizes that lead to difficulty in obtaining reproducible results. Therefore, nanoparticles with uniform size and tunable chemical structures are hypothesized to provide better control of morphology and greater reproducibility.

Processing is also important in enhancing phase separation, controlling domain size, and promoting device performance. Film annealing is one of the most important processing steps controlling the morphology. Thermal annealing, solvent vapor annealing, and solvent annealing have been widely used to enhance phase separation and device performance. However, due to the environmental sensitivity of the photoactive materials, most devices are fabricated under inert gas protection to avoid degradation by oxygen and moisture. Even though many processing steps have been conducted under ambient environment, the total fabrication in air to produce high performance OPV devices has not yet been reported. Thus, the discovery of a method to manufacture OPV cells entirely in air is of great technical interest.

The goal of this research is to determine the potential for improving conversion efficiency in OPV devices through control of nanostructure in conductive polymer films. It is hypothesized that increased control of morphology of the systems on the nanoscale will provide pathways for enhancing photon-electron conversion allowing enhanced OPV efficiency. We propose to increase morphological control by introducing polyhedral

oligomeric silsesquioxane (POSS) nanostructured chemicals as additives into the poly(3-hexylthiophene-2,5-diyl) (P3HT) and [6,6]-phenyl C61 butyric acid methyl ester (PCBM) photoactive layer. It is hypothesized that POSS molecules will change the morphology and phase separation in the P3HT:PCBM system and that different POSS structures and functionalities will have differing effects. Phase separation and development of continuous structures are directly related to the power conversion efficiency. Additionally, POSS structures are expected to enhance crystallinity of the P3HT domains and thereby affect the charge distribution and transport pathways inside the system. Alternate processing and annealing methods will be applied to optimize efficiency of the photovoltaic cells.

References

(1) National Academy Engineering Home Page. *http://www.engineeringchallenges.org/cms/challenges.aspx* (aceessed May 1, 2011).

(2) Smil, V. *Energy: A Beginner's Guide*; Oxford: Oneworld Publications: London, 2006; pp 12.

(3) Morton, O. *Nature* **2006**, *443*, 19-22.

(4) Xue, J. *Polym. Rev.* **2010**, *50*, 411-419.

(5) Chason, M.; Gamota, D. R.; Brazis, P. W., Jr.; Kalyanasundaram, K.; Zhang, J.; Lian, K. K.; Croswell, R. *MRS Bull.* **2006**, *31*, 471-475.

(6) Skotheim, T. A.; Reynolds, J. R. *Handbook of Conducting Polymers*.CRC Press: Boca Raton, 2007; 10-1-10-31.

(7) Wienk, M. M.; Struijk, M. P.; Janssen, R. A. *Chemical Physics Letters* **2006**, *422*, 488-491.

(8) Liu, J. P3HT:PCBM Bulk Heterojunction Organic Solar Cell: Performance Optimization & Application of Inject Printing. Thesis, Linkopings University, May 2008.

(9) Quan, S.; Teng, F.; Xu, Z.; Qian, L.; Hou, Y.; Wang, Y.; Xu, X. *European Polymer Journal* **2006**, *42*, 228-233.

(10) Pfeiffer, S.; Hörhold, H. H. *Macromolecular Chemistry and Physics* **1999**, *200*, 1870-1878.

(11) Choy, W. C. H. *Organic Solar Cells : Materials and Device Physics.* Springer: London, 2013; pp 19.

(12) Chasteen, S. V.; Sholin, V.; Carter, S. A.; Rumbles, G. *Solar Energy Materials and Solar Cells* **2008**, *92*, 651-659.

(13) Heeney, M.; Zhang, W.; Crouch, D. J.; Chabinyc, M. L.; Gordeyev, S.; Hamilton, R.; Higgins, S. J.; McCulloch, I.; Skabara, P. J.; Sparrowe, D. *Chemical Communications* **2007**, 5061-5063.

(14) Sang, G.; Zou, Y.; Huang, Y.; Zhao, G.; Yang, Y.; Li, Y. *Applied Physics Letters* **2009**, *94*, 193302-193303.

(15) Švrček, V.; Yamanari, T.; Mariotti, D.; Matsubara, K.; Kondo, M. *Applied Physics Letters* **2012**, *100*, 223904.

(16) Liang, Y.; Xu, Z.; Xia, J.; Tsai, S. T.; Wu, Y.; Li, G.; Ray, C.; Yu, L. *Advanced Materials* **2010**, *22*, E135-E138.

(17) Wang, H.; He, Y.; Li, Y.; Su, H. *The Journal of Physical Chemistry A* **2011**, *116*, 255-262.

(18) Mihailetchi, V.; Wildeman, J.; Blom, P. *Physical Review Letters* **2005**, *94*, 126602.

(19) Brabec, C.; Scherf, U.; Dyakonov, V. *Organic Photovoltaics: Materials, Device Physics, and Manufacturing Technologies*; John Wiley & Sons: online, 2011; pp 329.

(20) Lee, S.-H.; Kim, J.-H.; Shim, T.-H.; Park, J.-G. *Electronic Materials Letters* **2009**, *5*, 47-50.

(21) Tang, C. W. *Applied Physics Letters* **1986**, *48*, 183-185.

(22) Zheng, Y.; Xue, J. *Polym. Rev.* **2010**, *50*, 420-453.

(23) Treat, N. D.; Brady, M. A.; Smith, G.; Toney, M. F.; Kramer, E. J.; Hawker, C. J.; Chabinyc, M. L. *Advanced Energy Materials* **2011**, *1*, 82-89.

(24) Chen, D.; Liu, F.; Wang, C.; Nakahara, A.; Russell, T. P. *Nano letters* **2011**, *11*, 2071-2078.

(25) van, B. S.; de, W. G.; Sourty, E.; Loos, J.; *Nano letters* **2009**, 9, 507-513.

(26) Salim, T.; Yin, Z.; Sun, S.; Huang, X.; Zhang, H.; Lam, Y. M. *ACS Appl. Mater. Interfaces* **2011**, *3*, 1063-1067.

(27) Park, J. H.; Kim, J. S.; Lee, J. H.; Lee, W. H.; Cho, K. *J. Phys. Chem. C* **2009**, *113*, 17579-17584.

(28) Yang, X.; Loos, J. *Macromolecules* **2007**, *40*, 1353-1362.

(29) Yin, W.; Dadmun, M. *Acs Nano* **2011**, *5*, 4756-4768.

(30) Padinger, F.; Rittberger, R. S.; Sariciftci, N. S. *Adv. Funct. Mater.* **2003**, *13*, 85-88.

(31) Yang, X.; Loos, J.; Veenstra, S. C.; Verhees, W. J. H.; Wienk, M. M.; Kroon, J. M.; Michels, M. A. J.; Janssen, R. A. J. *Nano Lett.* **2005**, *5*, 579-583.

(32) Salamandra, L. Organic Photo-Voltaic Cells and Photo-Detectors based on Polymer Bulk-Heterojunctions. Ph.D. Thesis, University of Rome Tor Vergata, July 2009.

(33) Chang, Y.-M.; Wang, L. *J. Phys. Chem. C* **2008**, *112*, 17716-17720.

(34) Ma, W.; Yang, C.; Gong, X.; Lee, K.; Heeger, A. J. *Adv. Funct. Mater.* **2005**, *15*, 1617-1622.

(35) Chen, D.; Nakahara, A.; Wei, D.; Nordlund, D.; Russell, T. P. *Nano letters* **2010**, *11*, 561-567.

(36) Li, G.; Shrotriya, V.; Huang, J.; Yao, Y.; Moriarty, T.; Emery, K.; Yang, Y. *Nat. Mater.* **2005**, *4*, 864-868.

(37) Berson, S.; de, B. R.; Bailly, S.; Guillerez, S.; Jousselme, B. *Adv. Funct. Mater.* **2007**, *17*, 3363-3370.

(38) Kim, C.-H.; Cha, S.-H.; Kim, S. C.; Song, M.; Lee, J.; Shin, W. S.; Moon, S.-J.; Bahng, J. H.; Kotov, N. A.; Jin, S.-H. *ACS Nano* **2011**, *5*, 3319-3325.

(39) Topp, K.; Borchert, H.; Johnen, F.; Tunc, A. V.; Knipper, M.; von, H. E.; Parisi, J.; Al-Shamery, K. *J. Phys. Chem. A* **2010**, *114*, 3981-3989.

(40) Staebler, D. L. *Reliability, IEEE Transactions on* **1982**, *31*, 281-284.

(41) Jørgensen, M.; Norrman, K.; Krebs, F. C. *Solar Energy Materials and Solar Cells* **2008**, *92*, 686-714.

(42) Hauch, J. A.; Schilinsky, P.; Choulis, S. A.; Childers, R.; Biele, M.; Brabec, C. J. *Solar Energy Materials and Solar Cells* **2008**, *92*, 727-731.

(43) Manceau, M.; Rivaton, A.; Gardette, J.-L.; Guillerez, S.; Lemaître, N. *Polymer Degradation and Stability* **2009**, *94*, 898-907.

(44) Grossiord, N.; Kroon, J. M.; Andriessen, R.; Blom, P. W. *Organic Electronics* **2012**, *13*, 432-456.

(45) Hintz, H.; Egelhaaf, H.-J.; Lüer, L.; Hauch, J.; Peisert, H.; Chassé, T. *Chemistry of Materials* **2010**, *23*, 145-154.

(46) Reese, M. O.; Morfa, A. J.; White, M. S.; Kopidakis, N.; Shaheen, S. E.; Rumbles, G.; Ginley, D. S. *Solar Energy Materials and Solar Cells* **2008**, *92*, 746-752.

(47) Ray, B.; Alam, M. A. *Applied Physics Letters* **2011**, *99*, 033303.

CHAPTER II

ELUCIDATION OF THE EFFECTS OF POSS STRUCTURE ON MORPHOLOGY AND PHOTOPHYSICAL CHARACTERISTICS OF PHOTOACTIVE POLYMER FILMS

Abstract

Polymeric photovoltaic cells have attracted significant attention due to their ease of processability, flexibility, and tunability of structure. The photoactive thin layer of polymeric photovoltaic cells generally contains a conjugated polymer as the donor and a fullerene derivative as the acceptor. Controlling the phase separation between donor and acceptor is of great importance in determining the performance of photovoltaic cells. Strategies including using nanoparticles and changing processing conditions have been widely utilized to optimize the phase separation. However, most nanoparticles utilized in the photovoltaic systems are conductive materials that are multi-disperse in size, which increases the chance of short circuiting between the electrodes. POSS molecules are monodisperse hybrid organic-inorganic nanostructured chemicals that are generally non-conductive. In this study, POSS molecules with different functional groups were incorporated into a polymeric photovoltaic active layer film to control the phase separation. POSS functionality was varied in an attempt to control the self-assembly of the donor/acceptor phases. High resolution AFM was utilized to investigate the surface morphology and phase separation. Photoactive films were also investigated using UV-vis spectroscopy and X-ray diffraction.

Introduction

Development of sustainable, clean energy sources is one of the greatest challenges for scientists and engineers in the 21st century. The National Academy of Engineering has identified "making solar energy affordable" as the first of its "Grand Challenges for Engineering." [1] Polymer-based OPV devices are attractive due to ease of fabrication, low-weight, flexibility, and potential reduction in cost. An effective polymer-based photovoltaic cell consists of both a conjugated semiconducting polymer as the donor and a fullerene derivative as the acceptor. One of the most widely studied polymeric photovoltaic systems is a phase separated blend of P3HT and PCBM (Figure 8). When a photovoltaic cell is working, a photon is absorbed by the P3HT which turns the photon into an exciton. The exciton is dissociated into free charge carriers at the donor/acceptor interface and collected as electrical energy. The formation of large domain sizes that exceed the exciton diffusion length will cause exciton recombination prior to their dissociation into free charge carriers. Weak phase separation will lead to poor charge transport between the donor and acceptor interfaces.[2] Therefore, it is of paramount importance to control the domain size close to the exciton diffusion length and form continuous structures to facilitate the charge transport across the bulk heterojunction.

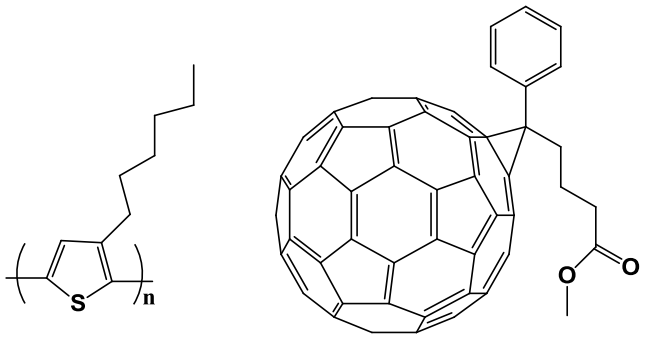

P3HT **$PC_{61}BM$**

Figure 8. Structures of P3HT and PCBM.

Efforts on improving the processing conditions have been made to control the phase separation of the P3HT:PCBM heterojunction system. Thermal annealing was first introduced into photovoltaic cells by Padinger et al., resulting in substantial increases in the power conversion efficiency.[3] In the thermal annealing process, the OPV cells are heated above the T_g of P3HT to allow molecular reorganization. In general, OPV cells that have not been subjected to annealing processes display little phase separation and thus demonstrate low power conversion efficiencies and fill factors.[4] On thermal annealing, both the P3HT and PCBM molecules are reorganized into thermodynamically favored crystallized structures. Due to the lower crystallization rate of PCBM, thermal annealing results in the formation of fiber-like P3HT crystallites in a matrix consisting of PCBM clusters and amorphous P3HT.[5] The annealing-induced P3HT crystallized domains not only adjust the degree of phase separation in accordance with the exciton diffusion length but also decrease the space between P3HT chains to facilitate the charge transport inside P3HT domains.[6] Also, the annealing was found to decrease the band gap difference between electrodes and the active layer, which increases the efficiency.

Studies have been reported of incorporation of nanoparticles as additives to OPV systems with the goal of increasing efficiency, with varying results. Berson et al. reported that carbon nanotubes increased the short circuit current of P3HT:PCBM cell by a factor of two, which leads to a higher power conversion efficiency.[7] Chul-Hyun Kim et al. embedded silver nanowires into P3HT:PCBM systems and reported the elevation of overall performance in terms of open circuit voltage, short circuit current, fill factor, and power conversion efficiency.[8] The effects of nanoparticle incorporation on OPV cell performance depend on the dispersion, size, and interaction of the nanoparticles with the polymer matrix. However, it is important to control the particle size, since large conductive particles could cause short circuiting between electrodes and loss of efficiency. POSS nanostructructured chemicals are hybrid organic-inorganic structures, monodisperse in size, consisting of a silicon oxide cage with a corona of organic substituents. Previous studies in our laboratories have shown that the migration and aggregation behavior of POSS molecules can be controlled in polymeric matrices to produce desired nanostructure development with associated performance improvements,[9,10] and POSS molecules can be tailored to serve as dispersing agents for organic and metallic nanoparticles.[11] POSS is also utilized to control the morphology and phase separation in polymers.[12] In our previous study, it has been found that by changing the pendant functional groups on the POSS organic corona, POSS molecules act to either drive phase separation or to improve compatibility in phase separated systems.[13] In this study, POSS molecules with different functional groups were introduced into the P3HT:PCBM system in an attempt to control the phase separation. Atomic force microscopy (AFM) was utilized to determine the morphology and nanoscale phase

separation. The P3HT crystallinity was characterized by UV-vis spectroscopy and X-ray diffraction (XRD).

Experimentation

Materials

ITO glass slides were cut into ~ 1.5 X 1.5 cm^2 squares. PEDOT:PSS, 1.3 wt.% dispersion in water, having resistivity in the range of 500-5000 ohm cm, was used as the hole transporter. P3HT, regioregular, electronic grade, 98 % regioregularity, average M_n ~ 45,000 was used as the donor. PCBM with purity >99% and molecular weight of 911 g/mol was used as the acceptor. Chlorobenzene was used as the solvent to form the actual photovoltaic donor/acceptor blend. All the materials above were purchased from Sigma Aldrich, USA. Octahydro POSS (H-POSS), tris sulfonic acid isobutyl POSS ($PhSO_3H$ POSS) and octa(3-hydroxy-3-methylbutyldimethylsiloxy) POSS (OH-POSS)were donated by Hybrid Plastics, Inc. All materials were used as received.

Sample Preparation

ITO (~100 nm) coated glass plates were successively cleaned ultrasonically in DI water, acetone, and isopropanol for 10 minutes each in a FS20D sonicator. They were then exposed to UV/ozone for 40 minutes and then immediately spin coated with a uniform layer of PEDOT:PSS. PEDOT:PSS was spin-coated at a speed of 5000 rpm (revolutions per minute) to form a 40 nm thick film. 25 mg/ml active layer solution having 1:1 wt. ratio of P3HT:PCBM in chlorobenzene was prepared for spin coating. The active layer was spin coated on top of the PEDOT:PSS layer at 1250 rpm for 90 sec using a WS-400B-GNDP/LITE spin coater. The thickness of the active layer was determined to be ~ 100 nm by AFM. The samples were then annealed at 150 °C in argon

for 30 min. to aid the crystallization process. The entire fabrication process was conducted in an air environment except for thermal annealing. The same experiments were repeated for 3 times to make sure reproducible results were obtained. Representative images and curves collected from these samples were shown in this study.

Instrumentation

AFM studies were conducted in tapping mode on a Dimension ICON scanning probe microscope from Bruker. A silicon probe from Bruker (RTESP) with nominal spring constant of 20-80 N/m was employed. Surface topographies of film samples were studied at different scan sizes at image resolution of 512 X 512 pixels and scan rate of 1 Hz. Multiple images were obtained of macroscopically separated areas of the surface, and representative images are shown. AFM studies were performed in a temperature (22±2 ℃) and humidity (40-45%) controlled room. UV-vis spectra were obtained using a Perkin-Elmer Lambda 6 UV/Vis spectrophotometer. All spectra were normalized to the intensity at 700 nm, where the absorption from P3HT or PCBM is not observable. X-ray diffraction studies were obtained using a Rigaku D/MAX-Ultima-III diffractometer at room temperature using Cu Kα radiation at a tube current of 44 mA and an acceleration voltage of 40 kV. Scan range was 4 °- 8 °at a step interval of 0.01 °and a scanning rate of 0.05 °/min.

Results and Discussion

In this study, three POSS structures with different functional groups were chosen for evaluation due to their expected range of interactions with the donor and acceptor phases. The structures of the POSS materials analyzed are shown in Figure 9. H-POSS, without organic functionality, was chosen to study the effect of the silicon-oxygen cage

alone. The hydroxy-terminated octa-substituted organosiloxy OH-POSS was chosen to examine the effect of potential hydrogen bonding with the PCBM ester. The $PhSO_3H$-POSS, with both hydroxyl and phenyl groups substituents was expected to have potential for both H-bonding and π-π interactions with the PCBM phase. POSS incorporation was limited to one wt% to avoid interference of the insulating POSS molecules with conductivity.

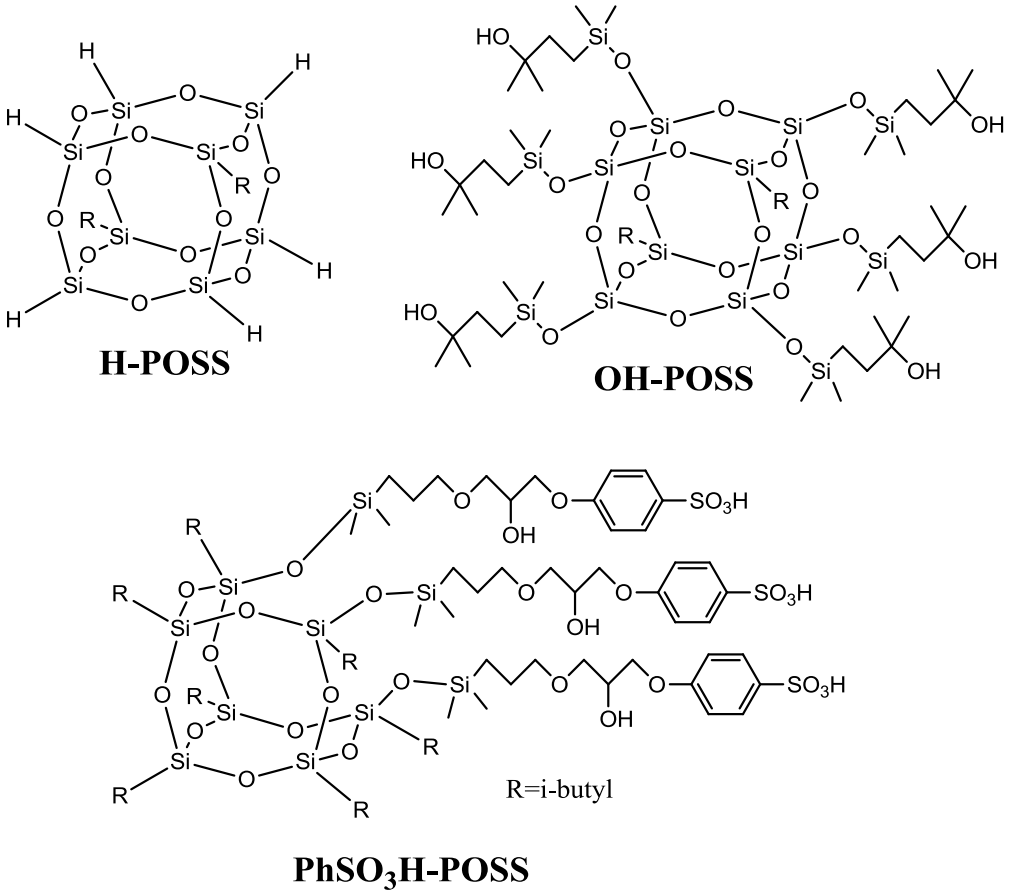

Figure 9. Structures of POSS molecules.

AFM Study

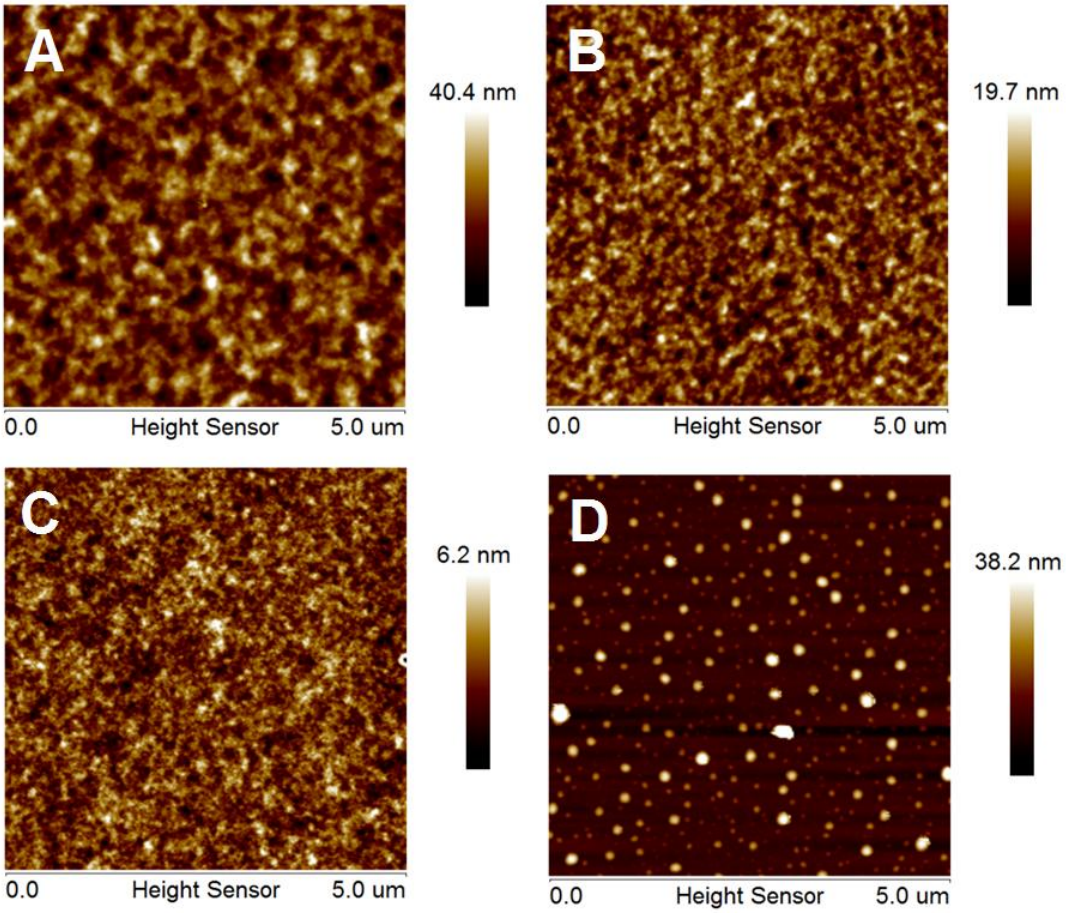

Figure 10. AFM height images of the (A) Neat P3HT:PCBM (B) H-POSS (C) OH-POSS and (D) PhSO3H-POSS modified P3HT:PCBM films. Image size is 5µmX5µm.

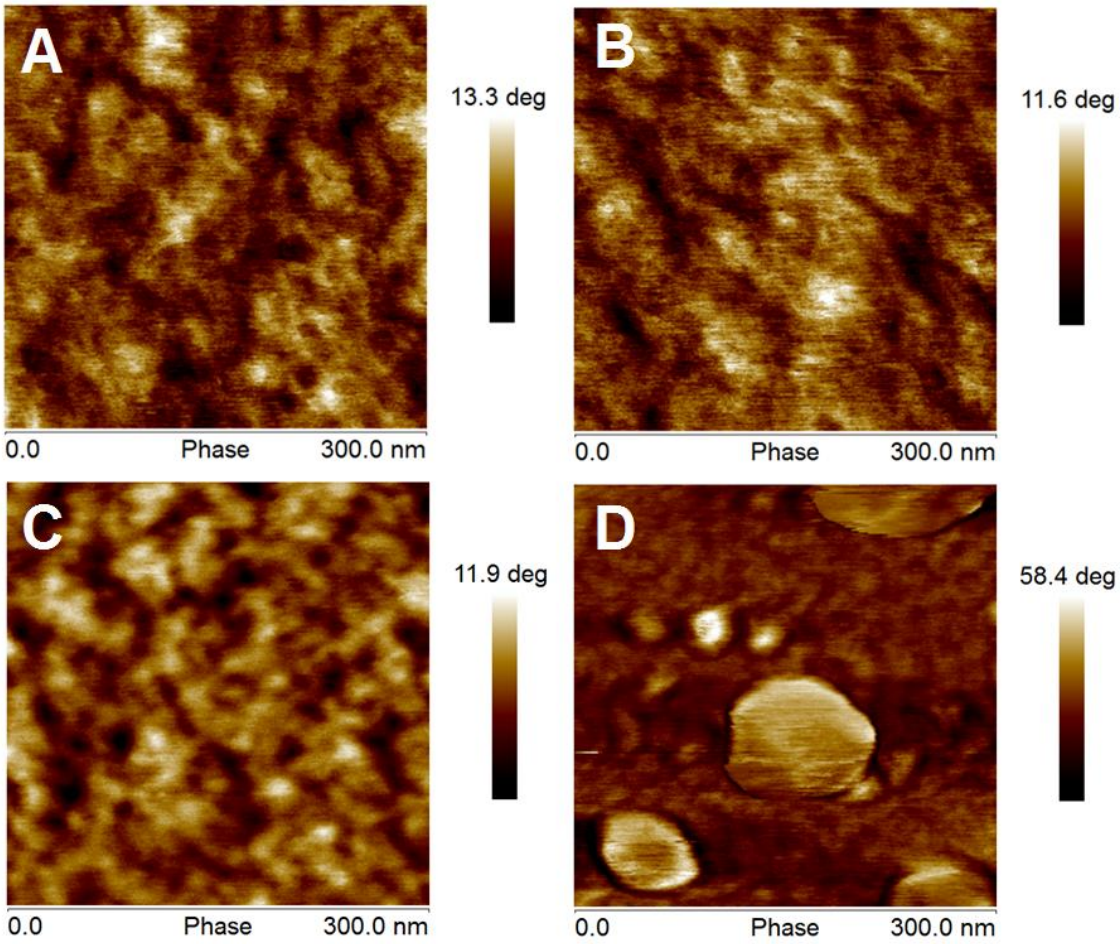

Figure 11. AFM phase images of the (A) Neat P3HT:PCBM (B) H-POSS (C) OH-POSS and (D) PhSO3H-POSS modified P3HT:PCBM films. Image size is 300 nm X 300 nm.

Table 1

Roughness of the Neat P3HT:PCBM and POSS-modified Films

	Neat	H-POSS	OH-POSS	$PhSO_3H$-POSS
RMS (nm) from 5μmX5μm	5.78	2.82	0.90	5.23
RMS (nm) from 300 nm X 300 nm	2.5	1.7	0.50	1.34

*All the RMS values are collected from the height images.

Morphology and phase separation evaluations were performed using AFM. Figure 10A displays the height image of the neat P3HT:PCBM film after 30 min thermal annealing. Fiber-like features (~150 nm diameter) are uniformly dispersed on the surface, attributed to P3HT crystallization and thermally induced phase separation. H-POSS has no organic substituents and thus allows analysis of the effects on morphology of addition of the silicon-oxygen cage alone. A finer phase separated morphology with closer domain packing is observed in the H-POSS containing sample in Figure 10B in comparison to that of the control, indicating the function of POSS as a dispersant. A similar phenomenon is observed in the OH-POSS modified films (Figure 10C). The domain spacing is further decreased and the domain size drops to ~100 nm diameter. This is attributed to hydrogen bonding of OH-POSS with PCBM, which alters the interactions between the P3HT and PCBM domains. A large number of uniformly dispersed aggregates (~200 nm diameter) are observed in the $PhSO_3H$-POSS modified film (Figure 10 D). A similar phenomenon was observed in our previous study of octa-phenyl POSS as an additive to P3HT/PCBM films, where it was found that POSS-PCBM clusters were formed in the active layer film, attributed to π-π interactions between POSS phenyl groups and fullerene substituents.[13] In this case, the $PhSO_3H$-POSS molecules contain both phenyl groups and hydroxyl groups functionality, allowing both π-π interactions and hydrogen bonding, resulting in the formation of a large number of aggregates.

The root mean square roughness values collected from the AFM height images are shown in Table 1. For the 5 micron images, the RMS values were observed to decrease for all of the POSS-containing samples, except for the $PhSO_3H$-POSS modified film which contains large aggregates, where an increase in roughness was observed. To

obtain a better understanding of the size of the phase separated domains, AFM analysis was performed on 300 nm X 300 nm sections of the films. In the $PhSO_3H$-POSS modified film the RMS value was collected from the 300 nm size height image excluding those large aggregates. The RMS values collected from the 300 nm size images displayed in Table 1 show reduced roughness for all of the POSS-containing samples in comparison to that of the standard. The reduction in the RMS values indicates the function of the silicon-oxygen cages as dispersants. Phase images at 300 nm scale are shown in Figure 11. Figure 11A displays the phase image of the neat P3HT:PCBM film. Small fiber like bright features (10-20 nm diameter) are observed embedded in the previously observed 150 nm domains. These smaller sized features found in the larger continuous domains are expected not only to help exciton diffusion but also to facilitate electron hopping in the bulk heterojunction system. Similar features were found in the H-POSS modified film (Figure 11B). A regular, phase separated morphology with uniformly dispersed network is exhibited in the OH-POSS modified film. Because of the presence of the large aggregates in the $PhSO_3H$-POSS modified film, it is difficult to discern the morphology of the underlying P3HT/PCBM blend.

UV-vis Spectroscopy Study

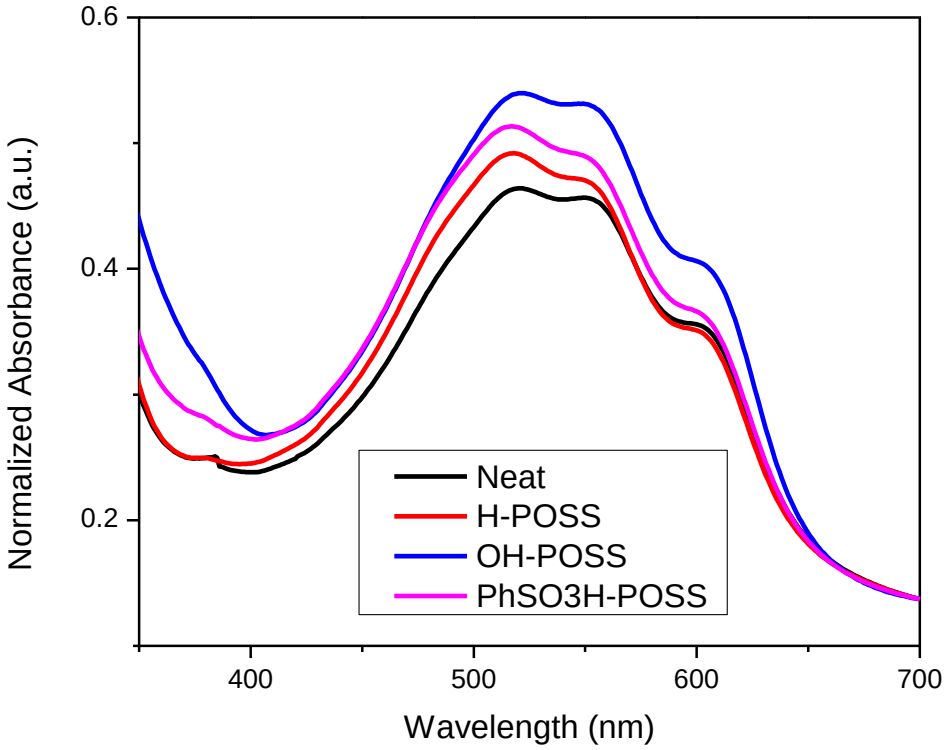

Figure 12. UV-vis spectra of the neat P3HT:PCBM films and POSS modified films.

In Figure 12 the UV-Vis spectra of thermally annealed neat and POSS-modified samples are shown. All POSS-modified samples display higher intensity peaks between 400 nm and 700 nm than those observed in the neat sample, which suggests a greater degree of crystallinity in the P3HT phase and enhanced phase separation in the heterojunction system.[14] The improved light absorption also suggests higher energy available during the light to electricity transition, affording the possibility of higher power conversion efficiency. The higher degree of crystallinity is attributed to the rigid POSS structures, which serve as nucleating agents for P3HT crystallization. This periodic seeding effect results in more ordered P3HT phase-separated domains, as shown in the

height images of the H-POSS and OH-POSS modified films in comparison to the standard. The OH-POSS modified film displayed the most regular morphology with most highly dispersed phases in both 5 μm and 300 nm AFM images, and also exhibits the highest absorption, suggesting the highest crystallinity and closest π-π stacking for these films. The light absorption decreases in the order of OH-POSS > $PhSO_3H$-POSS > H-POSS > neat film. It should be mentioned that even though a large number of aggregates are observed in the $PhSO_3H$-POSS sample, those aggregates are expected to act as light scattering vectors within the film, which serves to increase the light absorption. [13]

XRD Study

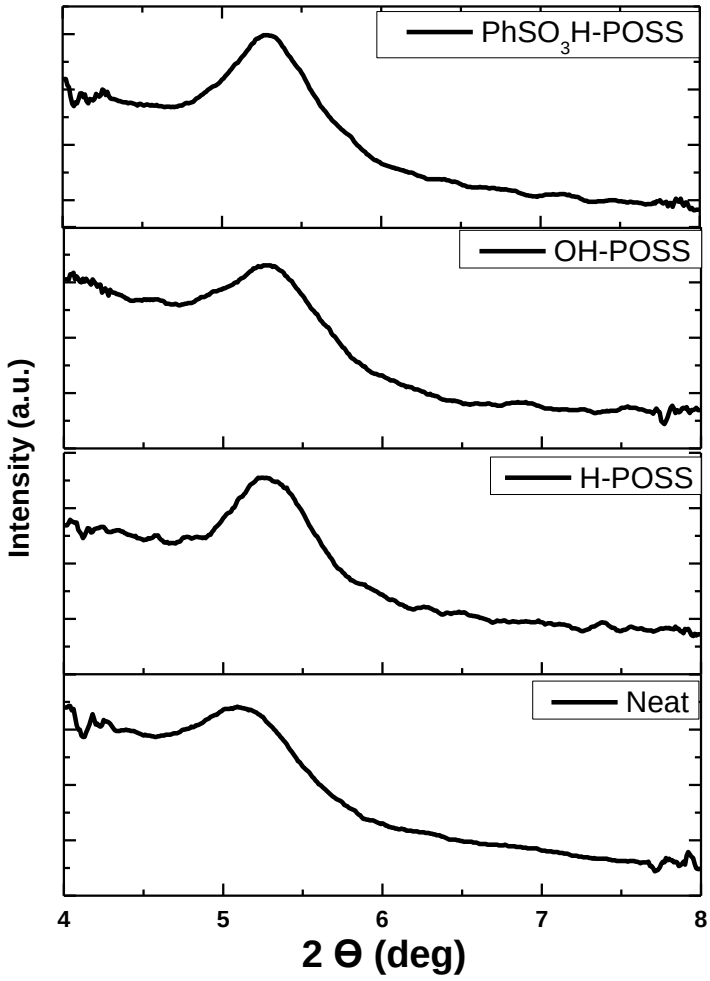

Figure 13. XRD curves of the neat P3HT:PCBM films and POSS modified films.

Table 2

d-spacing of the Neat P3HT:PCBM Films and POSS Modified Films

	Neat	H-POSS	OH-POSS	$PhSO_3H$-POSS
2θ (deg)	5.1	5.25	5.30	5.28
d-spacing (nm)	1.73	1.68	1.66	1.67

XRD was used to measure the spacing between P3HT crystals. The d-spacing is calculated using Bragg's equation:

$$\textit{Equation 1} \qquad d = \frac{n\lambda}{2sin\theta}$$

the results of which are shown in Table 2, with corresponding XRD curves shown in Figure 13. In all of the film samples (100) plane diffraction peaks are observed corresponding to an ordered lamellar structure with interlayer spacing. This interlayer spacing is generated by the alkyl side chains on the backbone of P3HT which separate the parallel stacks.[15] The peak maxima were used to determine the 2θ angle of all the solar cell samples. The peak position shifted to the right, suggesting decrement in the interlayer spacing and closer packing of the P3HT chains. This is attributed to POSS nucleation, which results in a greater degree of crystallization and tighter crystallite packing for the P3HT phase. For instance, when compared with the neat sample, which displays the peak maximum at a 2θ value of 5.1 deg, the sample modified with OH-POSS displays the peak maximum at 5.30 deg. Using Bragg's equation the spacing between P3HT stacking is found to decrease from 1.73 nm for the neat sample to 1.66 nm for the OH-POSS sample. It is suggested that closer spacing can facilitate hole mobility, allowing hopping between the PCHT chains with reduced loss of conductivity. [6,16] It should be noted that the d-spacing increases in the order of OH-POSS < $PhSO_3H$-POSS < H-POSS < neat film, parallel to the order of decrease in the measured UV-vis absorption, confirming the conclusion that POSS enhances crystallinity and crystallite packing of the P3HT phase.

Conclusions

In summary, the morphology and phase separation in the heterojunction P3HT:PCBM system can be altered by the addition of POSS molecules, and the degree to which morphology is altered depends on the POSS organic functional groups. The H-

POSS has been found to act as a dispersant and to lower the surface roughness. Fine phase separation was observed in the OH-POSS sample, and uniformly dispersed aggregates were formed on the addition of the $PhSO_3H$-POSS. Increased light absorption and decreased d-spacing between crystallites were observed for all POSS modified samples, suggesting a closer P3HT π-π stacking and higher crystallinity caused by the silicon-oxygen cages. The type of functional groups on the POSS molecule determined the extent to which crystalline packing changed. UV-vis and XRD studies indicated the π-π stacking degree decreased in the order of OH-POSS > $PhSO_3H$-POSS > H-POSS > neat P3HT:PCBM.

References

(1) National Academy Engineering Home Page. *http://www.engineeringchallenges.org/cms/challenges.aspx* (aceessed May 1, 2011).

(2) Zheng, Y.; Xue, J. *Polym. Rev.* **2010**, *50*, 420-453.

(3) Padinger, F.; Rittberger, R. S.; Sariciftci, N. S. *Adv. Funct. Mater.* **2003**, *13*, 85-88.

(4) Yang, X.; Loos, J.; Veenstra, S. C.; Verhees, W. J. H.; Wienk, M. M.; Kroon, J. M.; Michels, M. A. J.; Janssen, R. A. J. *Nano Lett.* **2005**, *5*, 579-583.

(5) Salamandra, L. Organic Photo-Voltaic Cells and Photo-Detectors based on Polymer Bulk-Heterojunctions. Ph.D. Thesis, University of Rome Tor Vergata, July 2009.

(6) Chang, Y.-M.; Wang, L. *J. Phys. Chem. C* **2008**, *112*, 17716-17720.

(7) Berson, S.; de, B. R.; Bailly, S.; Guillerez, S.; Jousselme, B. *Adv. Funct. Mater.* **2007**, *17*, 3363-3370.

(8) Kim, C.-H.; Cha, S.-H.; Kim, S. C.; Song, M.; Lee, J.; Shin, W. S.; Moon, S.-J.; Bahng, J. H.; Kotov, N. A.; Jin, S.-H. *ACS Nano* **2011**, *5*, 3319-3325.

(9) Misra, R.; Fu, B. X.; Plagge, A.; Morgan, S. E. *J. Polym. Sci., Part B: Polym. Phys.* **2009**, *47*, 1088-1102.

(10) Misra, R.; Fu, B. X.; Morgan, S. E. *J. Polym. Sci., Part B: Polym. Phys.* **2007**, *45*, 2441-2455.

(11) Wheeler, P. A.; Misra, R.; Cook, R. D.; Morgan, S. E. *J. Appl. Polym. Sci.* **2008**, *108*, 2503-2508.

(12) Zhang, Q.; He, H.; Xi, K.; Huang, X.; Yu, X.; Jia, X. *Macromolecules* **2011**, *44*, 550-557.

(13) Wu, Q.; Bhadra, S.; Bhattacharya, M.; Morgan, S. E. *Polym. Prepr. (Am. Chem. Soc., Div. Polym. Chem.)* **2011**, *52*, 307-308.

(14) Kim, Y.; Cook, S.; Tuladhar, S. M.; Choulis, S. A.; Nelson, J.; Durrant, J. R.; Bradley, D. D. C.; Giles, M.; McCulloch, I.; Ha, C.-S.; Ree, M. *Nat. Mater.* **2006**, *5*, 197-203.

(15) Li, G.; Shrotriya, V.; Yao, Y.; Huang, J.; Yang, Y. *J. Mater. Chem.* **2007**, *17*, 3126-3140.

(16) Nalwa, H. S. *Handbook of advanced electronic and photonic materials and devices*; Academic Press: San Diego, 2001; pp 1-25.

CHAPTER III

IDENTIFICATION OF POSS INTERACTIONS WITH P3HT AND PCBM AND RESULTANT PERFORMANCE IN ORGANIC PHOTOVOLTAIC DEVICES

Abstract

Nanoparticles have been shown in some cases to improve phase separation and morphology in bulk heterojunction organic photovoltaic cells. In this study, the effect of incorporation of POSS molecules of different structures in air processed P3HT and PCBM films and photovoltaic cells was evaluated. Morphology and composition of the nanoscale phase separated domains were determined via conductive atomic force microscopy in conjunction with nanomechanical mapping and Raman imaging. UV-vis and fluorescence spectroscopy analysis of the films was performed at different stages of the process and with different levels of solvent vapor and thermal annealing. It was found that POSS molecules of selected structures provided enhancement in morphology control in films, translating to improvements in fill factor and power conversion efficiency of laboratory-scale OPV cells. The findings indicate the potential for further improvements in solar cell performance with specifically tailored POSS/polymer phase separated systems.

Introduction

Polymer-based OPV devices have attracted considerable attention over the last decade due to their ease of fabrication, low-weight, flexibility, and potential reduction in cost.[1] The key disadvantage of OPV cells is their low power conversion efficiency compared with inorganic cells. Power conversion efficiency is determined by the process of photon absorption, exciton separation, and prevention of recombination of

electron/hole pairs prior to collection at the electrode, which is determined in turn by the composition and morphology of the phase-separated active layer in the OPV device. The active layer typically consists of a p-type conjugated polymer, which serves as the donor, and an n-type fullerene derivative, which serves as the acceptor. On absorption of light energy, an exciton is generated, which undergoes charge separation after diffusion to the donor/acceptor interface. The degree of phase separation, the size of the phase separated domains, and the organization of the domains determine the charge diffusion pathways and recombination processes. It has been reported that the highest conversion efficiency is achieved when the domain size is equal to the exciton diffusion length.[2,3] Phase separation is generally achieved through control of the crystallization and aggregation processes of the donor and acceptor components respectively. Processing techniques including thermal, [4,5,6] solvent,[7] and solvent vapor annealing[8] have been reported to enhance phase separation.[11,12]

A typical air processed photovoltaic cell consists of an anode layer, hole transporting layer, active layer, and cathode layer. For such a device with P3HTand PCBM, the power conversion efficiency is 2.2%, when processed in air. [9] Higher efficiencies can be achieved by inserting an interfacial electron transport layer and when processing under inert conditions; however, this is an obstacle for large scale industrial production.

Studies have been reported of incorporation of nanoparticles, including carbon nanotubes,[10] silver nanowires,[11] and gold nanoparticles,[12] in the active layer in an attempt to enhance morphology control. However, difficulty in obtaining adequate dispersion of the nanoparticles in the polymer blend limits their beneficial effects on the OPV system.

POSS nanostructured chemicals are hybrid organic-inorganic structures, monodisperse in size, consisting of a silicon oxide cage with a corona of organic substituents. By varying the organic groups, it has been shown that the migration and aggregation behavior of POSS molecules can be controlled in polymeric matrices to produce desired nanostructure development with associated performance improvements,[13-15] and POSS molecules can be tailored to serve as dispersing agents for organic and metallic nanoparticles.[16,17] It is also possible to effect changes in the morphology, crystallinity, and phase dispersion in polymeric blend systems on incorporation of specific POSS systems.[18,19] It has been reported that POSS molecules facilitate the electron injection and promote current density when attached to semiconducting polymers.[20,21] To the best of our knowledge, a study of POSS performance in OPV films has not yet been reported.

Polydimethylsiloxane (PDMS), a linear, long-chain macromolecule with siloxane backbone structure similar to that of the POSS cage, was evaluated by Graham et al. in a low band gap polymer blend. They reported that addition of PDMS increased J_{sc} by 50% and efficiency by 70% over the low-efficiency control.[22] PDMS is not as easily functionalized as POSS to provide compatibility with the active layer, and, as it is a flexible, long-chain molecule, it is not expected to provide structural rigidity to the blend. Small molecule additives with better miscibility than PDMS also have been used to improve the performance of organic photovoltaic cells by controlling the ternary morphology during the solvent evaporation process. [23-25] However, unlike the rigid POSS molecules, they are removed during solvent evaporation and cannot impart additional structural rigidity to the blend after drying.

Although incorporation of nanoparticles may result in enhanced OPV performance, development of a full understanding of the nanoscale morphology and mechanism of action in these complex blends is challenging. Raman imaging has been utilized to distinguish the donor and acceptor domains on the micron scale;[26,27] however, it does not have the resolution to determine nanoscale morphology. Atomic force microscopy (AFM) provides resolution of less than 10 nm in evaluating surface features of polymeric films. Traditional AFM tapping mode evaluation is widely used in morphology characterization; however, it is difficult to extract compositional information of phase separated systems based only on the height and phase images. Recently developed nanomechanical mapping AFM modules have become available in which it is possible to simultaneously extract topographical and materials properties information, including relative surface hardness, modulus and adhesion, at each point using a calibrated probe with known parameters.[28,29] Conductive AFM (C-AFM) techniques allow further determination of the composition of phase-separated OPV blends, where the hole and electron pathways can be identified at the nanoscale using current mapping analysis.[30]

In this study, POSS molecules were first introduced into an air processed P3HT and PCBM OPV system. Two types of POSS molecules with different functional groups were chosen to explore the effects of POSS interaction with blend components. Films were analyzed at different stages of the pre- and post-annealing processes of the active photovoltaic layer, and the relationship between morphology and composition was studied by nanomechanical mapping, conductive AFM, spectroscopic studies, and Raman

imaging. The effects of POSS- induced morphology and absorbance changes on OPV device performance were determined.

Experimentation

Materials

Unpatterned ITO glass slides with 8-12 Ω/sq resistance were purchased from Sigma Aldrich. Patterned ITO coated glass slides with coating thickness ~100 nm and surface resistivity of 8-12 Ω/sq were purchased from Luminescence Technology Corp., to use as the transparent anode. PEDOT-PSS, obtained from Ossilla as a 1.3 wt.% dispersion in water having resistivity in the range of 500-5000 Ω cm, was used as the hole transporter. P3HT, electronic grade, 98% regioregular, 99.995% pure on trace metals basis, average M_n ~ 45,000, was obtained from Sigma Aldrich. PCBM obtained from Sigma Aldrich with purity >99% and molecular weight of 911 g/mol was used as the acceptor. Octaphenyl POSS (Ph-POSS) and mercaptopropylisobutyl POSS (SH-POSS) with 99% purity were provided by Hybrid Plastics, Inc. o-Dichlorobenzene (DCB) from Acros was used as the solvent to form the actual photovoltaic donor/acceptor blend. For solvent vapor annealing (SVA), isopropanol (IPA) was used. All the materials were used as received.

Sample Preparation

Photoactive films for spectroscopic and microscopic analysis (without cathode layer). The photoactive P3HT:PCBM blend (ratio 1:0.6) was prepared in DCB (25 mg/ml) in an amber vial. The mixture was heated at 60°C for one hour to promote dissolution and then subjected to gradient cooling to room temperature in the same oil bath. It was then kept at room temperature for 24 hours. The POSS modified samples were prepared by

adding 1 wt % Ph-POSS or 1 wt % SH-POSS to the initial P3HT:PCBM mixture. POSS concentration was held at 1 wt% based on preliminary screening studies indicating optimum device performance at this level. ITO (~100 nm) coated glass plates were successively cleaned ultrasonically in deionized water, acetone and IPA for 10 minutes each. They were dried under N_2 and exposed to UV/ozone for 40 minutes and then immediately spin coated with a uniform layer of PEDOT:PSS. The PEDOT:PSS dispersion was spin-coated at a speed of 5000 rpm for 2 min. The PEDOT:PSS coated substrates were then dried for 15 min on a hot plate at 150°C in air, which was measured by AFM to be 40 ± 5 nm thickness. The P3HT:PCBM blend solution was spin coated on top of the PEDOT-PSS layer at 1250 rpm for 70 sec. The thickness of such active layers was found to be 100 ± 10 nm, as measured using AFM scratch testing. Solvent vapor annealing was performed for 20 min in a chamber saturated with IPA vapor. The samples were then thermally annealed at 150°C in argon for 30 min. The entire fabrication process was conducted in an air environment except for the thermal annealing (TA) step. The above samples prepared on unpatterned ITO glass were further studied by optical microscopy, AFM, Raman imaging, UV-vis spectroscopy, and fluorescence spectroscopy. Two annealing processes were conducted in this study, one involving only solvent vapor annealing (SVA) and the other using both SVA and thermal annealing (SVA-TA).

Solar cells for analysis of power conversion efficiency (with 100 nm coating of aluminum to form the cathode). The devices for performance measurement were prepared on patterned ITO glass. The glass cleaning process was the same as that used for the unpatterned ITO glass. After exposure to UV/ozone for 40 min, the ITO glass was spin coated with the PEDOT:PSS dispersion at a speed of 5000 rpm for 2 min. Then the slides

were heated on a hot plate at 150 °C in air for 15 min. The P3HT:PCBM (ratio 1:0.6) photoactive blend (the same composition as described previously for microscopic analysis) was spin coated on the baked PEDOT:PSS layer, then subjected to 20 min of solvent vapor annealing in an IPA saturated chamber, and then a 100 nm thick layer of Al (cathode) was evaporated on top of the active layer through a shadow mask using metal evaporation function by a Q150T Turbo-Pumped Sputter Coater. The deposition rate was controlled to 35 nm/min. to achieve reproducible coatings and device performance. The solar cells thus formed were then annealed at 150°C in argon for 30 min. Three identical devices were made and each device had six cells, with an active area of 0.042 cm^2.

Analytical Techniques

The optical microscopy images were obtained using a VHX digital microscope from Keyence. For this study, all images were collected at a magnification of 1000X .

Raman images were collected with a DXR Raman Microscope from ThermoScientific. A laser beam of 532 nm was focused with a 100 X /0.95 objective in the optical microscope. The laser power was 5 mW and the aperture was a 25 μm pinhole. The autofocus function was employed during the scanning to ensure that the laser was focused on the surface of the film. All images were baseline corrected. The resolution of the images is 540 nm.

AFM studies were conducted on a Dimension ICON scanning probe microscope from Bruker. The nanomechanical mapping images were acquired after calibration of the probe. A silicon probe from Bruker (RTESP) with nominal spring constant of 20-80 N/m was employed. The calibration process followed the absolute method and was checked through the relative method, which is suggested by the supplier. After calibration of the

AFM tip, the elastic modulus of the surface is estimated from the slope of the force-displacement curve when the tip is in contact with the surface, following Derajaguin-Mueller-Toporov (DMT) theory. This is known as the DMT modulus. [31-33] The evaluation of the DMT modulus was carried out using the Nanoscope Analysis 1.40 software, Bruker. All the processes were performed in the peakforce QNM air mode in Nanoscope 8 software. First a standard sapphire sample from Bruker was scanned and a force curve was obtained. The deflection sensitivity was calculated from the force curve using the software. Three different positions were chosen to ensure consistency of measurements. The average value was then used as the final deflection sensitivity. After obtaining the deflection sensitivity, the probe was withdrawn from the surface. Thermal tune function in the software was performed to obtain the resonance frequency of the probe, through which the spring constant was calculated. A standard titanium sample from Brucker and a neat P3HT:PCBM sample were then scanned with the previous parameters. The tip radius was calculated from the deformation image of the Ti sample and the height image of the neat P3HT:PCBM sample through the Nanoscope Analysis software. Finally a standard PEG-PS reference sample from Bruker was tested to make sure the expected elastic modulus value was obtained. A value of 0.3 was used as an estimate for Poisson's ratio and the scan rate was held at 1 Hz during the measurements. The height image and corresponding modulus image were obtained during one single scan. The root mean square (RMS) value from the height image was utilized to characterize the roughness of the surface. The average modulus value of the modulus image was used to show the stiffness of the surface. For those images with large (> 1

micron) phase separated features, the modulus values were calculated based on the flat areas which exclude the micron-scale features.

The conductive AFM analysis was performed using a probe from Bruker (SCM-PIC) with a thin platinum/iridium front side coating. The nominal spring constant of the probe was 0.18-0.42 N/m. Tip radius of the probe was 8 nm. During scanning, a bias of +2 V was applied between the ITO layer and the AFM probe. Both height images and corresponding current images were obtained during the measurements. Since the height images in C-AFM are similar to those obtained in nanomechanical mapping, only current images are shown. In calculations of average current, the micron-sized phase separated features were excluded in those images where they were present.

Fluorescence spectra were obtained using a TECAN Infinite M1000 microplate reader with premium Quad4 monochromators. UV-vis spectra were obtained using a Perkin-Elmer Lambda 6 UV/Vis spectrophotometer. The spectra normalization was carried out at 700 nm, where there is negligible absorption by the blend components. It was so chosen to identify the effect of each component (P3HT and PCBM) independently.

UV-vis and XRD analyses were preformed immediately after completion of the annealing procedure. AFM imaging was performed on the same day, while Raman and fluorescence studies were performed within two days of processing to standardize the time between processing and characterization. In each case, the three types of samples (neat, Ph-POSS, and SH-POSS) were produced and evaluated together.

Current-voltage (J-V) measurements were carried out using a Keithley 2400 source unit. Irradiation was provided by an AM1.5 solar simulator (Photo Emission Tech.

Inc.) with illumination of 1000 W/m^2 from a Xenon lamp coupled to a monochromator. The total incident light intensity was calibrated with a standard reference silicon solar cell.

Results and Discussion

It is well known that processing conditions, including thermal and solvent vapor annealing, affect nanoscale morphology, and conversion efficiency in P3HT/PCBM OPV systems.[34] For the current study a protocol was determined that reproducibly yielded the highest conversion efficiencies in air processed OPV cells produced in our laboratories (results reported previously).[35] It was found that cells produced with a 20 minute IPA solvent vapor annealing step followed by a 30 minute thermal annealing step at 150°C yielded the best performance. The choice of solvent for solvent vapor annealing was governed by two parameters – the solubility parameter and the boiling point. We previously demonstrated that during solvent vapor annealing of partly wet thin films, the use of a non-solvent resulted in a more favorable self-assembly of the polymer than that produced with a good solvent. [35]A good solvent increased the phase domain sizes beyond desirable limits. So a solvent (IPA[36]) with solubility parameter close to that of PCBM[37] but farther from that of P3HT [38] was chosen. This facilitated greater PCBM mobility, thereby initiating favorable PCBM aggregation even before the thermal annealing step. Also, the choice of a low boiling solvent ensured greater and faster penetration through the cross section of the film, resulting in efficient donor-acceptor assemblies. Similar concepts have been utilized earlier.[39] In an attempt to further optimize the morphology of the active layer, two types of POSS were introduced into the P3HT:PCBM system separately, whose structures are shown in Figure 14. The POSS structures were chosen for their potential interactions with the phase separated domains, where Ph-POSS is

expected to have greater affinity for the PCBM phase and SH-POSS for the P3HT phase. Spectroscopy and microscopy analyses were performed on multi-layer photoactive films without the cathode layer, while solar cell performance studies were performed on cells with an Al cathode layer coating.

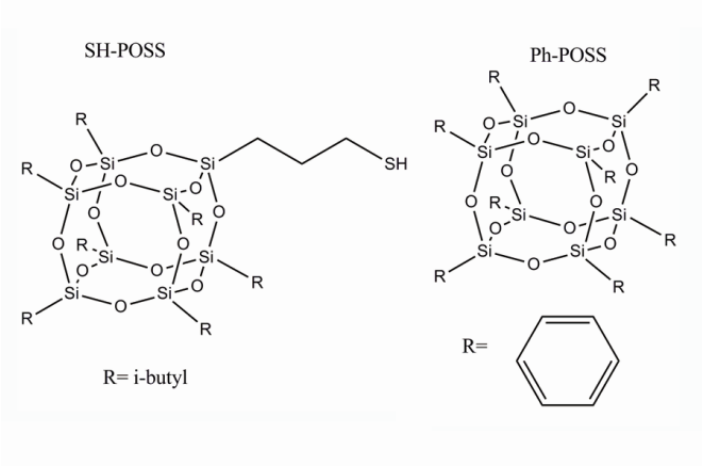

Figure 14. Structures of SH-POSS and Ph-POSS.

Optical Microscopy

Figure 15 shows the optical microscopy images of the OPV blends with and without POSS. The neat OPV film appears uniform and smooth (Figure 15A). In the Ph-POSS modified film (Figure 15B), oblong features 1-3 μm in diameter are observed which are attributed to POSS/polymer clusters. A smaller number of widely distributed oblong features are observed in the SH-POSS modified film (Figure 15C). The morphology variations in the samples arise from the different functional groups on the POSS molecules, as discussed in the following sections.

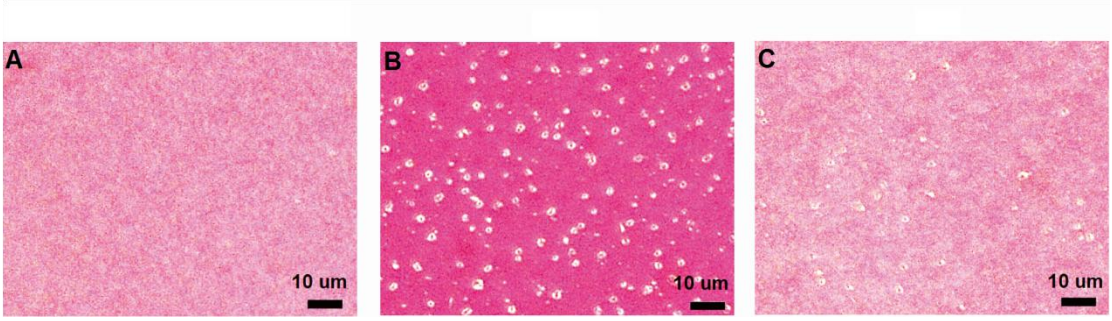

Figure 15. Optical microscopy images (1000X) of (A) the neat P3HT:PCBM film (B) the Ph-POSS modified film and (C) the SH-POSS modified film after SVA-TA. POSS is incorporated at 1 wt %.

Raman Imaging

Raman imaging analysis was performed to gain information about the compositions of the clusters observed in the Ph-POSS and SH-POSS modified films observed by optical microscopy. The Raman spectrum of the neat film was obtained to provide baseline information (Figure 16). The peak at 1447 cm^{-1} is attributed to the symmetric C=C stretch and the peak at 1325 cm^{-1} is attributed to the C-C intra-ring stretch of P3HT.[40,41] Because of the high intensity of the P3HT bands (related to the high crystallinity and close packing of the P3HT phase) the much lower intensity PCBM bands are difficult to discern. Thus, in accordance with previous literature reports,[2] the high intensity peak at 1447 cm^{-1} was used to determine the distribution of P3HT in the films.

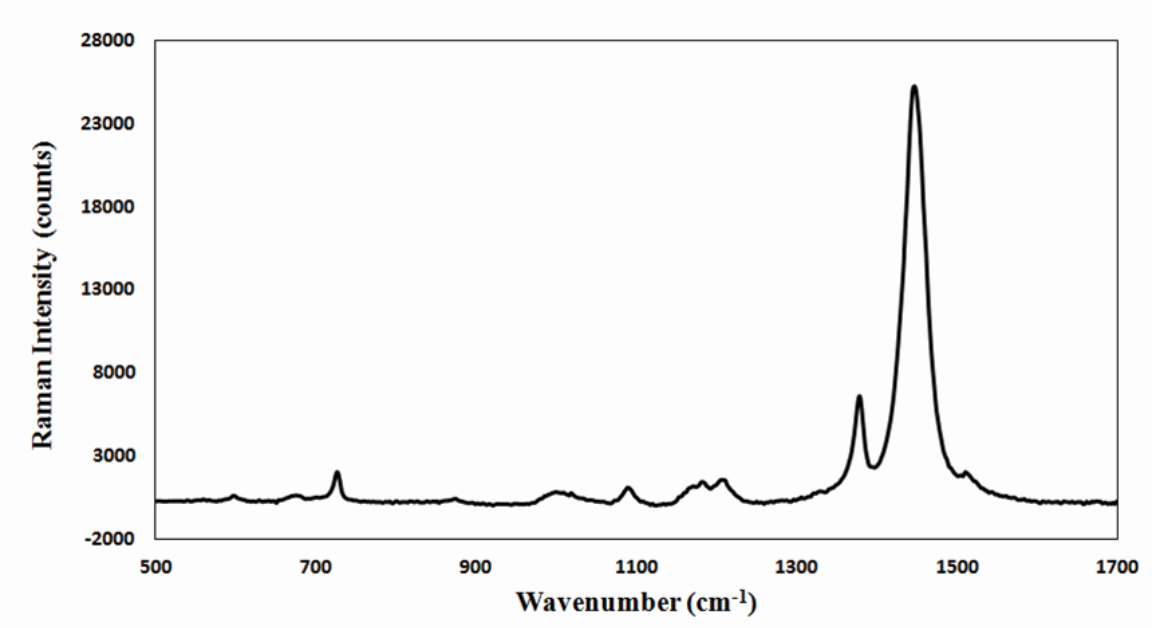

Figure 16. Raman spectrum of the neat P3HT:PCBM film after SVA-TA.

Raman imaging maps of the 1447 cm^{-1} peak are shown in Figure 17 for the neat P3HT:PCBM film (3a), the Ph-POSS modified film (3b), and the SH-POSS modified film (3c). The neat OPV film shows nearly uniform peak intensity, indicating uniform P3HT concentration distribution at the resolution of the Raman imaging (540 nm). Figures 17b and 17c show wide variations in peak intensity, with the red domains representing highest peak intensity and thus highest relative P3HT concentration and the blue domains representing lowest P3HT concentration. The Ph-POSS modified film (Figure 17b) shows micron-sized, oblong, low-intensity features that are attributed to domains with low P3HT concentration. The SH-POSS modified film (Figure 17c), in contrast, shows high intensity oblong features that are attributed to domains with high P3HT concentration.

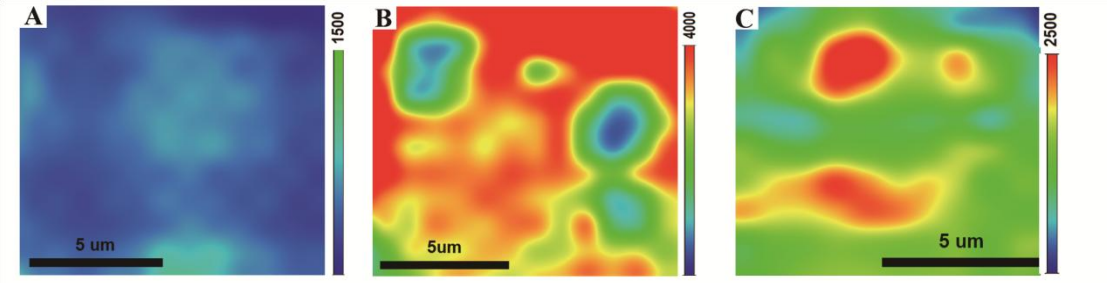

Figure 17. Raman images of the (A) neat P3HT:PCBM film (B) Ph-POSS modified film and (C) SH-POSS modified film after SVA-TA. The color bar indicates the peak intensity at 1447 cm^{-1}

AFM Analysis

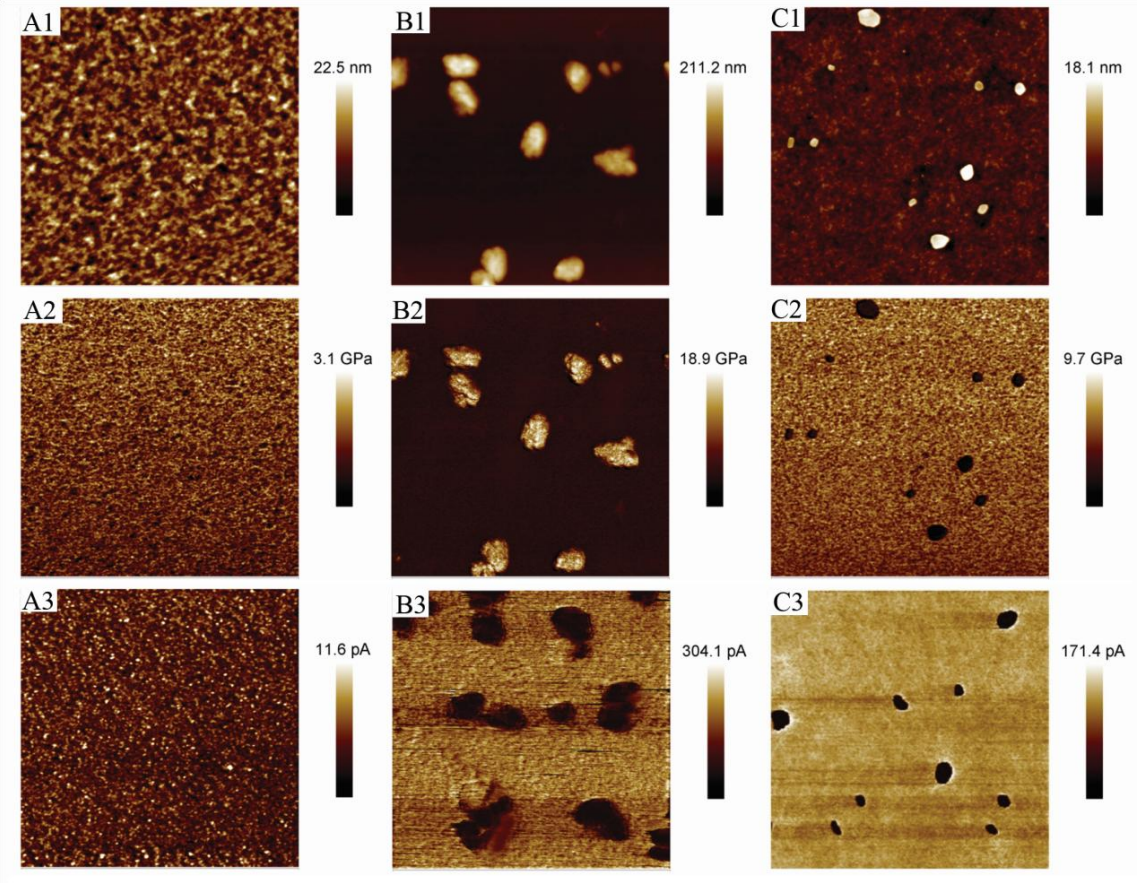

Figure 18. (A1) height image, (A2) the corresponding DMT modulus image and (A3) current image of P3HT:PCBM film after SVA-TA; (B1) height image (B2) the corresponding DMT modulus image and (B3) current image of the Ph-POSS modified film after SVA-TA; (C1) height image (C2) the corresponding DMT modulus image and (C3) current image of the SH-POSS modified film after SVA-TA. The lateral dimensions of all images are 5 μm X 5 μm.

Nanomechanical mapping allows simultaneous analysis of surface topography and mechanical properties of the film surface. Utilizing a calibrated probe with known physical parameters, it is possible to determine relative hardness and stiffness of nanoscale-separated features on the surface and thus infer the composition of the phase-separated morphological features. Figure 18 shows comparative height (1), DMT modulus (2), and current (3) images for the three P3HT:PCBM films, neat (A), Ph-POSS

modified (B), and SH-POSS modified (C). Physical parameters measured for the films are given in Table 3. The neat P3HT:PCBM film displays the nano-scaled phase-separated morphology typically observed for this system. The bright spots (approximately 20 nm in diameter) apparent in the AFM DMT modulus image correspond to the bright spots in the C-AFM image for the P3HT:PCBM film (A2 and A3, respectively), AFM analysis of neat PCBM and P3HT films showed that PCBM DMT modulus was one order of magnitude higher and PCBM conductivity two orders of magnitude higher than that measured for P3HT (Table 3). Under positive bias, electrons flow from the AFM tip to the surface, and the PCBM electron acceptor phase is expected to show higher conductivity and appear brighter in the C-AFM images.[42] The bright features in the neat PCBM:P3HT DMT modulus and C-AFM images are therefore attributed to the PCBM phase. The POSS-modified films show quite different morphologies, with large (1 μm in size), bright, oblong features apparent in the height images (B1 and C1). For the Ph-POSS modified film, corresponding bright features are observed in the DMT modulus image (B2), indicating that the raised features observed in the height images have higher DMT modulus than that of the surrounding material. For the SH-POSS modified film, however, the oblong features appear darker in the DMT modulus image (C2), indicating that they are lower in relative DMT modulus than the surrounding phase. As determined from cross sectional analysis of the topographic images, the raised features in the Ph-POSS modified film range from 100 – 150 nm in height while those in the SH-POSS are 10 – 20 nm in height.

AFM cross-sectional DMT modulus and conductivity analyses were performed in order to obtain more information about the composition of the raised features observed in

the height images of the POSS-containing blends (Figure 19). The baseline information of the individual components listed in Table 1 indicates that the polymeric P3HT shows relatively lower DMT modulus (2.2 GPa) than that of the carbon supported PCBM (11 GPa) and silicon-oxygen supported POSS (15 GPa). The average DMT modulus of the Ph-POSS modified film excluding the raised areas is 5.3 GPa, while the average DMT modulus of the raised features is greater than 10 GPa (Figure 19A1). This indicates that the raised areas consist of clusters of POSS and/or PCBM, while the surrounding phase is a blend with the softer P3HT. For the SH-POSS modified film, in contrast, the raised areas show lower DMT modulus than the surrounding matrix, indicating that the clusters are high in P3HT content. The surrounding matrix has higher modulus than that of the Ph-POSS film because it is enriched in PCBM. The C-AFM images of both POSS-modified films show that the clusters are lower in conductivity (darker) than the surrounding matrix (Figure 19B3, C3). This indicates that the clusters have a high content of the non-conducting POSS molecules. The cross-sectional analysis of the C-AFM images indicate that there is limited conductivity in the clusters found in the Ph-POSS modified film (Figure 19A2), but no measurable conductivity in the clusters in the SH-POSS modified film (Figure 19B2). The combined AFM mechanical and conductivity analyses indicate that the raised features observed in the Ph-POSS modified films consist of clusters of Ph-POSS with the highly conductive PCBM, while the features observed in the SH-POSS modified film consist of clusters of SH-POSS with P3HT. These findings are consistent with the conclusions from the Raman imaging analysis of the micron-sized phase-separated features.

The POSS aggregates observed in Figure 18B protrude from the surface more than 200 nm, and are thus of much greater height than the phase separated P3HT/PCBM blend component (maximum height approximately 20 nm). With such a great disparity in the height of the topographical features, it is not possible to simultaneously obtain high resolution of the two planes, POSS surface and active layer surface, in the same image. Thus, to evaluate the nanoscale morphology of the blends, AFM images were obtained of 500 nm flat areas in between the raised POSS clusters (Figure 20). Figures 20A1-C1 show the 5 um X 5um DMT modulus images, with Figure 20 A2-C2 providing corresponding DMT modulus and Figure 20 A3-C3 providing corresponding height images from the 500 nm X 500 nm flat areas. Phase separated polymer domains of 10-20 nm, close to the size of the exciton diffusion length,[2] are observed in the DMT modulus images. The bright features are attributed to the higher modulus PCBM phase and the darker regions to the softer P3HT phase. The Ph-POSS modified film exhibits the most regular morphology, with a clear network of fiber-like features surrounding evenly spaced softer features. The SH-POSS film shows a higher average DMT modulus, as was observed in the larger scale images in Figure 19, due to enrichment of PCBM in the matrix surrounding the SH-POSS clusters.[43]

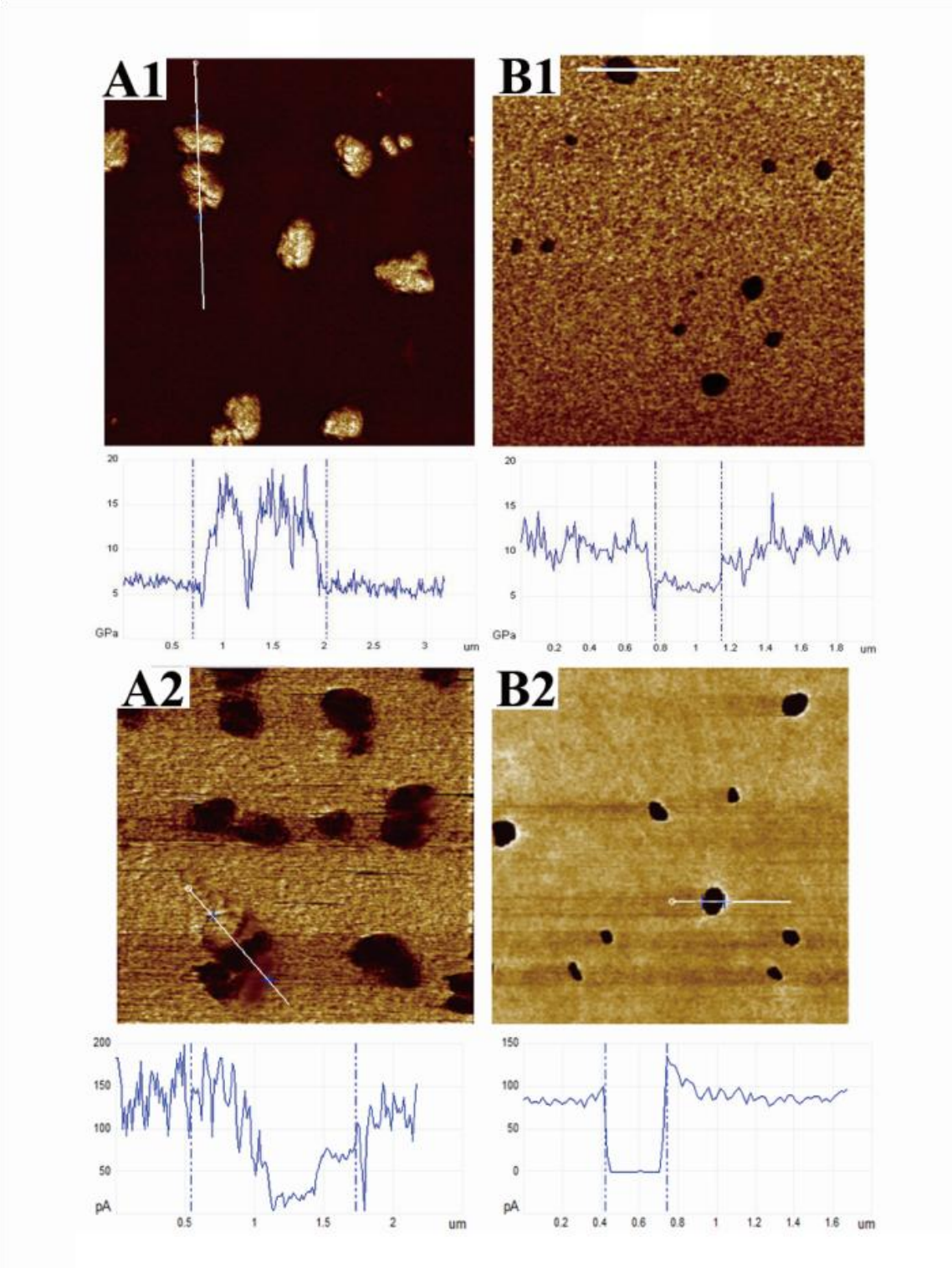

Figure 19. AFM cross section curves of POSS-modified films after SVA-TA. Ph-POSS (A1) DMT modulus image and (A2) current image; SH-POSS (B1) DMT modulus image and (B2) current image. White line indicates cross-section analyzed. The scale of all images is 5 μm X 5 μm.

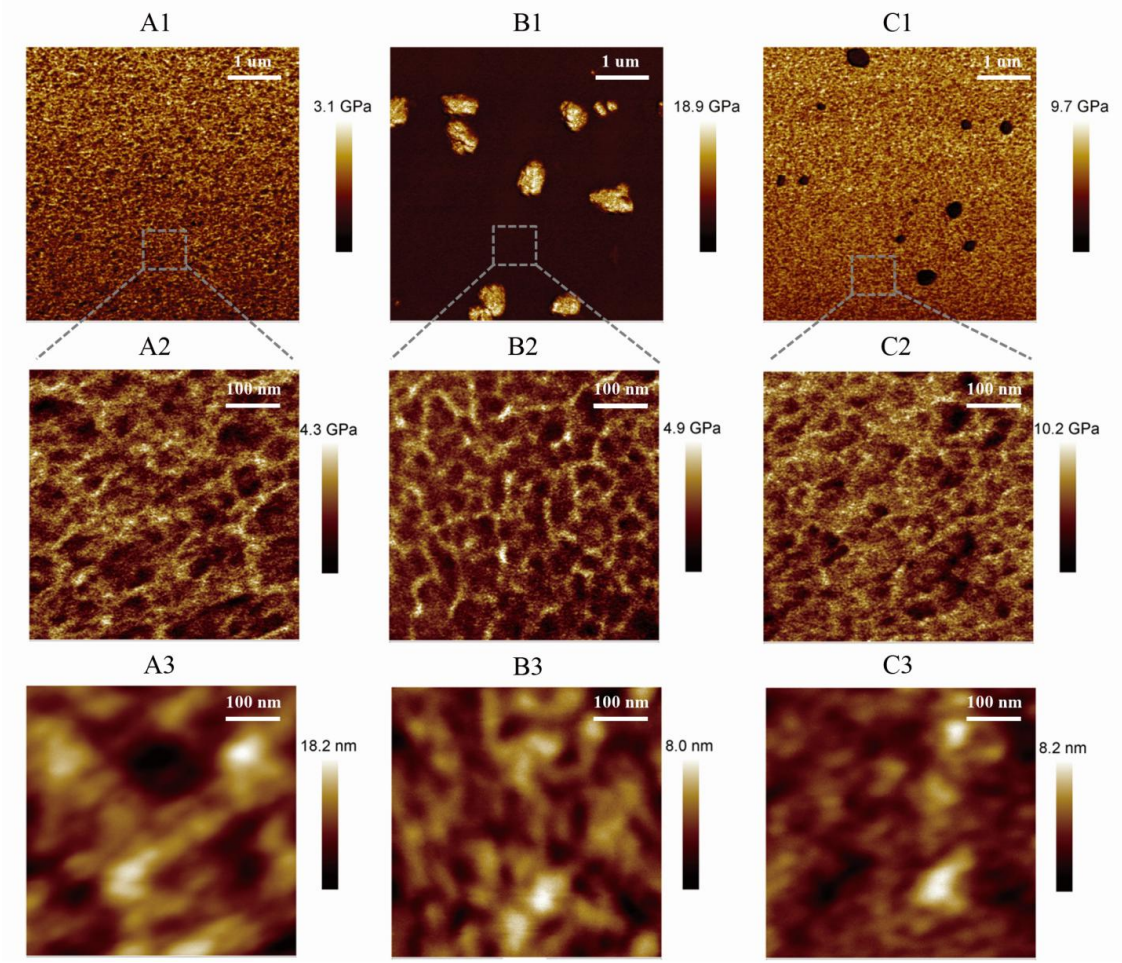

Figure 20. (A1) 5 x 5 μm DMT modulus image, (A2) 500 x 500 nm DMT modulus image, and (A3) the corresponding 500 x 500 nm height image of the P3HT:PCBM film after SVA-TA; (B1) 5 x 5 μm DMT modulus image, (B2) 500 x 500 nm DMT modulus, and (B3) the corresponding 500 x 500 nm height image of the Ph-POSS modified P3HT:PCBM film after SVA-TA (C1) 5 x 5 μm DMT modulus image, (C2) 500 x 500 nm DMT modulus image, and (C3) the corresponding 500 x 500 nm height image of the SH-POSS modified P3HT:PCBM film after SVA-TA.

In order to gain a better understanding of the interactions between the POSS molecules and the components of the photo-active polymers, a study of the effects of processing conditions was conducted. Films were prepared using only SVA and both SVA and TA. Nanomechanical mapping and C-AFM images of the POSS-modified films produced with SVA only are shown in Figure 21. The Ph-POSS modified film after SVA shows a morphology similar to that of the neat OPV film, with a smooth surface and no

aggregates. The corresponding SH-POSS modified film, on the other hand, displays aggregates with low DMT modulus and conductivity, similar to those observed after SVA-TA. Therefore, it is believed that the PCBM/Ph-POSS aggregates are formed during the TA step and the P3HT/SH-POSS aggregates are shaped during the SVA process. This is in accord with previous reports which suggest SVA aides P3HT self assembly and TA has a more dominant effect on the PCBM aggregation. [35,44] The differences in aggregate formation and composition are attributed to differences in the POSS molecule interactions with the P3HT/PCBM matrix. It is expected that the phenyl substituted Ph-POSS molecules preferentially interact with the PCBM phase through π-π interactions,[45] and Ph-POSS/PCBM aggregates are formed only after thermal annealing. The SH-POSS molecules are expected to form dimers through thiol coupling reactions when exposed to air,[46] and most likely serve as nucleation sites for P3HT crystallization during the SVA process, resulting in the observed SH-POSS/P3HT aggregates.

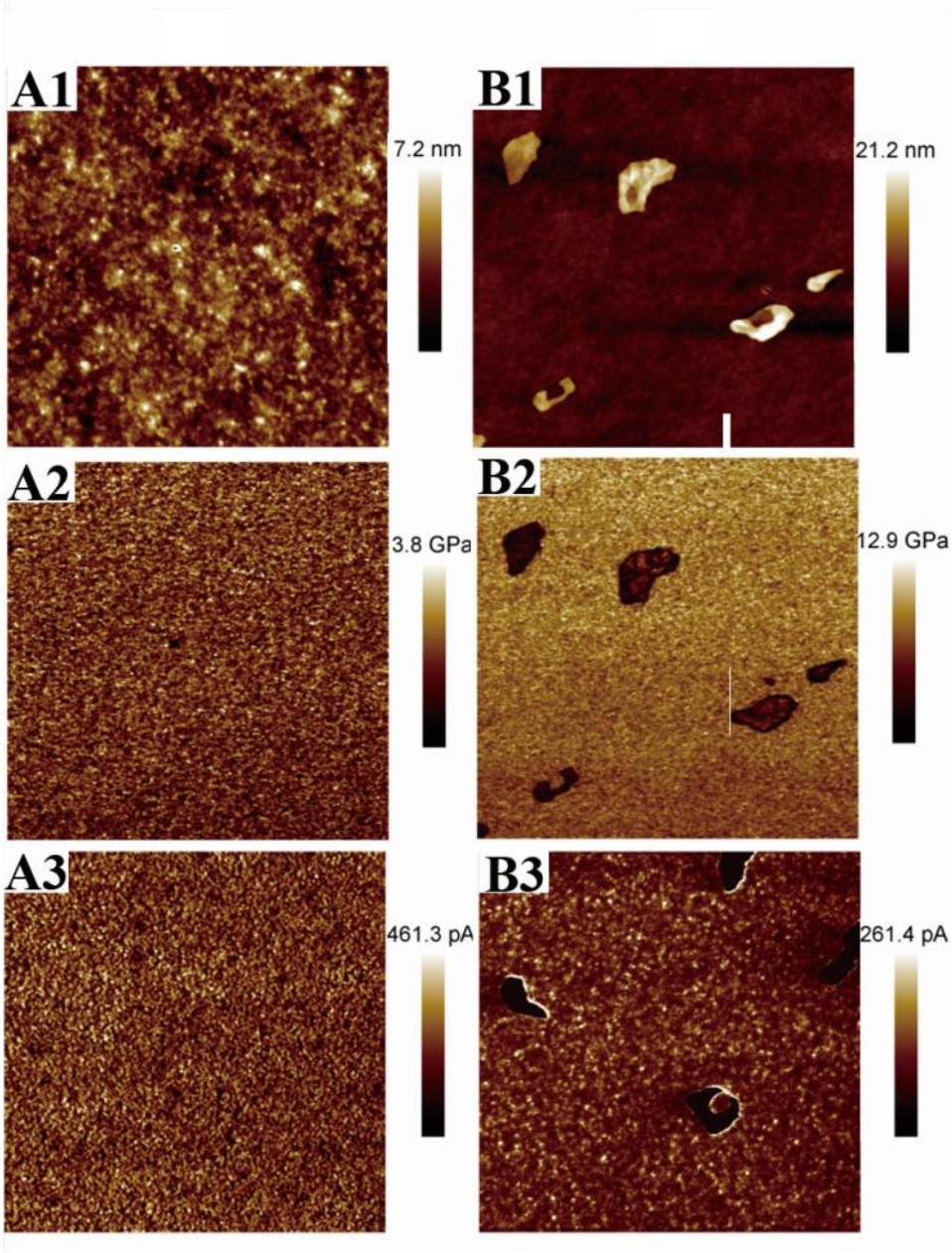

Figure 21. (A1) height image (A2) the corresponding DMT modulus image and (A3) current image of the Ph-POSS modified film after SVA; (B1) height image (B2) the corresponding DMT modulus image and (B3) current image of the SH-POSS modified film after SVA. The scale of all images is 5 μm X 5 μm.

The average roughness, DMT modulus and current values collected from AFM images of samples prepared with only SVA and both SVA-TA are listed in Table 3. RMS roughness is slightly increased after TA, while DMT modulus and conductivity are

slightly decreased. During the thermal annealing process, the amorphous P3HT content decreases as a highly crystalline P3HT phase with finer crystal structure emerges. Similar redistribution of the amorphous and distributed PCBM molecules into well-packed aggregates also ensues. The increases in P3HT crystallinity and PCBM aggregation accompany a small increase in the measured RMS roughness after the TA step. At the same time, a small decrease in the measured DMT modulus and conductivity is observed. We attribute these findings also to the redistribution and restructuring of the amorphous domains into finer crystalline domains, which results in an increase in interfacial material. Rather than being dominated by the peak values obtained from distributed PCBM molecules, the measured values of DMT modulus and conductivity represent an average of the overall contribution of the phase separated material and interfacial material. Thus, both increased phase separation and a greater distribution of finer structures are expected and desirable changes in morphology, and both correspond to improvements in solar cell performance.

Table 3

Nanomechanical and Conductive Properties of Individual Blend Components and OPV Films at Different Stages of Processing

Sample	RMS (nm)	DMT Modulus (GPa)	Average Current (pA)
Neat P3HT	N/A	2.2	25
Neat PCBM	N/A	11.0	1730
Neat Ph-POSS	N/A	15.0	N/A

Table 3 (continued).

Sample	RMS (nm)	DMT Modulus (GPa)	Average Current (pA)
Neat SH-POSS	N/A	15.0	N/A
P3HT:PCBM SVA	0.4	5.6	47
P3HT:PCBM SVA-TA	2.7	3.9	4
Ph-POSS SVA	0.5	6.5	248
Ph-POSS SVA-TA	1.1	5.3	112
SH-POSS SVA	0.5	11.4	75
SH-POSS SVA-TA	1.0	9.6	63

*the numbers are collected from AFM images excluding micron-size phase separated features

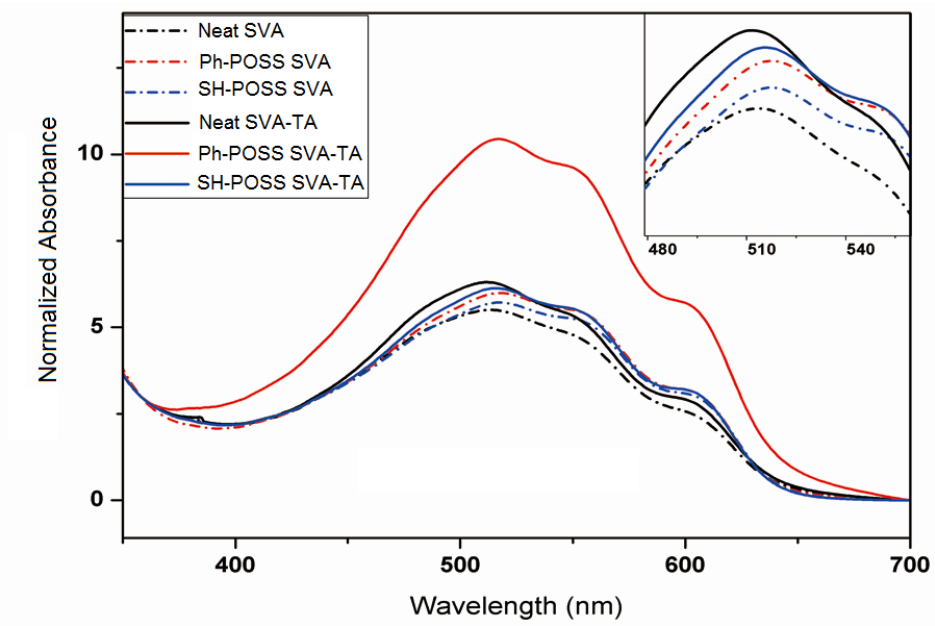

Figure 22. UV-Vis spectra of the neat P3HT:PCBM film, the SH-POSS modified film and the Ph-POSS modified film with SVA and SVA-TA.

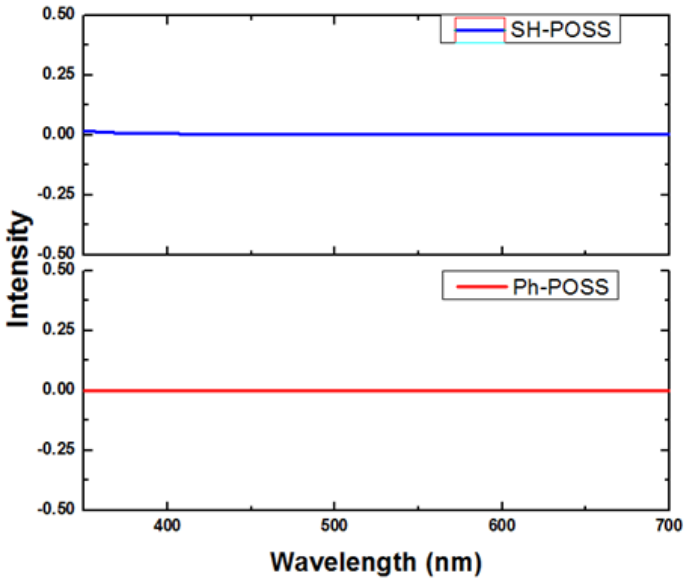

Figure 23. UV-vis absorption curves of Ph-POSS and SH-POSS in THF (0.001 g POSS in 1 mL THF).

The absorption spectra of the neat P3HT:PCBM and POSS-modified films, with SVA and SVA-TA, are shown in Figure 22. It was found that for all of the films, the absorbance increased after TA. Neat POSS samples showed no absorption in the 350 – 700 nm range (see Figure 23 and previous reports[47]), and thus the increments are attributed to increased crystallinity and packing of the P3HT phase.[48] Remarkably, absorption almost doubles for the Ph-POSS modified film after thermal annealing. This is attributed to the formation of PCBM-rich clusters during thermal annealing, which enhances phase separation and allows the P3HT to undergo further crystallization. At the same time, the PCBM/POSS clusters play an important role as scattering vectors, which reflect and scatter the light into the film. Such scattering results in increases in the path length traversed by light inside the active layer leading to enhancement of net absorption. We suggest that the PCBM/POSS clusters act in a similar way as the light entrapment features in inorganic solar cells, which can increase the performance greatly.[49]

Fluorescence Study

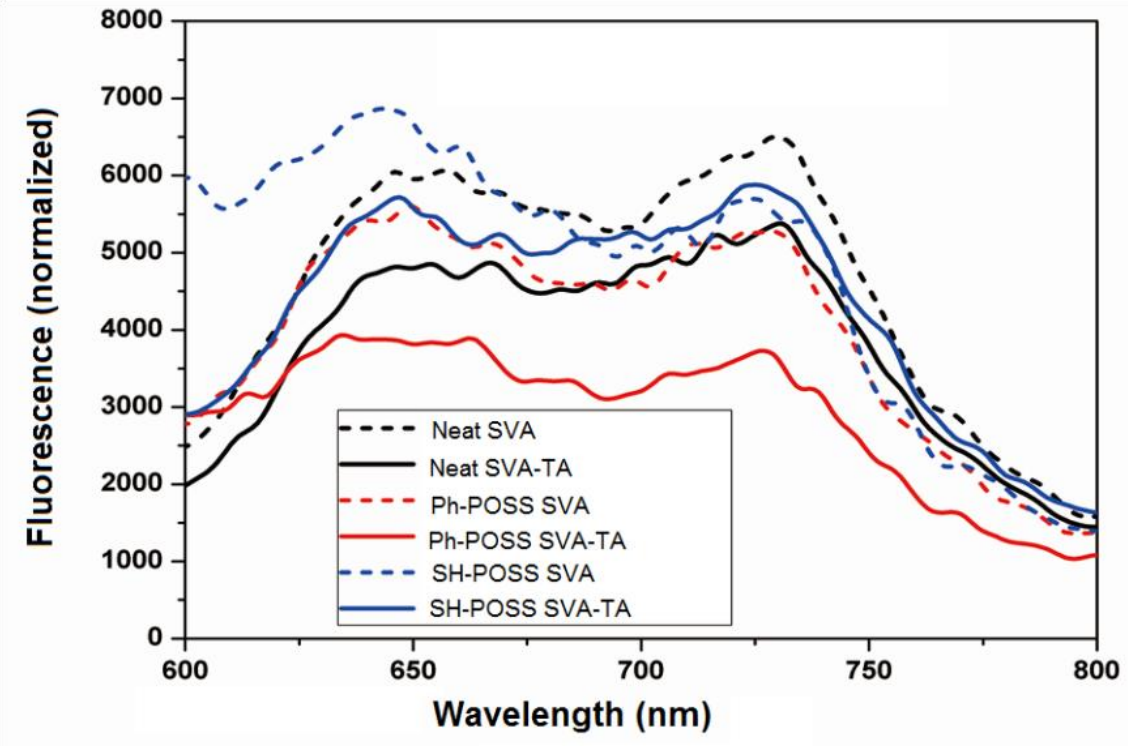

Figure 24. Fluorescence spectra of neat P3HT:PCBM, SH-POSS modified, and Ph-POSS modified films with SVA and SVA-TA.

Table 4

Integrated Area (x 10-4) of the Normalized Fluorescence Spectra from 600-800 nm

Neat SVA	Neat SVA-TA	Ph-POSS SVA	Ph-POSS SVA-TA	SH-POSS SVA	SH-POSS SVA-TA
93	78	81	59	96	87

P3HT fluorescence in the range of 600 and 800 nm is quenched when it is blended with PCBM, due to charge transfer between the molecules.[50,51] Thus the fluorescence quenching intensity is related to the efficiency of charge separation in the OPV film. Figure 24 shows the fluorescence spectra of the neat and POSS-modified films

with SVA and SVA-TA. For all of the films the fluorescence intensity is reduced after thermal annealing, implying more efficient phase separation. The Ph-POSS modified films show reduced fluorescence intensity in comparison to the neat film, while the SH-POSS modified films show increased fluorescence intensity. This indicates that Ph-POSS enhances phase separation and charge transfer, while the SH-POSS reduces efficiency of phase separation. The integrated areas of the spectra between 600 and 800 nm were calculated and tabulated in table 4. Assuming that lower values correspond to better quenching and phase separation, the efficiency trend is Ph-POSS SVA-TA> Neat SVA-TA>Ph-POSS SVA>SH-POSS SVA-TA> Neat SVA>SH-POSS SVA.

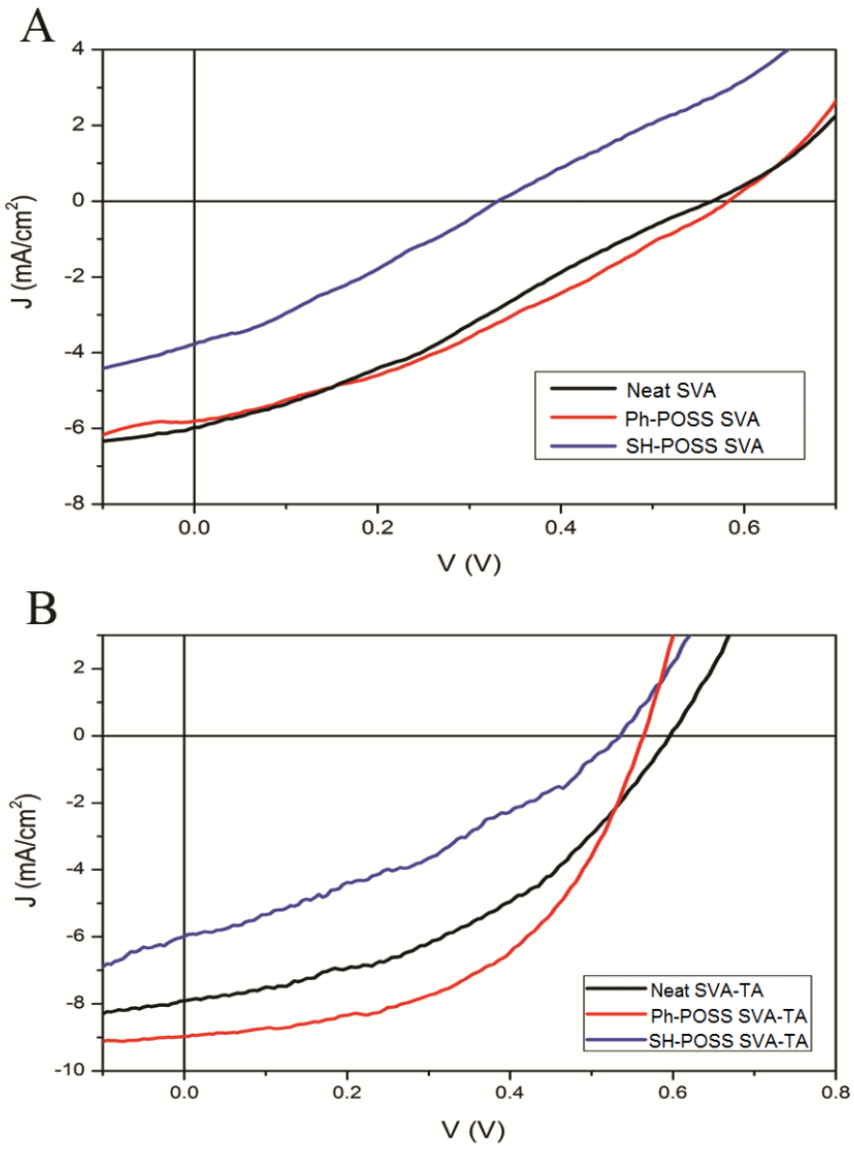

Figure 25. I-V curves of (a) devices with only solvent vapor annealing and (b) devices with both solvent vapor and thermal annealing.

Table 5

Performance of OPV Devices

	Jsc (mA/cm2)	Voc (V)	FF (%)	PCE (%)	Rsh (Ωcm2)	Rs (Ωcm2)
Neat SVA	5.8±0.2	0.57±0.01	32.1±4.0	1.07±0.08	144±49	70±18
Neat SVA-TA	7.9±0.2	0.6±0.01	43.9±1.9	2.08±0.10	261±16	29±5
Ph-POSS SVA	5.8±0.3	0.59±0.08	33.4±4.5	1.14±0.13	144±54	81±22
Ph-POSS SVA-TA	9.0±0.3	0.57±0.02	51.2±1.7	2.62±0.13	426±79	13±1
SH-POSS SVA	3.7±0.4	0.33±0.07	29.8±2.2	0.36±0.07	126±41	82±25
SH-POSS SVA-TA	6.0±0.1	0.54±0.04	35.2±2.1	1.14±0.11	144±20	38±8

SVA=isopropanol vapor annealing for 20 min, TA=thermal annealing at 150 ℃ for 30 min. Rsh and Rs are calculated to be equal to the inverse slope at Jsc and Voc, respectively. Values presented are averages with ± one standard deviation.

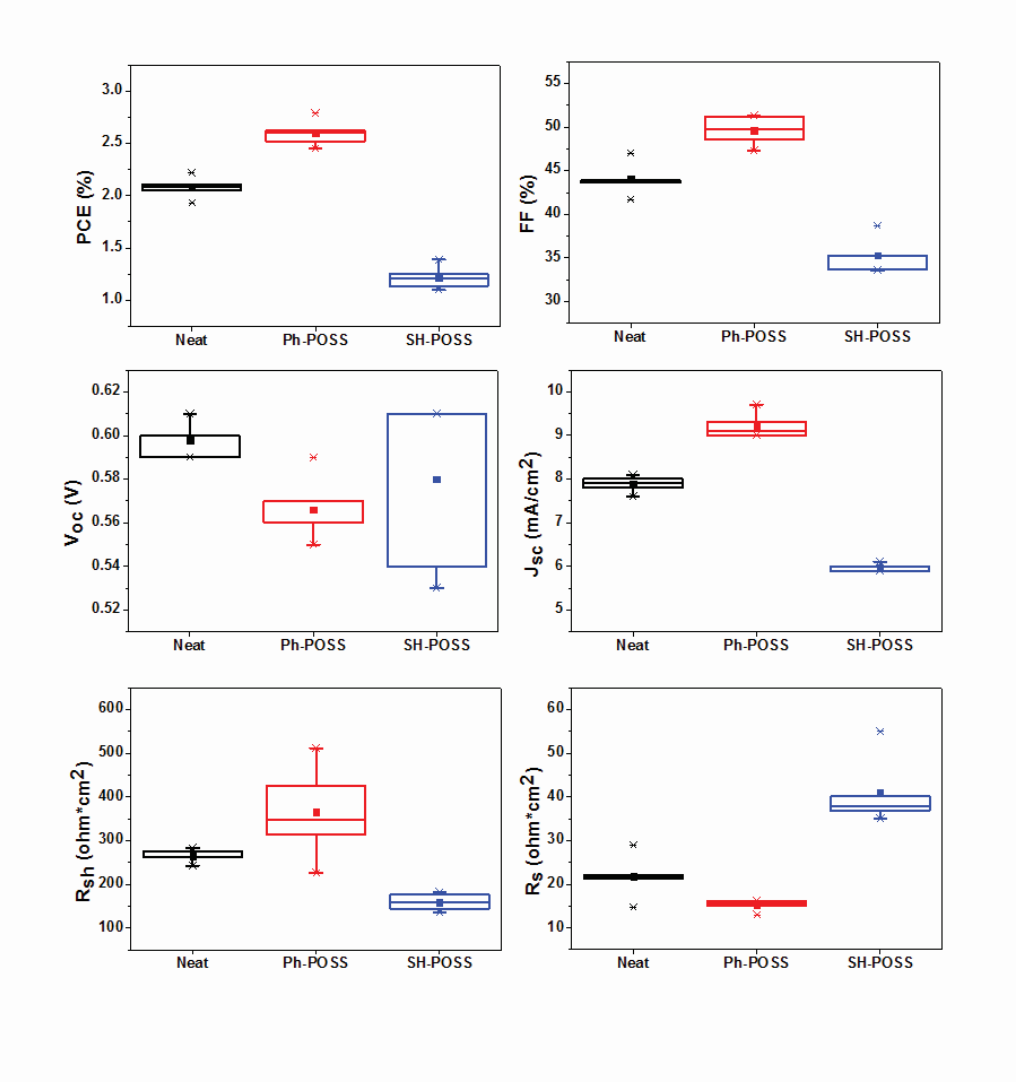

Figure 26. Box charts depicting the variability in device characteristics of cells that underwent both SVA and TA. (Bottom star is the 1st percentile, top star is the 99th percentile, top line of the box is the 75th percentile, medium line of the box is the median, bottom line of the box is the 25th percentile, and solid square is the mean).

Current-voltage curves of the OPV devices with and without POSS incorporation after (A) SVA and (B) SVA-TA are shown in Figure 25. Device performance characteristics (short circuit current density (J_{sc}), open circuit voltage (V_{oc}), fill factor (FF), power conversion efficiency (PCE), shunt resistance (R_{sh}) and series resistance (R_s) are given in Table 5 (box plot analysis of the data is provided in Figure 26). The devices with only SVA show poor performance, with low FF and PCE. Thermal annealing of

the neat OPV blend resulted in an increase of the FF from 32.1% to 42.9% and increase of the PCE from 1.07% to 2.08%, attributed to increased phase separation and crystallinity of the P3HT.[52] The addition of Ph-POSS increased the performance while SH-POSS decreased the performance of the cells. Similar trends were observed in J_{sc} as observed in UV-vis absorbance measurements, with the Ph-POSS demonstrating almost 50% improvement in comparison to the SH-POSS system. Absolute levels of improvement were not as high in the device as in the thin films, attributed to device inefficiencies. The thermally-annealed Ph-POSS-containing cells exhibited the highest R_{sh}, the lowest R_s and increases in the FF to 51.2% and PCE to 2.62%, in comparison to 43.0% and 2.02% respectively for the neat cells. The improvements are attributed to improved phase separation and scattering of the light by the PCBM/POSS clusters into the film, which increases the light absorbance efficiency in the device. Such scattering within the active layer is thought to increase the photon absorption by lengthening the optical path traversed,[49,53] resulting in increased exciton generation. The P3HT/POSS clusters in the SH-POSS modified films, on the other hand, disrupt the phase separated morphology and reduce charge transfer efficiency. It is interesting to note that the measured device efficiency trend follows the same order as that of fluorescence quenching of the films, which indicates that the simpler fluorescence spectroscopy analysis could be used to predict solar cell performance.

Power conversion efficiencies achieved with the incorporation of one weight percent Ph-POSS are reproducible and statistically significant, and are comparable to or greater than those reported with other types of nanoparticles,[10-12,54] where simple incorporation without further treatment often results in decrease in efficiency. The

improvements are also similar to those reported with the addition of PDMS.[22] Addition of high percentages (5-13%) of alkyl thiols yielded greater enhancement of PCE (up to 130% improvement in comparison to 25% improvement for Ph-POSS). These films, however, were twice as thick as our active layers. [24] The promising results reported herein with low weight percentages of POSS materials indicate their potential for further enhancement of device performance, alone or in combination with other additives. The ability to tailor the POSS organic corona with a wide range of specific compositions presents the possibility for compatibility with different photoactive polymeric systems, dispersion of synergistic nanomaterials, and/or introduction of other functionality. Additionally, we suggest that the enhancement in nanomechanical properties obtained on incorporation of the hybrid POSS nanomaterials may provide an avenue for strengthening and improving the long-term performance of the OPV cells.

Specific Considerations

The film thickness can influence the polymeric characteristics dramatically, particularly in the thin film regime. Glass transition temperature (Tg) is an important characteristic indicating the long range segmental movement of polymer chains and its measurement may be used to probe the difference in properties for polymeric thin films and the bulk. The Tg of a free standing polymeric film decreases with decreasing film thickness. In a polystyrene (PS) system, when the thickness is less than a critical value of 70 nm, the PS thin film shows Tg lower than the bulk system, and Tg decreases linearly with decreasing film thickness below the critical thickness. [55]When the Tg of the bulk polymer increases, the critical thickness also increases. In a poly(methyl methacrylate) (PMMA) system with Tg higher than that of PS, the Tg of the PMMA decreases at

thicknesses below 100 nm. [56] The Tg of the P3HT is reported to be 12 ^{0}C;[57] thus, the critical thickness is believed to be lower than that of PS. While the photoactive layer thickness is above 100 nm, the films are considered to show equal properties as the bulk system in this case.

In this study, SH-POSS and Ph-POSS molecules were added at one weight % to the active layer. As the molecular weight of SH-POSS (MW=891 g/mol) is slightly lower than that of Ph-POSS (MW=1033 g/mol), both the molar (calculate: SH-POSS = mol%, Ph-POSS = mol%) and volume ratios of SH-POSS are slightly higher than that of Ph-POSS (estimate size of butyl vs phenyl ring substituents to give relative volume difference, should be small). If the POSS molecules were individually dispersed, it would be expected that SH-POSS would provide more surface area than that of the Ph-POSS in the same weight percentage, which might influence the nanoscale morphology of the photoactive films in a more efficient way. However, both Ph-POSS and SH-POSS were observed to form micron-sized aggregates with PCBM and P3HT respectively. Even though the Ph-POSS was present in slightly lower molar and volume percentages than the SH-POSS, it provided dramatically improved efficiency through its interaction with the PCBM phase, which resulted in elevated light absorption, promoted P3HT crystallinity, and better dispersed phase separated domains. The SH-POSS, however, presenting more interactions with P3HT resulted in reduced charge generation and device performance. It should be noted that only 1 wt% Ph-POSS was utilized in the P3HT:PCBM system. It would be expected that higher concentrations of POSS would decrease the device performance due to the non-conductivity of the POSS molecules.

Conclusions

Air processed P3HT:PCBM based photovoltaic films were prepared under both isopropanol solvent vapor annealing alone and SVA combined with thermal annealing. Ph-POSS and SH-POSS were introduced into this system in an attempt to enhance control of the morphology and phase separation. Micron sized aggregates (1-3 μm) were observed in the POSS modified films after SVA-TA. Raman imaging indicated that the aggregates in the SH-POSS modified films were rich in P3HT, while those observed in the Ph-POSS modified films had low concentrations of P3HT. Conductive-AFM and nanomechanical mapping demonstrated that the aggregates in the Ph-POSS modified film exhibited a small amount of conductivity and were of higher relative hardness, providing further evidence of their low P3HT and high Ph-POSS/PCBM content. The aggregates observed in the SH-POSS modified films, on the other hand, demonstrated low relative hardness and no conductivity, providing further evidence of their higher concentration of P3HT. AFM analysis of the films at different steps in the process indicated that while the SH-POSS/P3HT aggregates formed during solvent vapor annealing, the Ph-POSS/PCBM aggregates did not form until the thermal annealing step. This phenomenon was attributed to the different interactions of the POSS molecules of different structures with the P3HT and PCBM phases; Ph-POSS is expected to interact with the PCBM phase through π-π interactions, while the SH-POSS displays greater interaction with the P3HT phase. UV-vis spectroscopy analysis demonstrated that Ph-POSS incorporation resulted in a doubling of the absorbance in comparison to the neat P3HT:PCBM film, while SH-POSS incorporation reduced absorption. The enhanced light absorption was attributed to improved phase separation and nanoscale morphology in the Ph-POSS containing films

and to the Ph-POSS/PCBM aggregates acting as scattering sites to reflect and scatter light within the film. Fluorescence spectroscopy analysis produced a trend of fluorescence quenching in the order of Ph-POSS SVA-TA> Neat SVA-TA>Ph-POSS SVA>SH-POSS SVA-TA> Neat SVA>SH-POSS SVA. Laboratory-scale photovoltaic cells were assembled and their performance analyzed. The Ph-POSS modified P3HT:PCBM cell exhibited improved performance in comparison to the neat P3HT:PCBM cell, with the short current density increasing from 7.9 to 9.0 mA/cm^2, the fill factor increasing from 43.9 to 51.2% and the power conversion efficiency improving from 2.08 to 2.62%. These improvements were attributed to enhanced phase separation and improved scattering within the film due to Ph-POSS/PCBM aggregates. The SH-POSS modified film, on the other hand, showed poorer performance than the standard, attributed to greater irregularity in the nanoscale morphology. The trends observed in conductive AFM and fluorescence quenching of the films were the same as those observed in the OPV cells. These findings indicate the promise for improving OPV cell efficiency through incorporation of properly functionalized POSS molecules in phase separated bulk heterojunction OPV systems.

References

(1) Xue, J. *Polym. Rev.* **2010**, *50*, 411-419.

(2) Zheng, Y.; Xue, J. *Polym. Rev.* **2010**, *50*, 420-453.

(3) Skotheim, T. A.; Reynolds, J. R., Eds. *Handbook of Conducting Polymers, Third Edition. Conjugated Polymers Processing and Applications*; CRC Press LLC: Boca Raton, 2007.

(4) Padinger, F.; Rittberger, R. S.; Sariciftci, N. S. *Adv. Funct. Mater.* **2003**, *13*, 85-88.

(5) Yang, X.; Loos, J.; Veenstra, S. C.; Verhees, W. J. H.; Wienk, M. M.; Kroon, J. M.; Michels, M. A. J.; Janssen, R. A. J. *Nano Lett.* **2005**, *5*, 579-583.

(6) Salamandra, L., Organic Photo-voltaic Cells and Photo-detectors Based on Polymer Bulk-heterojunctions, Ph.D. Thesis, University of Rome Tor Vergata, Rome, 2009.

(7) Li, G.; Shrotriya, V.; Huang, J.; Yao, Y.; Moriarty, T.; Emery, K.; Yang, Y. *Nat. Mater.* **2005**, *4*, 864-868.

(8) Hegde, R.; Henry, N.; Whittle, B.; Zang, H.; Hu, B.; Chen, J.; Xiao, K.; Dadmun, M. *Sol. Energy Mater. Sol. Cells* **2012**, *107*, 112-124.

(9) Rider, D. A.; Tucker, R. T.; Worfolk, B. J.; Krause, K. M.; Lalany, A.; Brett, M. J.; Buriak, J. M.; Harris, K. D. *Nanotechnology* **2011**, *22*, 085706/085701-085706/085709.

(10) Berson, S.; de, B. R.; Bailly, S.; Guillerez, S.; Jousselme, B. *Adv. Funct. Mater.* **2007**, *17*, 3363-3370.

(11) Kim, C.-H.; Cha, S.-H.; Kim, S. C.; Song, M.; Lee, J.; Shin, W. S.; Moon, S.-J.; Bahng, J. H.; Kotov, N. A.; Jin, S.-H. *ACS Nano* **2011**, *5*, 3319-3325.

(12) Topp, K.; Borchert, H.; Johnen, F.; Tunc, A. V.; Knipper, M.; von, H. E.; Parisi, J.; Al-Shamery, K. *J. Phys. Chem. A* **2010**, *114*, 3981-3989.

(13) Misra, R.; Fu, B. X.; Plagge, A.; Morgan, S. E. *J. Polym. Sci., Part B: Polym. Phys.* **2009**, *47*, 1088-1102.

(14) Misra, R.; Fu, B. X.; Morgan, S. E. *J. Polym. Sci., Part B: Polym. Phys.* **2007**, *45*, 2441-2455.

(15) Abad, M. J.; Barral, L.; Fasce, D. P.; Williams, R. J. J. *Macromolecules* **2003**, *36*, 3128-3135.

(16) Wheeler, P. A.; Misra, R.; Cook, R. D.; Morgan, S. E. *J. Appl. Polym. Sci.* **2008**, *108*, 2503-2508.

(17) Lligadas, G.; Ronda, J. C.; Galia, M.; Cadiz, V. *Biomacromolecules* **2006**, *7*, 3521-3526.

(18) Misra, R.; Fu, B. X.; Plagge, A.; Morgan, S. E. *J. Polym. Sci., Part B: Polym. Phys.* **2009**, *47*, 1088-1102.

(19) Misra, R.; Alidedeoglu, A. H.; Jarrett, W. L.; Morgan, S. E. *Polymer* **2009**, *50*, 2906-2918.

(20) Xiao, S.; Nguyen, M.; Gong, X.; Cao, Y.; Wu, H.; Moses, D.; Heeger, A. J. *Adv. Funct. Mater.* **2003**, *13*, 25-29.

(21) Lee, R.-H.; Lai, H.-H. *Eur. Polym. J.* **2007**, *43*, 715-724.

(22) Graham, K. R.; Mei, J.; Stalder, R.; Shim, J. W.; Cheun, H.; Steffy, F.; So, F.; Kippelen, B.; Reynolds, J. R. *ACS Appl. Mater. Interfaces* **2011**, *3*, 1210-1215.

(23) Dang, M. T.; Hirsch, L.; Wantz, G.; Wuest, J. D. *Chem. Rev.* **2013,** *113*, 3734-3765.

(24) Ouyang, J.; Xia, Y. *Sol. Energy Mater. Sol. Cells* **2009**, *93*, 1592-1597.

(25) Pivrikas, A.; Stadler, P.; Neugebauer, H.; Sariciftci, N. S. *Org. Electron.* **2008**, *9*, 775-782.

(26) Riisness, I.; Carach, C.; Gordon, M. J. *Appl. Phys. Lett.* **2012**, *100*, 073308/073301-073308/073304.

(27) Huang, Y.-C.; Liao, Y.-C.; Li, S.-S.; Wu, M.-C.; Chen, C.-W.; Su, W.-F. *Sol. Energy Mater. Sol. Cells* **2009**, *93*, 888-892.

(28) Lofaj, F.; Ferdinandy, M.; Cempura, G.; Dusza, J. *J. Eur. Ceram. Soc.* **2012**, *32*, 2043-2051.

(29) Adamcik, J.; Lara, C.; Usov, I.; Jeong, J. S.; Ruggeri, F. S.; Dietler, G.; Lashuel, H. A.; Hamley, I. W.; Mezzenga, R. *Nanoscale* **2012**, *4*, 4426-4429.

(30) Dante, M.; Peet, J.; Nguyen, T.-Q. *J. Phys. Chem. C* **2008**, *112*, 7241-7249.

(31) Derjaguin, B.; Muller, V.; Toporov, Y. P. *J. Colloid Interface Sci.***1975**, *53*, 314-326.

(32) Butt, H.-J.; Cappella, B.; Kappl, M. *Surf. Sci. Rep.* **2005**, *59*, 1-152.

(33) Watanabe, J.; Lepoutre, P. *J. Appl. Polym. Sci.* **1982**, *27*, 4207-4219.

(34) Zhao, Y.; Xie, Z.; Qu, Y.; Geng, Y.; Wang, L. *Appl. Phys. Lett.* **2007**, *90*, 043504/043501-043504/043503.

(35) Bhattacharya, M.; Wu, Q.; Morgan, S. E. *Polym. Prepr.* **2012**, *53*, 117-118.

(36) Machui, F.; Abbott, S.; Waller, D.; Koppe, M.; Brabec, C. J. *Macromol. Chem. Phys.* **2011**, *212*, 2159-2165.

(37) Nilsson, S.; Bernasik, A.; Budkowski, A.; Moons, E. *Macromolecules* **2007**, *40*, 8291-8301.

(38) Barton, A. F. M. *Chem. Rev.* **1975**, *75*, 731-754.

(39) Park, J. H.; Kim, J. S.; Lee, J. H.; Lee, W. H.; Cho, K. *J. Phys. Chem. C* **2009**, *113*, 17579-17584.

(40) Tsoi, W. C.; James, D. T.; Kim, J. S.; Nicholson, P. G.; Murphy, C. E.; Bradley, D. D. C.; Nelson, J.; Kim, J.-S. *J. Am. Chem. Soc.* **2011**, *133*, 9834-9843.

(41) Klimov, E.; Li, W.; Yang, X.; Hoffmann, G. G.; Loos, J. *Macromolecules* **2006**, *39*, 4493-4496.

(42) Bull, T. A.; Pingree, L. S. C.; Jenekhe, S. A.; Ginger, D. S.; Luscombe, C. K. *ACS Nano* **2009**, *3*, 627-636.

(43) Dennler, G.; Lungenschmied, C.; Neugebauer, H.; Sariciftci, N. S.; Labouret, A. *J. Mater. Res.* **2005**, *20*, 3224-3233.

(44) Dennler, G.; Scharber, M. C.; Brabec, C. J. *Adv. Mater.* **2009**, *21*, 1323-1338.

(45) Natori, I.; Natori, S.; Kanasashi, A.; Tsuchiya, K.; Ogino, K. *J. Polym. Sci., Part B: Polym. Phys.* **2013**, *51*, 368-375.

(46) Garcia, R. J. L.; Parra, A.; Aleman, J. *Green Chem.* **2008**, *10*, 706-711.

(47) Dintcheva, N. T.; Morici, E.; Arrigo, R.; La Mantia, F.; Malatesta, V.; Schwab, J. *eXPRESS Polym. Lett.* **2012**, *6*,561-571.

(48) Chang, Y.-M.; Wang, L. *J. Phys. Chem. C* **2008**, *112*, 17716-17720.

(49) Garnett, E.; Yang, P. *Nano Lett.* **2010**, *10*, 1082-1087.

(50) Xie, Y.; Bao, Y.; Du, J.; Jiang, C.; Qiao, Q. *Phys. Chem. Chem. Phys.* **2012**, *14*, 10168-10177.

(51) Kim, H.; So, W.-W.; Moon, S.-J. *J. Korean Phys. Soc.* **2006**, *48*, 441-445.

(52) Erb, T.; Zhokhavets, U.; Gobsch, G.; Raleva, S.; Stühn, B.; Schilinsky, P.; Waldauf, C.; Brabec, C. J. *Adv. Funct. Mater.* **2005**, *15*, 1193-1196.

(53) Tan, B.; Wu, Y. *J. Phys. Chem. B* **2006**, *110*, 15932-15938.

(54) Derbal-Habak, H.; Bergeret, C.; Cousseau, J.; Nunzi, J. *Sol. Energy Mater. Sol. Cells* **2011**, *95*, S53-S56.

(55) Liem, H., Cabanillas-Gonzalez, J., Etchegoin, P., Bradley, D. *Journal of Physics: Condensed Matter* **2004**, *16*, 721.

(56) Roth, C.B., Dutcher, J. *The European Physical Journal E: Soft Matter and Biological Physics* **2003**, *12*,103-107.

(57) Zhao, J., Swinnen, A., Van Assche, G., Manca, J., Vanderzande, D., & Mele, B. V.*The Journal of Physical Chemistry B* **2009**, *113*, 1587-1591.

CHAPTER IV

DETERMINATION OF EFFECTS OF SOLVENT VAPOR AND THERMAL ANNEALING ON ENVIRONMENTAL AND MORPHOLOGY STABILITY OF PHOTOACTIVE POLYMER FILMS AND PHOTOVOLTAIC DEVICES

Abstract

P3HT/PCBM OPV devices were prepared in air under different combinations of solvent vapor annealing, encapsulation, and thermal annealing in an attempt to improve performance without the need for inert atmosphere processing. Active layer films were analyzed by AFM, nanomechanical mapping, UV-Vis spectroscopy, and XRD. Devices prepared with isopropanol solvent vapor annealing combined with thermal annealing showed the highest environmental resistance and performance. Such devices yielded average PCE of 3.3 %, with stability to atmospheric exposure of up to 60 minutes prior to encapsulation. Encapsulated devices exposed to the laboratory environment for 30 days exhibited a decrease in PCE of approximately 15%. On application of a second thermal annealing step PCE recovered to over 90% of the original value. The unprecedented air stability of the cells is attributed to formation of a low oxygen content active layer through the solvent vapor annealing process and to development of a stable, favorable morphology.

Introduction

Organic photovoltaic (OPV) cells have undergone rapid development over the last two decades, because of their advantages such as solution processability, flexibility, and stable performance under elevated temperatures.[1] Since the first OPV cell was reported in 1986 with 1% efficiency,[2] the power conversion efficiency has surpassed 10%,[3] which

brings the technology to the edge of commercial feasibility. However, large scale manufacturing of OPV devices is restricted by their low environmental stability, necessitating production in an inert processing environment.[4] Device instability is attributed to both degradation of the conductive polymers and instability of the morphology of the photoactive layer. The photoactive layer consists of a conjugated polymer as the electron donor and a fullerene derivative as the electron acceptor. Free charge carriers are generated at the interfacial areas between donor and acceptor phases. A great extent of phase separation is required to provide sufficient interface to promote charge generation. Photoactive blends prepared without annealing exhibit weak phase separation, but phase separation can be improved by applying annealing techniques, including thermal, solvent, and solvent vapor annealing.[5-7] Phase separation, however, is a thermodynamically meta-stable state in which phase separated domains tend to aggregate into larger domains over time. [8] When the domain size exceeds the exciton diffusion length, the performance decreases.

The most widely studied OPV system is comprised of poly(3-hexylthiophene-2,5-diyl) (P3HT) as the donor and phenyl-C_{61}-butyric acid methyl ester (PCBM) as the acceptor. Several approaches have been explored in an attempt to improve the morphological stability of P3HT/PCBM blends. Holdcroft and coworkers synthesized a graft copolymer of P3HT to PCBM, with which the film morphology was stabilized. The efficiency of the pristine P3HT:PCBM devices dropped 80% after 3 hours at 150 °C, while the devices containing the copolymer showed a decrease of only 50% under the same conditions.[9] A crosslinked PCBM system was developed to prevent PCBM

aggregation over time. [10] However, devices prepared with this material did not yield efficiency comparable to that of the pristine P3HT:PCBM devices.

The necessity for inert atmosphere during device fabrication is another obstacle to OPV commercialization. Photoactive materials are intrinsically sensitive to oxygen and moisture, which can degrade the conjugated system, alter the band gap, and reduce the conductivity. [11,12] Attempts have been made to minimize the inert gas usage during processing steps. Yan and coworkers successfully prepared a P3HT:PCBM device with 3.4% power conversion efficiency using a process that was conducted in air except for the thermal annealing step.[13] It has been found that thermal annealing in air has a destructive effect on the photoactive materials. [14]

In this study, P3HT:PCBM based OPV devices were fabricated entirely in air, without employing inert atmospheric conditions. Isopropanol solvent vapor annealing was applied in an attempt to improve the environmental resistance of the photoactive layer. The devices were subsequently encapsulated with epoxy to reduce further environmental exposure. This encapsulation step allowed a subsequent thermal annealing step, which enhances phase separation, to be performed in air. Device performance was evaluated as a function of exposure time in the laboratory environment, and the effects of thermal annealing after the aging process were determined. Film morphology, absorbance, and crystallinity levels were analyzed using AFM, nanomechanical mapping, UV-Vis spectroscopy, and X-ray diffraction.

Experimentation

Materials

Patterned ITO glass slides with ~100 nm ITO (surface resistivity of 8-12 Ω/sq) were purchased from Luminescence Technology Corp. and used as the transparent anodes. Poly(3,4-ethylenedioxythiophene)-poly(styrenesulfonate) (2.8 wt.% dispersion in water) was obtained from Sigma Aldrich to use as the hole transport layer. P3HT, (Mn ~ 45,000, 98% regioregular) was obtained from Sigma Aldrich to use as the donor material. PCBM (>99%) obtained from Sigma Aldrich was used as the acceptor material. Dichlorobenzene from Acros was used as the solvent for P3HT:PCBM. UV-curable epoxy purchased from Ossila (E 131, 5 to 30 seconds at 250 to 600 nm at 10 - 100mW/cm^2, viscosity~300 cps at 23 ℃) and transparent glass slides obtained from Fisher Scientific were used for encapsulation. Isopropanol (IPA, 99.5%, anhydrous) from Sigma Aldrich was used for solvent vapor annealing. All the materials were used as received.

Sample Preparation

A series of devices was prepared with different levels of thermal and solvent vapor annealing and atmospheric exposure to evaluate the combined effects of oxygen exposure annealing on device performance.

Devices prepared with solvent vapor and thermal annealing (SVA-TA). A blend of P3HT:PCBM (ratio 1:0.8) in DCB (25 mg/ml) was prepared. The mixture was heated at 60 ℃ for one hour and then was kept at room temperature for 24 hours before use. Patterned ITO glass slides were successively cleaned ultrasonically in deionized water, acetone, and IPA for 10 minutes each. The cleaned ITO glass slides were dried and

exposed to UV/ozone generated by a ProCleaner™ Plus system for 40 minutes. The PEDOT:PSS dispersion was spin-coated on the ITO surface at a speed of 5000 rpm for 1 min. The uniformly coated substrates were then thermally annealed in air on a hot plate at 150 ℃ for 10 min to remove the residual water. The film thickness was measured by AFM to be 40 nm. The prepared P3HT:PCBM solution was then spin coated on top of the PEDOT:PSS layer at a speed of 1250 rpm for 120 sec. The thickness of the P3HT:PCBM layer was measured to be around 100 nm by AFM scratch testing. Samples were placed in a covered chamber saturated with IPA vapor for 20 min for solvent vapor annealing. A 100 nm thick Al layer was then deposited onto the annealed P3HT:PCBM layer through a shadow mask at the rate of 35 nm/min using the metal evaporation function of a Q150T Turbo-Pumped Sputter Coater. A thin layer of UV-curable epoxy was then spread across the top and sides of the multilayer film and a transparent glass slide was placed on top of the epoxy layer. Slight pressure was applied to remove the bubbles inside the epoxy layer. The covered devices were then placed in a UV reactor for 10 min to ensure that the epoxy was fully cured. Samples subjected to thermal annealing were then annealed at 150 ℃ in air for 10 min. The completed devices had an active area of 0.042 cm^2 and 6-10 devices were used in performance measurement. The devices were kept in air in the dark at room temperature for degradation studies.

Devices prepared with air exposure between the solvent and thermal annealing steps (SVA-Air60min-TA). The fabrication of these samples followed the same procedure as that described for the SVA-TA samples, except that after solvent vapor annealing, the devices were placed in air for 60 min in a temperature (20 ℃) and humidity (50% humidity) controlled room prior to Al deposition.

Devices prepared with thermal annealing only (TA). For these samples the fabrication procedure was the same as that described for the SVA-TA samples, except that no solvent vapor annealing was applied. The Al cathode was deposited onto the surface of the P3HT:PCBM layer immediately after spin coating.

Thermally annealed devices with air exposure (Air60min-TA). Samples were prepared following the same fabrication procedure as that described for the TA samples, except that after spin coating of P3HT:PCBM, the devices were placed in air for 60 min before Al deposition.

Photoactive Film Preparation

Film samples were prepared for AFM, UV-vis spectroscopy and XED studies by spin coating the P3HT:PCBM solution on clean transparent glass slides using the conditions described previously. SVA samples were placed in an IPA saturated chamber for 20 min. TA were annealed at 150 ℃ in argon for 10 min to avoid oxidation.

Analytical Techniques

AFM studies were conducted on a Dimension ICON scanning probe microscope from Bruker Biosciences Corporation. Nanomechanical mapping images were acquired under quantitative nanomechanical mapping mode with a calibrated silicon probe (RTESPA, spring constant of 20-80 N/m, obtained from Bruker Biosciences Corporation). The calibration process was performed using the absolute method and was checked through the relative method as recommended by the supplier.[15]

UV-Vis spectra were obtained using a Perkin-Elmer Lambda 6 UV/Vis spectrophotometer. X-ray diffraction studies were obtained using a Rigaku D/MAX-Ultima-III diffractometer at room temperature using Cu Kα radiation at a tube current of

44 mA and an acceleration voltage of 40 kV. Scan range was 4 °- 8 °at a step interval of 0.01 °and a scanning rate of 0.05 °/min.

Current-voltage (J-V) measurements were carried out using a Keithley 2400 source unit. Irradiation was provided by an AM1.5 solar simulator (Photo Emission Tech. Inc.) with illumination of 1000 W/m^2 from a Xenon lamp coupled to a monochromator. The total incident light intensity was calibrated with a standard reference silicon solar cell. The performance parameters of open circuit voltage (V_{oc}), short circuit current (J_{sc}), fill factor (FF) and power conversion efficiency (PCE) were extracted from the J-V curves.

Results and Discussion

Device Performance

In order to determine the effects of limited atmospheric exposure on OPV performance, devices using standard OPV materials were prepared in air with varying annealing and encapsulation procedures as described in the experimental section. Current-voltage curves for devices prepared with thermal annealing only (TA), isopropanol solvent vapor annealing followed by thermal annealing (SVA-TA), and devices with an additional one hour exposure to ambient environment prior to aluminum deposition, encapsulation, and thermal annealing (with and without solvent vapor annealing, SVA-Air60-TA and Air60-TA) are shown in Figure 27. Boxplots of the performance characteristics are shown in Figure 28 (six to ten devices were prepared under each set of processing conditions). Those samples exposed to IPA vapor annealing combined with thermal annealing show dramatically improved performance in comparison to those undergoing only thermal annealing, and, in fact, the device

characteristics are similar to those reported for devices prepared in inert atmosphere [16] (average values for SVA-TA samples: J_{sc} = 9.6 mA/cm^2, V_{oc} = 0.6V, FF = 58.3% and PCE =3.3%). Surprisingly, the SVA-TA samples showed no degradation in performance after the additional 60 minutes exposure to air. Those samples undergoing only thermal annealing, on the other hand, demonstrated lower measured device characteristics similar to those reported for air processed cells [17] (average values for TA samples J_{sc} = 8.7 mA/cm^2, V_{oc} = 0.59 V, FF = 41.3% and PCE =2.1%). After the additional 60 minute air exposure the performance decreased dramatically (average values for Air60-TA samples: J_{sc} = 5.2 mA/cm^2, V_{oc} = 0.3V, FF = 27.8% and PCE = 0.5%). Note that epoxy encapsulation did not appear to change the performance compared to that reported for unencapsulated samples.[16,17]

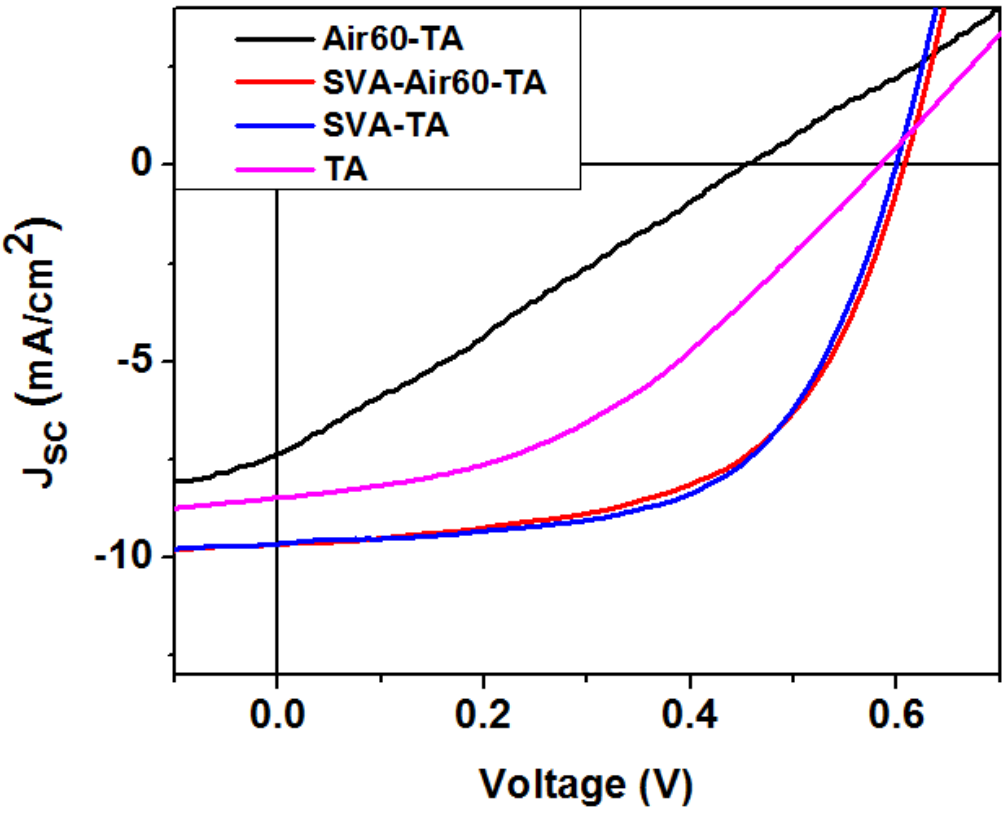

Figure 27. J-V curves of devices prepared under varying combinations of annealing and air exposure.

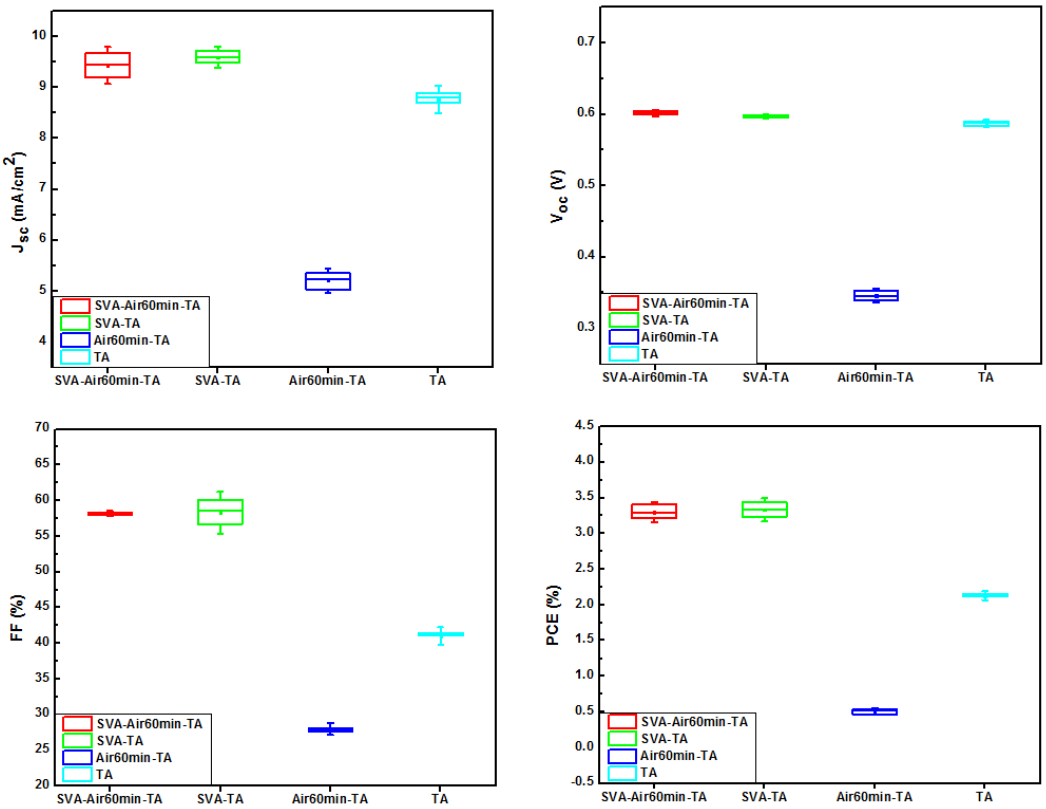

Figure 28. Box plots of measured parameters for devices prepared under different conditions of annealing and air exposure. (The bottom star represents the 1st percentile, the top star is the 99th percentile, the top line of the box is the 75th percentile, the central line of the box is the median, the bottom line of the box is the 25th percentile, and the solid square within the box is the mean).

We hypothesize that the IPA annealing process produces a film with reduced oxygen content compared to that of the film produced in air. Based on Henry's law, the amount of a given gas dissolved in a liquid is proportional to the partial pressure of the given gas in equilibrium with the liquid.[18] The incorporation of IPA vapor that decreases the partial pressure of oxygen in the solvent chamber also reduces the amount of oxygen in the swollen P3HT:PCBM films. When the films are completely dried, the solvent vapor annealed films have a very small level of dissolved oxygen in comparison to those dried in air. Oxygen diffusion in the dried films occurs at a much slower rate. Solvent vapor annealing alone, however, is not enough to produce the desired performance

characteristics, as shown in the comparative current/voltage plots for SVA-TA and SVA samples (Figure 29). SVA combined with TA yields improvement in J_{sc} of 25% , V_{oc} of 15% and PCE of 38% in comparison to SVA alone. Improvement of J_{sc} has been widely reported as a result of thermal annealing, attributed to changes in the phase separated morphology that increase hole and electron mobility.[19] However, substantial improvement in V_{oc} is not normally observed, particularly for devices fabricated in inert atmosphere.[20,21] In our case, the improvements in measured V_{oc} with thermal annealing are attributed to the doping action of oxygen associated with P3HT. V_{oc} is proportional to the energy difference between the HOMO level of P3HT and the LUMO level of PCBM. [22] Oxygen acts as a dopant to P3HT and elevates its HOMO level, which thus decreases the V_{oc}. [23] The oxygen doping action is thermally reversible, and upon thermal annealing, oxygen is released and V_{oc} increases. [22] While IPA solvent vapor annealing results in an active layer with reduced oxygen levels, it is not entirely purged of oxygen. Thermal annealing eliminates P3HT-associated oxygen, which corrects the energy mismatch and results in an increase in the V_{oc}.

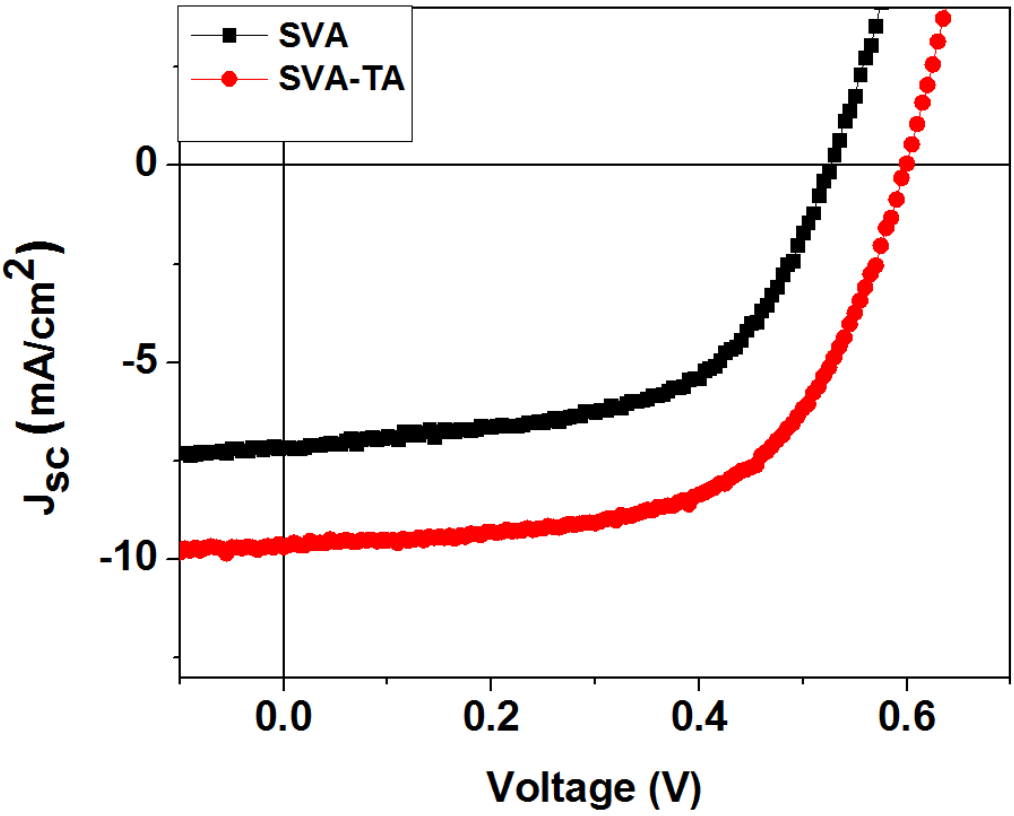

Figure 29. J-V curves of devices prepared with SVA and SVA-TA annealing.

Film Characteristics

Photoactive films were prepared on unpatterned ITO glass surfaces to evaluate the effects of annealing on film morphology and photophysical properties. Comparative X-ray diffraction curves of photoactive films prepared with varying annealing conditions are presented in Figure 30, in which the observed diffraction peak near 5.3 degrees is attributed to crystallized P3HT. The film prepared without annealing shows a low intensity peak centered at 5.28 degrees, indicating low crystallinity. The film exposed to IPA vapor annealing alone shows a small increase in peak intensity and a shift to 5.43 degrees, indicating an increase in crystallinity and closer chain packing in the P3HT phase. [24] The films exposed to thermal annealing alone and SVA followed by TA exhibit

five-fold increases in peak intensity in comparison to the neat sample. The increases are attributed to greater chain mobility during thermal annealing, which allows increased crystallization of the P3HT phase. A very small improvement in degree of crystallinity is present for the SVA-TA sample in comparison to that undergoing TA alone. A similar trend is observed in UV-Vis light absorption (Figure 31). Light absorption increases in the order of: no annealing < SVA < TA < SVA-TA. Increased absorption in the 350 – 700 nm range is attributed to higher crystallinity and more closely packed P3HT chains.[25] The differences in the UV-Vis absorption spectra are greater than those observed in XRD for the SVA-TA and TA samples. These differences are attributed to changes in the nanoscale morphology, which are discussed in the next section.

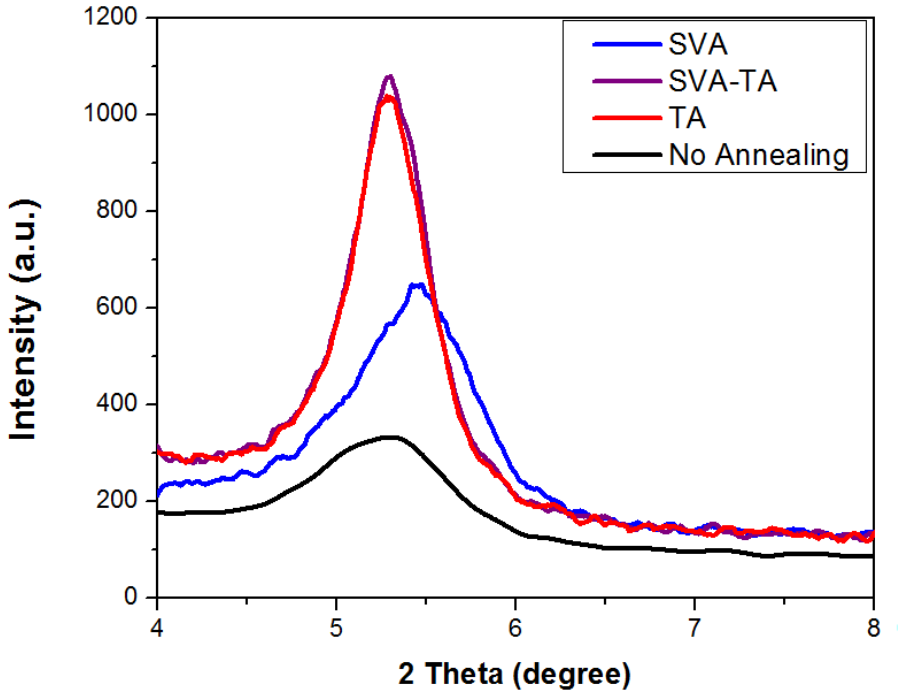

Figure 30. XRD curves of samples prepared with different annealing processes.

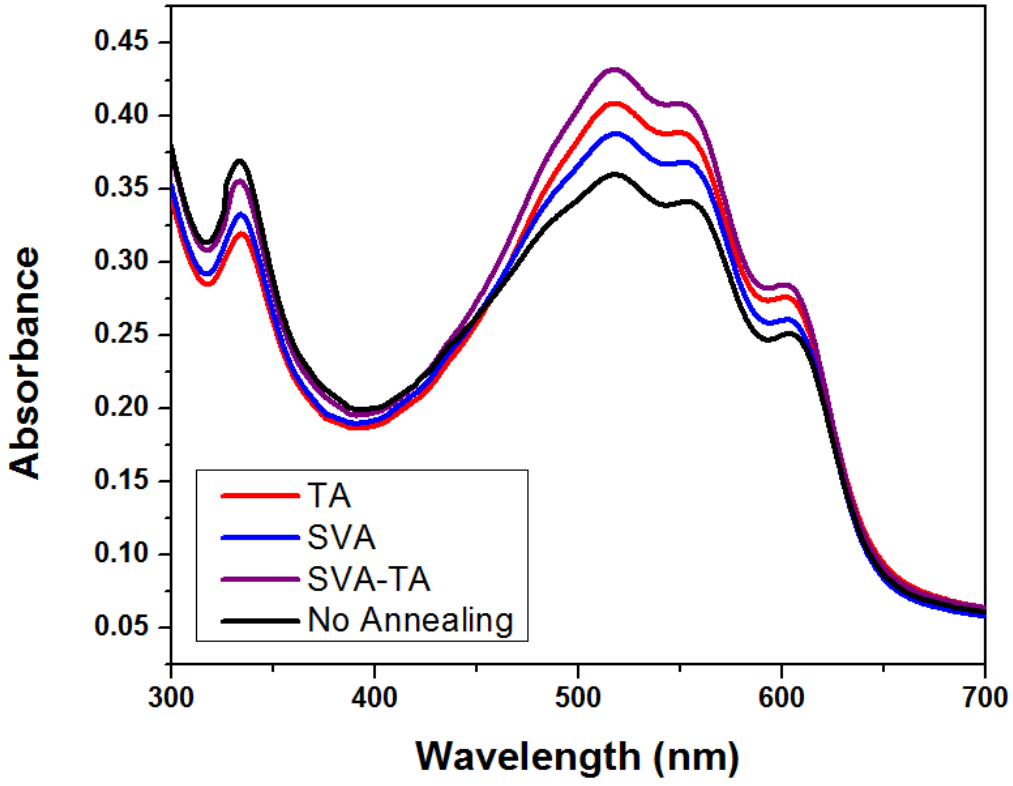

Figure 31. UV-vis spectra of samples prepared with different annealing processes.

Film Morphology

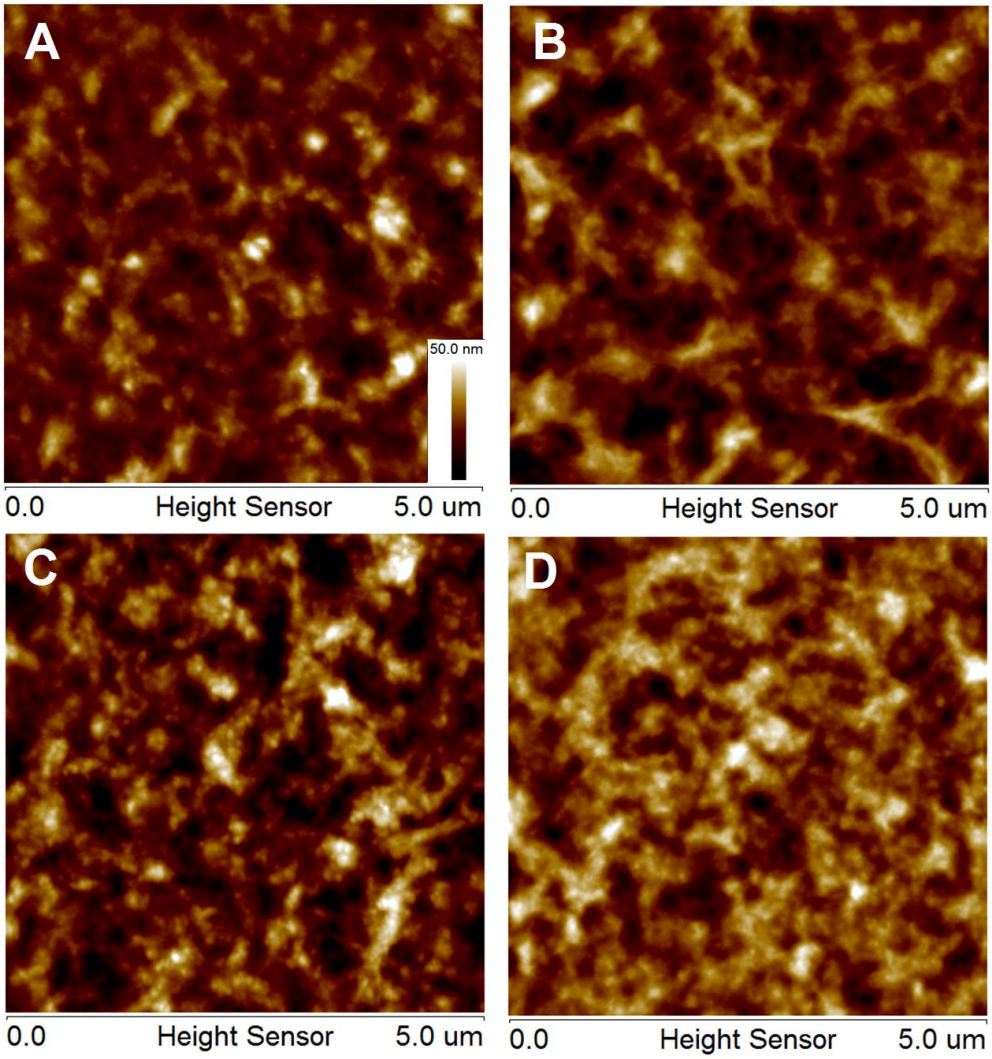

Figure 32. AFM height images of samples with (A) no annealing, (B) TA, (C) SVA, and (D) SVA-TA. Z-scale for all images is 50 nm.

Film morphology plays a key role in determining the performance of OPV devices. AFM height images of samples prepared with varying annealing processes are presented in Figure 32. The unannealed sample (Figure 32A), shows bright and dark sub-micron features that may be associated with phase-separated domains. Thermal annealing (Figure 32B) produces a coarser morphology, with large fibers of 1-2 microns in length

and 200-300 nm in width. This type of morphology is normally reported for thermally annealed films.[26] The sample exposed to solvent vapor annealing (Figure 32C) exhibits micron-sized fiber-like structures composed of smaller spherical features. These spherical domains are believed to be formed during the film drying process, when IPA (a poor solvent) promotes P3HT molecular aggregation in the swollen film. Thermal annealing of the SVA-treated films produces similar morphology (Figure 32D), with a large number of the 100 nm spherical features that appear to form a continuous network across the surface. In order to examine the nanoscale morphology of the films, nanomechanical mapping studies were performed on 500 nm sections, shown in Figure 33. In these images the bright features (high DMT Modulus) are attributed to the PCBM phase, while dark areas are attributed to the low modulus P3HT phase.[27] The film prepared without annealing shows weak phase separation (Figure 33A), where P3HT and PCBM domains are dispersed on the surface and no ordered morphology is observed), as has been reported previously. [20] The film made with TA only (Figure 33B) shows relatively large P3HT domains (~100 nm) with a lower concentration of dispersed P3HT domains. The film produced with SVA only (Figure 33C), on the other hand, shows smaller interpenetrating PCBM and P3HT phases on the order of 10-40 nm, which appear to form interconnected networks across the surface of the film. The SVA-TA film (Figure 33D) shows a similar surface morphology to that observed with SVA alone, indicating formation of a stable morphology during solvent vapor annealing.

Recall that XRD evaluation indicated that the size of P3HT crystallites and overall degree of crystallinity were similar for TA and SVA-TA samples, but UV-Vis analysis showed substantially higher absorbance for the SVA-TA sample. AFM analysis

shows a finer morphology for SVA-TA samples than for TA samples, with smaller, more highly dispersed, phase separated domains, which form an interpenetrating network. We attribute the high device efficiency measured for SVA-TA samples to this interpenetrating network morphology consisting of phase domain sizes similar to that of the exciton diffusion length.

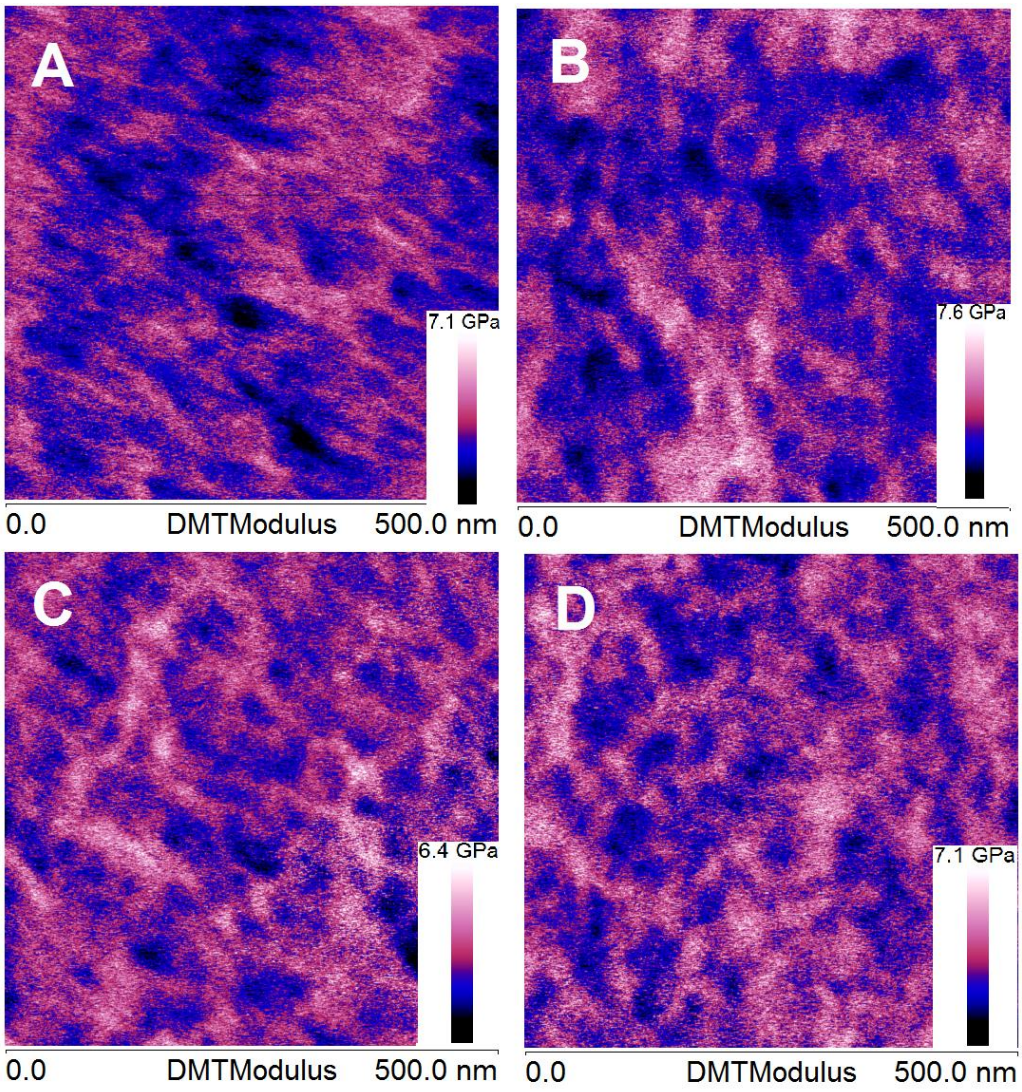

Figure 33. DMT modulus images of films produced with: (A) no annealing, (B) TA, (C) SVA, and (D) SVA-TA.

Degradation and Recovery

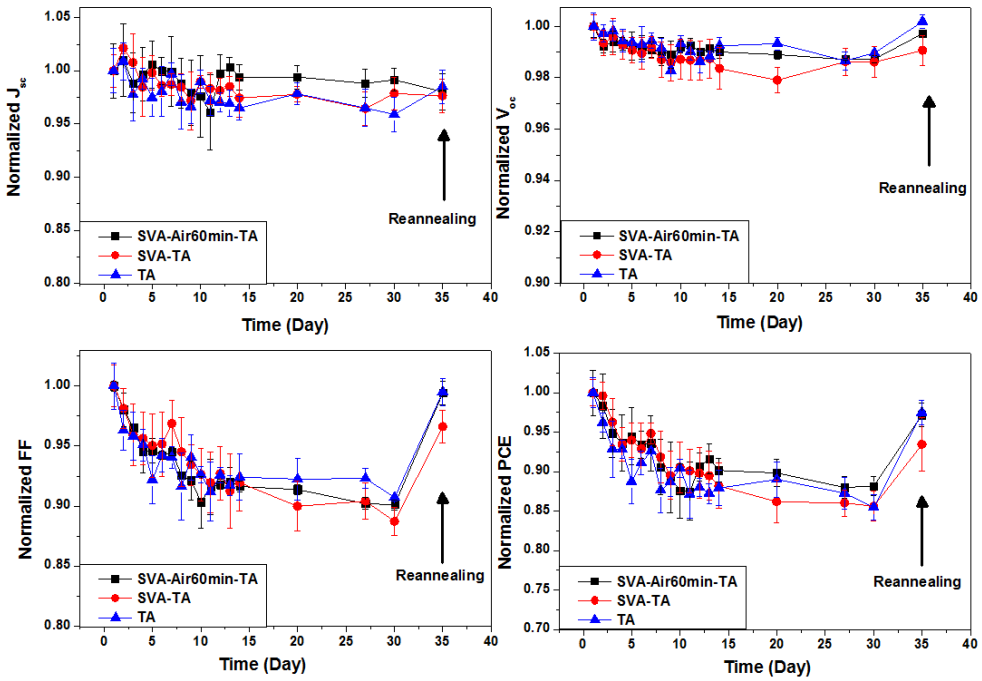

Figure 34. Device performance characteristics as a function of aging time in air for devices prepared under different annealing conditions and recovery after thermal annealing.

The encapsulated devices with the highest initial performance (SVA-Air60min-TA, SVA-TA, and TA) were exposed to the ambient laboratory environment for 30 days, and their performance was monitored periodically. In Figure 8 the device characteristics measured as a function of exposure time are shown, normalized to the initial performance values. The three device types exhibit similar degradation trends, despite differences in the annealing methods and previous environmental exposure, indicating a common degradation mechanism. In general, there is fairly little change in J_{SC} and V_{0C} over time, but larger, parallel changes are observed in FF and PCE. A two-step degradation pathway is exhibited: a fast initial decrease in properties (~7% efficiency drop in the first 4 days), followed by a slow decrease in properties during the second stage (~8%

efficiency drop in the following 26 days). A similar phenomenon has been reported in other studies; [28,29] however, the mechanism of degradation is not well established. Following the 30 day environmental exposure, a reannealing process was performed in which the devices were thermally annealed for 5 min at 150 °C. Surprisingly, the FF and PCE recovered to greater than 90% of their original values for all three device types.

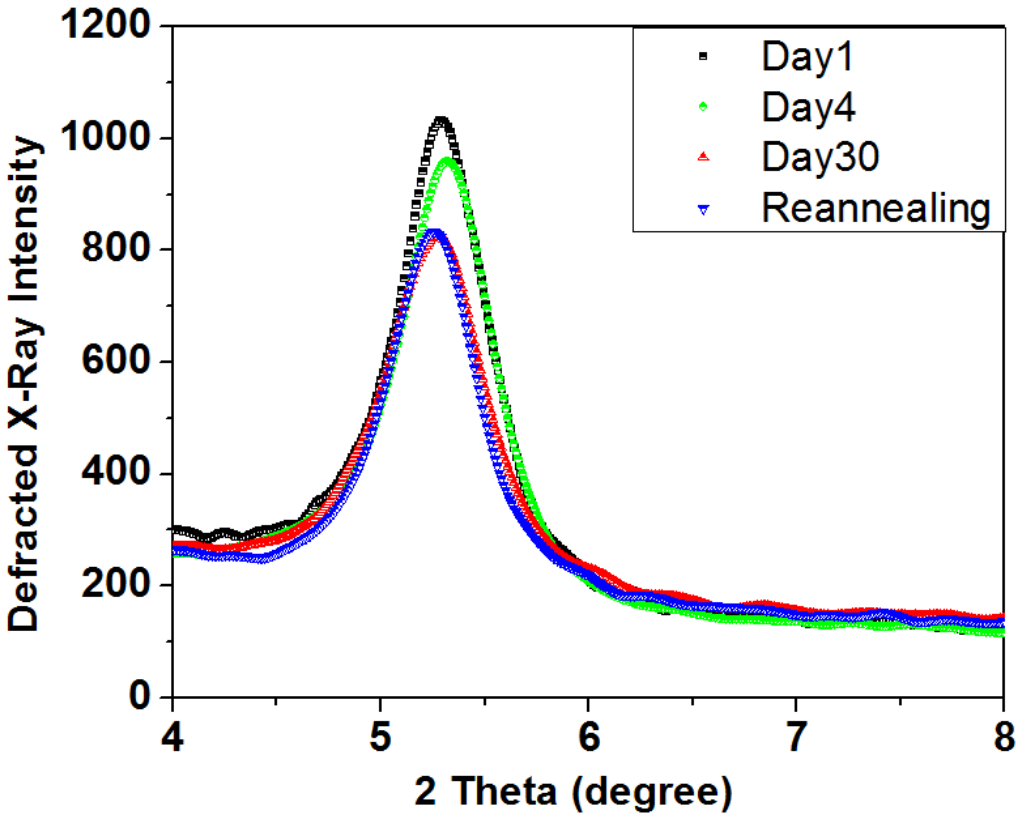

Figure 35. XRD spectra of the degraded and reannealed SVA-TA devices.

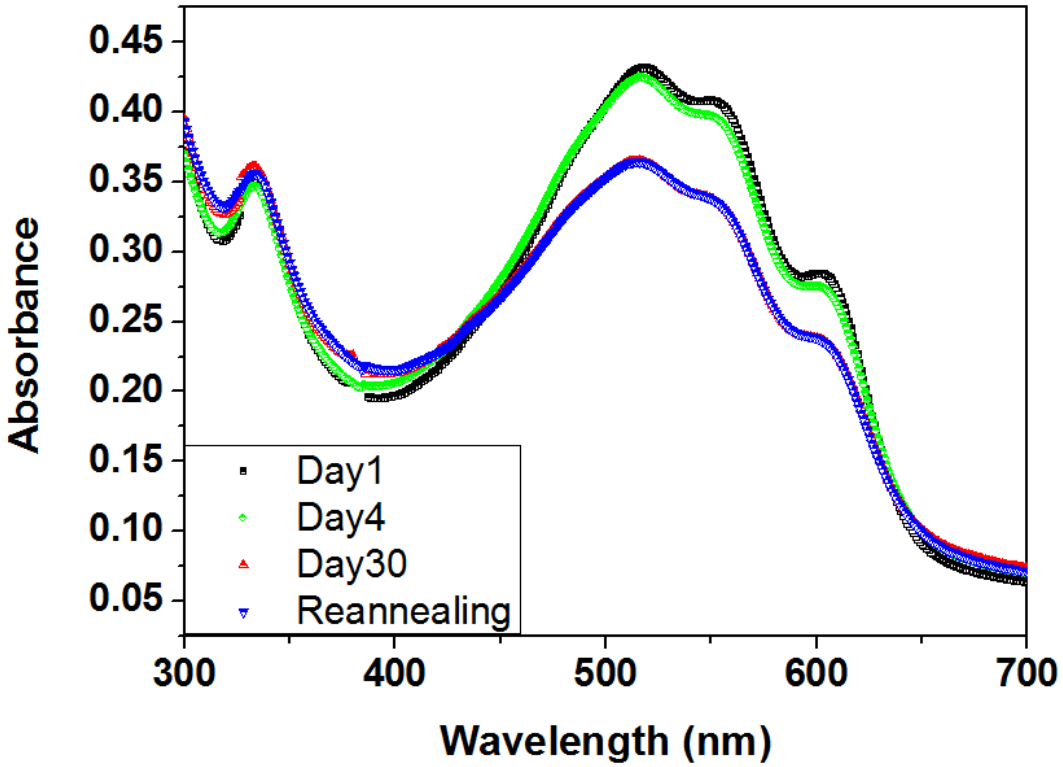

Figure 36. UV-vis spectra of the degraded and reannealed SVA-TA devices.

It is believed that both chemical degradation and morphologic changes in the P3HT:PCBM films as a function of aging time contribute to the observed decrease in performance.[4] Figure 35 shows XRD analysis of films prepared with SVA-TA as a function of environmental exposure and reannealing. The gradual decrease in the intensity of the P3HT crystalline peak is attributed to oxidative degradation of the P3HT backbones that reduces molecular weight and crystallinity.[30] P3HT degradation is also indicated by the observed decrease in light absorption as a function of aging time by UV-Vis analysis (Figure 36). However, no observable changes were observed after the reannealing process in either XRD or UV-Vis spectra, indicating that the performance recovery is not the result of increased P3HT crystallinity but is rather the result of other morphological changes. It should be noted that over 65% of the efficiency lost during

environmental exposure is recovered during the reannealing process, indicating that both the performance degradation and the recovery are driven by these morphological changes.

AFM images of the exposed and reannealed samples are shown in Figure 11. In the second column (5 micron DMT images), micron-sized phase separated PCBM aggregates (bright features) are observed in the 30 day annealed sample (Figure 37C2), which largely disappear after the reannealing step (Figure 37 D2). In the third column, smaller scale features can be observed in the 500 nm DMT images. The average diameter of the phase separated domains in the third column was calculated by the nanoscope analysis software. A threshold color template was applied on the blue-purple DMT modulus image to fit the phase separated domain shape, based on which both the P3HT and PCBM domain sizes were calculated. Coarsening of the morphology is observed after 4 days (Figure 37B3); the P3HT domain size increased from 16 nm to 34 nm, and the PCBM domain size increased from 12 nm to 20 nm. The domain sizes are even larger after 30 days (Figure 37C3) with 40 nm P3HT domains and micron-size PCBM features. Both domains show decreased size (23 nm in P3HT and 15 nm in PCBM) and greater network connectivity in the film that has undergone reannealing (Figure 37D3); however, the morphology is not as fine as that observed initially (Figure 37A3). To our surprise, the PCBM aggregates do not appear as promoted features on the corresponding height images (Figure 37C1). The ratio of the P3HT and PCBM domains on the surface was also calculated by the threshold method. The freshly prepared film showed 62% PCBM on the surface, but the ratio decreased to 55% after 4 days and 51% after 30 days. The decrement of PCBM content is attributed to the formation of the micron sized PCBM

aggregates. After thermal annealing, the PCBM content in Figure 37 D3 increased to 75% because of the re-dispersion of the micron PCBM features..

Phase separation is a meta-stable equilibrium that is time-dependent. Compared with the large PCBM crystals on a thermally annealed surface reported by others,[31] the observed aggregates in our case might stem from small crystalline nuclei, present but not observable in the as-produced film, that require aging time to form large PCBM domains. It should be noted that PCBM aggregates faster than P3HT, [32] but, in general, its aggregation does not influence the P3HT domain size. [33] Therefore, even though micron sized PCBM aggregates are formed, the comparably stable P3HT domains limit the rate of the performance degradation. In the reannealing process, the number of PCBM aggregates decreases dramatically, as shown in Figure 37D2. We attribute this to increased molecular motion that drives PCBM disaggregation and promotes formation of the interpenetrating network, observed in Figure 37D3, which results in recovery of the device performance.

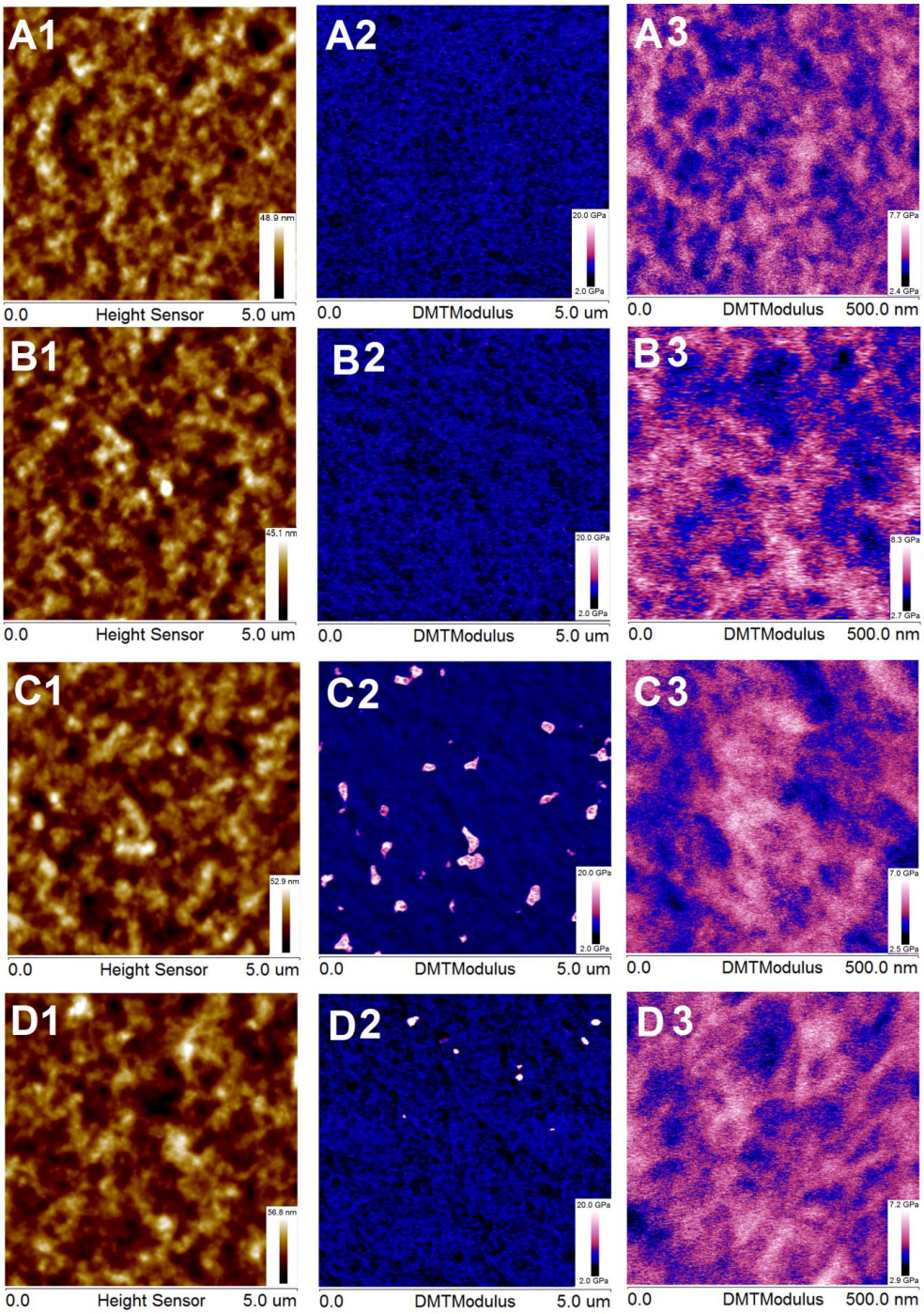

Figure 37. AFM images of SVA-TA samples at the (A) first day, (B) 4 days, (C) 30 days and (1) reannealing. A1-D1 are the height images corresponding to 5 μm DMT modulus images of A2-D2. A3-D3 are 500 nm DMT modulus images taken from small sections of A2-D2.

Conclusions

Air-processed P3HT:PCBM OPV devices with power conversion efficiencies of 3.3 % were produced employing a solvent vapor annealing process using a poor solvent (isopropanol). The devices were surprisingly stable, and maintained high efficiency levels even after exposure to ambient environment for one hour prior to encapsulation. Long-term stability of encapsulated devices was evaluated by exposure to ambient environment for 30 days. Losses in fill factor and PCE of approximately 15 % were observed. Remarkably, more than 90% of the original efficiency could be recovered by applying a second thermal annealing process to the aged cells, indicating that the degradation was primarily driven by changes in morphology.

The remarkable performance and stability levels achieved with these cells are attributed to two factors: 1) the development of a low oxygen content active layer through the isopropanol-saturated annealing/film formation process and 2) the formation of a stable, highly dispersed, interconnected, phase-separated morphology with domain sizes close to the exciton diffusion length through the solvent vapor annealing process. Nanomechanical mapping analysis was employed to demonstrate morphological characteristics, and UV-Vis spectroscopy showed enhanced absorbance for SVA films. These findings demonstrate the possibility of developing lower cost manufacturing methods to produce high performance OPV cells without the need for inert environment production.

References

(1) Xue, J. *Polym. Rev.* **2010**, *50*, 411.

(2) Tang, C. W. *Appl. Phys. Lett.* **1986**, *48*, 183.

(3) You, J.; Chen, C.-C.; Hong, Z.; Yoshimura, K.; Ohya, K.; Xu, R.; Ye, S.; Gao, J.; Li, G.; Yang, Y. *Adv. Mater.* **2013**, *25*, 3973.

(4) Jørgensen, M.; Norrman, K.; Krebs, F. C. *Solar Energy Materials and Solar Cells* **2008**, *92*, 686.

(5) Padinger, F.; Rittberger, R. S.; Sariciftci, N. S. *Adv. Funct. Mater.* **2003**, *13*, 85.

(6) Li, G.; Shrotriya, V.; Huang, J.; Yao, Y.; Moriarty, T.; Emery, K.; Yang, Y. *Nat. Mater.* **2005**, *4*, 864.

(7) Ma, W.; Yang, C.; Gong, X.; Lee, K.; Heeger, A. *J. Adv. Funct. Mater.* **2005**, *15*, 1617.

(8) Ray, B.; Alam, M. A. *Applied Physics Letters* **2011**, *99*, 033303.

(9) Gholamkhass, B.; Holdcroft, S. *Chemistry of Materials* **2010**, *22*, 5371.

(10) Drees, M.; Hoppe, H.; Winder, C.; Neugebauer, H.; Sariciftci, N. S.; Schwinger, W.; Schäffler, F.; Topf, C.; Scharber, M. C.; Zhu, Z. *Journal of Materials Chemistry* **2005**, *15*, 5158.

(11) Hermenau, M.; Riede, M.; Leo, K.; Gevorgyan, S. A.; Krebs, F. C.; Norrman, K. *Solar Energy Materials and Solar Cells* **2011**, *95*, 1268.

(12) Reese, M. O.; Nardes, A. M.; Rupert, B. L.; Larsen, R. E.; Olson, D. C.; Lloyd, M. T.; Shaheen, S. E.; Ginley, D. S.; Rumbles, G.; Kopidakis, N. *Advanced Functional Materials* **2010**, *20*, 3476.

(13) Wu, S.; Li, J.; Tai, Q.; Yan, F. *The Journal of Physical Chemistry C* **2010**, *114*, 21873.

(14) Manceau, M.; Rivaton, A.; Gardette, J.-L.; Guillerez, S.; Lemaître, N. *Polymer Degradation and Stability* **2009**, *94*, 898.

(15) Pittenger, B.; Erina, N.; Su, C. *Quantitative Mechanical Property Mapping at the Nanoscale with PeakForce QNM.* Application Note of Veeco Instruments Inc 2010.

(16) Dang, M. T.; Hirsch, L.; Wantz, G. *Advanced Materials* **2011**, *23*, 3597.

(17) Rider, D. A.; Tucker, R. T.; Worfolk, B. J.; Krause, K. M.; Lalany, A.; Brett, M. J.; Buriak, J. M.; Harris, K. D. *Nanotechnology* **2011**, *22*, 085706/1.

(18) Lide, D. R. *Handbook of Chemistry and Physics*; CRC press: Boca Raton, 2004.

(19) Yang, X.; Loos, J.; Veenstra, S. C.; Verhees, W. J.; Wienk, M. M.; Kroon, J. M.; Michels, M. A.; Janssen, R. A. *Nano Letters* **2005**, *5*, 579.

(20) Li, G.; Shrotriya, V.; Yao, Y.; Yang, Y. *Journal of Applied Physics* **2005**, *98*, 043704.

(21) Agostinelli, T.; Lilliu, S.; Labram, J. G.; Campoy-Quiles, M.; Hampton, M.; Pires, E.; Rawle, J.; Bikondoa, O.; Bradley, D. D.; Anthopoulos, T. D. *Advanced Functional Materials* **2011**, *21*, 1701.

(22) Grossiord, N.; Kroon, J. M.; Andriessen, R.; Blom, P. W. *Organic Electronics* **2012**, *13*, 432.

(23) Lu, C.-K.; Meng, H.-F. *Physical Review B* **2007**, *75*, 235206.

(24) Li, G.; Shrotriya, V.; Yao, Y.; Huang, J.; Yang, Y. *J. Mater. Chem.* **2007**, *17*, 3126.

(25) Vanlaeke, P.; Swinnen, A.; Haeldermans, I.; Vanhoyland, G.; Aernouts, T.; Cheyns, D.; Deibel, C.; D'Haen, J.; Heremans, P.; Poortmans, J. *Solar Energy Materials and Solar Cells* **2006**, *90*, 2150.

(26) Ma, W.; Kim, J. Y.; Lee, K.; Heeger, A. J. *Macromolecular Rapid Communications* **2007**, *28*, 1776.

(27) Wu, Q.; Bhattacharya, M.; Morgan, S. E. *ACS Applied Materials & Interfaces* **2013**, *5*, 6136.

(28) Reese, M. O.; Morfa, A. J.; White, M. S.; Kopidakis, N.; Shaheen, S. E.; Rumbles, G.; Ginley, D. S. *Solar Energy Materials and Solar Cells* **2008**, *92*, 746.

(29) Hauch, J. A.; Schilinsky, P.; Choulis, S. A.; Childers, R.; Biele, M.; Brabec, C. J. *Solar Energy Materials and Solar Cells* **2008**, *92*, 727.

(30) Chang, Y.-M.; Su, W.-F.; Wang, L. *Solar Energy Materials and Solar Cells* **2008**, *92*, 761.

(31) Chirvase, D.; Parisi, J.; Hummelen, J.; Dyakonov, V. *Nanotechnology* **2004**, *15*, 1317.

(32) Salamandra, L. Organic Photo-Voltaic Cells and Photo-Detectors based on Polymer Bulk-Heterojunctions. Ph.D. Thesis, University of Rome Tor Vergata, July 2009.

(33) Jo, J.; Kim, S. S.; Na, S. I.; Yu, B. K.; Kim, D. Y. *Advanced Functional Materials* **2009**, *19*, 866.

CONCLUSIONS

In this work, the structural and physical factors controlling the size, distribution, and crystallinity of nanoscale phase separated donor and acceptor domains through addition of POSS nanostructured chemicals were elucidated. New methods of producing organic photovoltaic devices entirely in air were developed. The main conclusions are summarized below:

1. POSS molecules were for the first time utilized as nanoadditives in OPV systems to control the phase separated morphology. It was found that POSS molecules of specific structures interacted with donor and acceptor molecules to increase light absorption, decrease the d-spacing of P3HT crystallites, and control the domain size in the P3HT:PCBM photoactive films.

2. Aggregates were observed in the Ph-POSS and SH-POSS modified P3HT:PCBM films. The surface composition of these aggregates was identified by combined techniques including c-AFM, nanomechanical mapping, and Raman imaging. It was found that Ph-POSS enhanced P3HT crystallinity and formed light reflecting Ph-POSS/PCBM aggregates, while SH-POSS formed SH-POSS/P3HT aggregates which reduced P3HT crystallinity. By promoting interconnected phase separated domains, Ph-POSS enhanced the efficiency by 26%.

3. Air-processed P3HT:PCBM OPV devices with power conversion efficiencies of 3.3 % were produced employing IPA solvent vapor annealing and thermal annealing. The P3HT:PCBM films with IPA solvent vapor annealing showed excellent stability to the ambient environment, maintaining stable performance even after one hour exposure

to air. The devices with both solvent vapor annealing and thermal annealing presented the highest light absorption, degree of crystallinity, and device performance.

4. The P3HT:PCBM devices were found to follow a two-stage degradation process over a 30-day exposure to the laboratory environment. It was found that the morphology coarsened over the period of aging, with production of PCBM aggregates and formation of larger P3HT domains. Remarkably, over 90% of the original power conversion efficiency could be restored by applying a thermal annealing step to the aged devices.

RECOMMENDATIONS FOR FUTURE WORK

This work demonstrated the potential to utilize POSS nanostructured chemicals to enhance performance of polymeric OPV devices. It was found that POSS molecules containing phenyl groups formed POSS/PCBM aggregates mediated by π- π interactions and that the resultant aggregates served as light reflective vectors to increase light absorption in the active layer and device performance. However, the conductivity of these aggregates was lower than that of the P3HT:PCBM films. It is recommended that future studies explore the effectiveness of POSS molecules with low molecular weight conjugated groups such as polyanilines, polythiophenes, and polypyroles as morphology controlling additives. These POSS structures are predicted to not only enhance light absorption in the active layer but also to promote the conductivity of the films.

It was found that isopropanol solvent vapor annealing dramatically improved the environmental stability of P3HT:PCBM films. Future studies should explore the application of solvent vapor annealing to the roll-to-roll printing or other industrial thin film processing techniques. Utilization of statistical design of experiments is also recommended to optimize the processing conditions to achieve maximum device performance.